UNIVERSITY OF VERONA

Department of DIAGNOSTICS AND PUBLIC HEALTH

Graduate School of NATURAL SCIENCES AND ENGINEERING

Doctoral Program in NANOSCIENCE AND ADVANCED TECHNOLOGIES

Cycle XXIX/2014

TIN SULPHIDE SOLAR CELLS BY THERMAL EVAPORATION

S.S.D.: FIS/01

Coordinator: PROF. FRANCO TAGLIARO

Supervisor: PROF. ALESSANDRO ROMEO

Ph.D. candidate: SIMONE DI MARE

Tin sulphide solar cells by thermal evaporation – Simone Di Mare
Ph.D. Thesis
Verona, 17th May 2017
ISBN XXXX-XXXX-XXX

a mia moglie,
grazie di cuore

SOMMARIO

Produrre energia elettrica dalla combustione di carburanti di origine fossile o dalla fissione di materiale radioattivo significa inquinare il pianeta, impoverirlo delle sue risorse e non garantire un futuro alle generazioni future. Sebbene nei suoi report annuali l'agenzia internazionale per l'energia (IEA) dipinga una situazione di espansione della produzione di energia "verde", il crescente fabbisogno di energia pulita e a basso costo spinge la ricerca verso nuove frontiere. Nel panorama del fotovoltaico, di anno in anno si vedono maturare i frutti della ricerca negli annunci di nuovi record mondiali di efficienza per molte tecnologie: nuove tecnologie emergenti, basate su concetti o materiali innovativi, si stanno aggiungendo a tecnologie mature, quali quelle basate su Si, CdTe o $CuIn_xGa_{(1-x)}Se_2$. Un esempio di queste nuove tecnologie sono quelle basate sui semiconduttori composti totalmente da elementi chimici non tossici ed abbondanti nella crosta terrestre (quindi potenzialmente a basso costo), come Cu_2ZnSnS_4 o SnS.

In questa tesi di dottorato, verranno studiati alcuni aspetti del solfuro di stagno, SnS, in vista di una sua possibile applicazione come strato assorbente per celle solari a film sottile. Il solfuro di stagno ha ottime proprietà optoelettroniche (band-gap diretta nella regione di massima efficienza teorica, ottimo coefficiente di assorbimento della luce, e mostra intrinsecamente conduzione di tipo p), che lo rendono un ottimo candidato per il fotovoltaico del futuro.

In questa tesi, verranno dapprima discusse le difficoltà incontrate con l'apparato di deposizione e come sono state superate. Successivamente verrà descritto e analizzato il

dispositivo solare basato sul solfuro di stagno e caratterizzato dalla migliore prestazione: questo risultato è in linea con quanto pubblicato in letteratura. La difficoltà nel riprodurre questo risultato in modo sistematico ci spingerà poi ad indagarne le possibili cause: suggeriremo la presenza di una possibile correlazione tra la performance dei nostri dispositivi e la storia termica del materiale grezzo utilizzato per evaporare lo strato assorbente. Nel proseguo della tesi, dato che anche il miglior risultato ha comunque mostrato una performance lontana dal limite teorico per un materiale con la band-gap dell'SnS, studieremo gli effetti di alcuni trattamenti post deposizione ideati per migliorare le caratteristiche optoelettroniche attraverso il miglioramento della qualità cristallina dell'assorbitore. Tali trattamenti post deposizione sono fondamentali in altre tecnologie, come nel caso del CdTe. Si studieranno due tipologie di trattamento termico: in atmosfera controllata o in aria, utilizzando vari composti a base di cloro e non, atti a favorire la ricristallizzazione dell'assorbitore. I risultati ottenuti verranno discussi caso per caso. Infine, anziché concentrarci ancora sulle caratteristiche dell'assorbitore stesso, ma sempre con lo scopo finale di migliorare le prestazioni dei nostri dispositivi, investigheremo delle alternative per gli altri strati che costituiscono nel loro insieme la cella solare: il contatto elettrico anteriore, quello posteriore, e infine il materiale semiconduttore di tipo n che completa la giunzione p-n.

ABSTRACT

The production of electricity by the combustion of fossil fuels or by the fission of radioactive materials leads to the pollution of Earth's environment, impoverishes Earth of its resources and does not secure the future for generations to come. Although International Energy Agency (IEA) in its annual reports depicts an increase of electricity production from renewable energy sources, the increasing need for low cost clean energy pushes research towards new frontiers. In photovoltaics, year after year, we see research coming to fruition with the announcements of new world record efficiencies for many technologies: new emerging technologies, based on innovative concepts or materials, are added to the mature ones, such as those based on Si, CdTe o $CuIn_xGa_{(1-x)}Se_2$. Examples of these innovations are those based on semiconductor compounds totally constituted by non-toxic and Earth's crust abundant chemical species (which could potentially be low cost materials), such as Cu_2ZnSnS_4 or SnS.

In this doctoral dissertation, we will investigate some aspects of SnS (tin sulphide), in view of its application as absorber layer for thin film solar cells. Tin sulphide is characterized by excellent optoelectronic properties (direct band gap in the region of the maximum theoretical efficiency, excellent absorption coefficient, and shows intrinsically p-type conduction), which makes SnS a promising candidate for the photovoltaic of the future.

In the first part of this thesis, we will discuss the issues related to the deposition apparatus, and the strategies applied to solve them. Afterwards, the SnS-based solar

device, which exhibited the best performance, will be described and discussed: our result is consistent with similar processes from international laboratories. Since the reproducibility of this result has been observed to be a complex task, we will study its origin. A possible correlation between the performance of our devices and the thermal history of the SnS raw material used to evaporate the absorber layer has been suggested. Then, since even the best performing device exhibited a poor performance, i.e. far from the theoretical limit for a material with the SnS energy band-gap, we will study the effects of several post deposition treatments, designed to enhance optoelectronic characteristics by improving the crystalline quality of the absorber material. Similar post deposition treatments are fundamental in other technologies, as in the CdTe case. We will study two types of thermal treatment: those taking place in a controlled atmosphere and those in air, by adding different compounds (with and without chlorine) to promote the absorber layer recrystallization process. The results will be discussed case by case. Up to now, we focused on the improvement of the absorber layer to enhance the performance of our devices. In the last part of this thesis, we will investigate some alternatives for the other layers constituting the solar device: the front and back contact, and the n-type semiconductor material which completes the p-n junction.

TABLE OF CONTENT

INTRODUCTION

The International Energy Agency (IEA) annual report[1] states that the electricity generated during 2014 is about 24000 TWh. This quantity has been generated mainly from the combustion of fossil fuels – 40.8 % from coal, 21.6 % from natural gas, 4.3 % from oil – or from nuclear power – 10.6 %. Although these fuels are now convenient from the economic point of view, their availability is finite and their combustion leads to the formation of pollutants (such as CO_2, SO_2, NO_X and particulate of various size) or radioactive waste in the case of nuclear power, which damage the environment. Only the 22.7 % of the electricity generated during 2014 comes from renewable sources – 16.4 % from hydro and 6.3 % from geothermal, solar, wind, …. These technologies have their own drawbacks, high costs, intrinsic intermittency and non-programmability of these sources, landscape pollution, or not mature technologies: however, their availability is virtually infinite and no greenhouse gas are released in Earth's atmosphere.

The data reported by the IEA annual reports relatively to the last five years (2010-2014) depict a continuous increase of the electricity generated from renewable sources – from 3.7 % to 6.3 % – as a result of many factors, such as, for example, the effects of the financial and economic crisis of 2007 and 2008, or the

earthquake which struck Japan in 2011 with the consequent Fukushima nuclear disaster.

Solar power can be used to produce electricity by the so-called *concentrated solar power*, where the solar power is used as heat source in a conventional power plant, or by the *photovoltaic effect* where the direct conversion of solar light in electricity takes place. We are interested in the latter.

During the last decades, many materials/technologies/approaches have been investigated with the aim of giving to mankind an inexpensive green power source.

The *first generation* of solar cells is constituted by all the technologies of solar devices based on monocrystalline and polycrystalline silicon, an indirect band gap semiconductor material (E_g = 1.11 eV) with a maximum power conversion efficiency η = 26.3 %[2]. The *second generation* is an attempt to reduce costs by using only a small amount of direct band-gap semiconductor materials, like CdTe and $CuIn_xGa_{(1-x)}Se_2$ (CIGS), or a less crystalline form of Si, amorphous Si (a-Si). The maximum power conversion efficiencies of these devices are η = 22.1 %[3] for CdTe (E_g = 1.42 eV), η = 22.6 %[4] for CIGS (tuneable E_g value corresponding to the $In_xGa_{(1-x)}$ relative content: E_g = 1.00 eV for x = 1 and E_g = 1.7 eV for x = 0) and η = 14.0 %[5] for a-Si. The first and second generation solar device main cost will be driven by the cost of the constituents meanwhile the technologies reach their maturity (Si wafer in the first case, and the encapsulant material in the latter)[6].

Multi-junction solar cells are devices made by a stack of single junction solar cells, all with a specific energy bandgap: light of different wavelength will be absorbed in the most suitable part of the device. These devices use combinations of III-V semiconductor materials like Al, In, Ga, As, P, and can reach very high conversion efficiencies (η = 44.4 %[7] in the case of three-junction solar concentrator and η = 46.0 %[8] for four-junction solar concentrator), but are very expensive and thus, are used in very specific applications, like aerospace or concentrator photovoltaics.

Commonly, emerging technologies are grouped in the *third generation solar cells*: to further lower the costs, it is necessary to improve conversion efficiency by

designing future devices with different concepts[6], i.e. by adding innovative solutions respect to the common p-n junction. Perovskite solar cell (η = 22.1 %[9]), dye-sensitized solar cell (η = 11.9 %[10]), organic solar cell (η = 11.5 %[11]), quantum dot solar cell (η = 11.6 %[12]) and kesterite solar cell (η = 12.6 %[13]) belong to this group.

Kesterite solar cells belong also to another group – the *Earth abundant* solar cell – since their constituents are Cu, Zn, Sn and S, some of the most abundant elements on Earth's crust. Moreover, it is constituted only by non-toxic elements. Some of the most attracting alternative and low-cost materials for photovoltaic such as Cu_2O[14], Sb_2Se_3[15] or SnS[16] belong to the *Earth abundant* solar cell group.

The interest on tin sulphide in the photovoltaic field is due to its suitable features: its constituents are abundant on Earth, non-toxic, and have a well-developed supply chain. Moreover, SnS has good properties for optoelectronic applications: a direct bandgap close to the maximum of the theoretical limit, a very high absorption coefficient above the direct bandgap, it exhibits native p-type conductivity and a high free carrier concentration. All these features make tin sulphide a potential candidate for alternative absorber in photovoltaic applications.

This dissertation is focused on the investigations on tin sulphide as an inexpensive alternative absorber layer for thin film photovoltaics.

This thesis is organized as follows.

In Chapter 1 the fundamental principles of a solar cells will be briefly described and the state of the art of the SnS-based solar cell technology will be presented.

In Chapter 2 the fabrication process of the standard SnS-based solar cell will be described. Moreover, the main parameters used to characterize a solar device will be discussed, as well as the experimental technique. Finally, the main experimental techniques generally employed to characterize semiconductor material properties like its morphology, composition, crystalline structure and lattice dynamics will be described.

While Chapter 2 is devoted to the characterization techniques, in Chapter 3 the main deposition techniques will be discussed. Since a non-negligible part of the PhD activities has been dedicated to improve the SnS thermal evaporation apparatus to perform research tasks, the main improvements and their effects on the apparatus behaviour will be shortly illustrated.

Chapter 4 contains the research work carried out on SnS as absorber layer. In this chapter, the best working SnS-based device will be described, and its performance will be compared with literature results. Then, the attention will be focused on the device performance irreproducibility which affected our samples. We decided to study the SnS raw material used to deposit the absorber layer, and a correlation between it and sample performance has been found. Thus, to wide our study on the raw material influence on device performance, another important parameter has been added, the substrate temperature, to demonstrate the generality of the phenomenon, and to confirm the importance of this parameter on samples overall properties.

The possibility to improve SnS-based device performance by enhancing the absorber layer crystalline quality after its deposition has been investigated and the results will be discussed in Chapter 5. We applied several post deposition treatments to SnS solar cells. Thermal annealing in vacuum or controlled atmosphere to induce SnS recrystallization have been used. We searched for the correct treating parameters to achieve the desired results without compromising the solar device p-n junction. Another typology of post deposition treatment has been studied: we investigated the possibility to aid the SnS recrystallization process by adding a reactive species, similarly to the $CdCl_2$ activation treatment of the CdTe case. We started precisely applying the $CdCl_2$ treatment to SnS, and then we developed two novel treatments based on non-toxic KI and $SnCl_2$.

In Chapter 6, some modification to our standard SnS device will be discussed. One by one, different materials will be proposed as alternative front contact, buffer layer and back contact. We will show how substituting the standard $Sn:In_2O_3$/ZnO front contact with an $F:SnO_2$ layer we reached the laboratory highest

performance for SnS-based solar cell. Then the attention will be focused on the buffer layer, the n-type part of the junction, since it is known that CdS is not the ideal conjugate material for SnS[17]. We will discuss its substitution with ZnS, and another strategy: to add an n-type SnS layer between CdS and p-SnS to obtain an SnS homojunction to reduce defects due to the CdS-SnS different lattice properties. Finally, a Cu-Au back contact bilayer is proposed as alternative to the standard Au back contact. We studied also the effects of Cu diffusion in our SnS-based device.

In the final part of this dissertation, the main results will be summarized.

Chapter 1.

INTRODUCTIVE CONCEPTS

This chapter will be devoted to the introduction of the basic principles concerning the research activity described in this thesis. In the first part, the fundamental concepts of solar cell devices will be presented. In the second part, the properties of the tin sulphide will be summarized as well as some of the most important results about SnS-based solar cells.

1.1 Solar cell devices

A solar cell is a device able to directly convert solar radiation into electricity by internal photoelectric effect.

The power conversion process requires several steps, and for each one a particular component is needed. The conversion starts with (1) the absorption of a photon, which gives place to the creation of an electron-hole pair as a consequence of the photon destruction. The carriers (2) must be separated before they could recombine, and (3) extracted from the device to supply an external load.

The processes involved in power generation can be described with the following scheme:

1. An *absorption layer* is needed to absorb light. Typically, a *p-type* semiconductor material is used; p-type means that the majority charge carriers are positive carriers, i.e. holes. Every semiconductor material is characterized by an *energy band-gap*, which originates from the periodic structure of atoms in solids and from the atomic species. The energy band-gap of a semiconductor material, E_g, is a primary parameter since it defines its optical properties: only photons with energy $hv > E_g$ can be absorbed. The photon energy excess ($hv-E_g$) is quickly lost (picoseconds) because the generated carriers will thermalize to the band edges by giving energy to the lattice. The energy band-gap influences all the properties of a solar cell; the *maximum theoretical efficiency* of a solar cell can be reached for materials which E_g value lies in the 1.1-1.4 eV range (this is known as Shockley-Queisser – S-Q – limit and is depicted in Fig. 1.1).

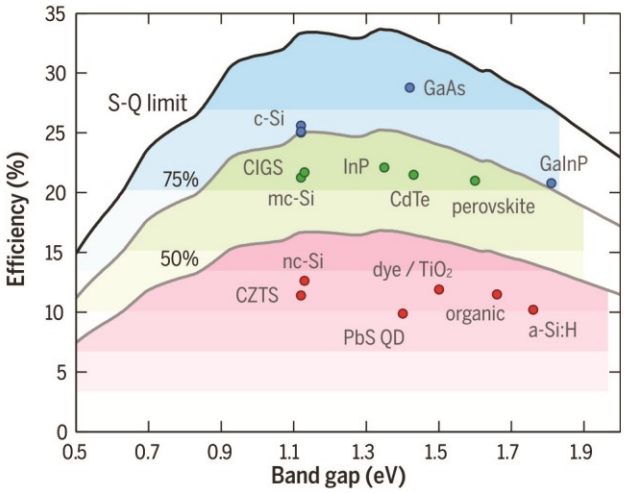

Fig. 1.1: The Shockley-Queisser efficiency (black line). Coloured points indicate different materials record efficiencies plotted at the corresponding band gaps. Adapted from [77].

2. A second layer is coupled to the absorber layer, and is called buffer layer. The buffer layer is an *n-type* semiconductor material: in this case the majority charge carriers are electrons. Once the two layers are in metallurgic contact, this system allows intrinsic charge carriers separation. This system is called *p-n junction* and is the basis of electronic. During the junction formation majority charge carriers diffuse into the region where their concentration is lower. This leads to the formation of a region depleted of mobile charges, called *depletion layer*, where there are only fixed charges. An electric field, the *built-in field*, is thus created across the depletion layer, which ends the diffusion process and the equilibrium

is established. A schematic of a generic p-n junction is showed in Fig. 1.2. When the junction is illuminated, the generated electron-hole pairs are thus separated by the built-in field, the carriers cross the junction, and a voltage across the junction forms.

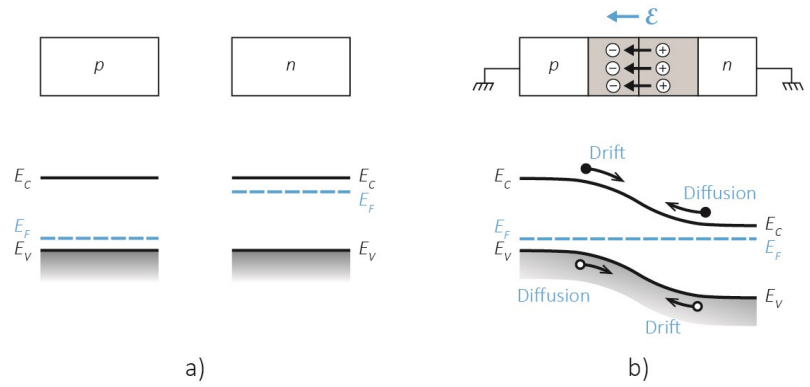

Fig. 1.2: a) p-type and n-type semiconductors before the junction formation. b) The built-in electric field in the depletion layer and the energy band diagram of a p-n junction in thermal equilibrium. Adapted from [78].

3. It is thus possible to feed and to expend the solar cell electromotive force on an external load by connecting the solar cell to it. For extracting the charge carriers from the p-n junction and driving them to the load, an electrical contact for p-n junction side is necessary. These electrical contacts are typically metals, but when a transparent layer is needed, metal-doped insulators are used.

A solar cell can be idealized by an equivalent circuit, as shown in Fig. 1.3: a parallel between a constant-current generator and a diode; the last represent the p-n junction.

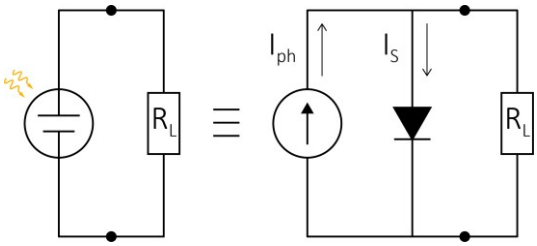

Fig. 1.3: The solar cell equivalent circuit in the single diode model. Adapted from [78].

The relationship between current and voltage, the device current-voltage characteristic or *I-V characteristic*, is thus known:

$$I(V) = I_S\left(e^{\left(\frac{qV}{k_B T}\right)} - 1\right) + I_{ph} \qquad (1.1)$$

where I_S is the saturation current of the diode, I_{ph} is the photocurrent and q, k_B, T are the elementary charge, the Boltzmann constant and the temperature respectively. The typical I-V characteristics for a solar cell in "*dark*" and in "*light*" are shown in Fig. 1.4. When no

light is illuminating the solar device, I_{ph} = 0 mA, and thus the I-V characteristic reduces to the diode one. Otherwise, by illuminating the device, the curve is shifted toward negative current values by the factor I_{ph}. The only region where it is possible to supply an external load is where the power ($P = I \cdot V$) is negative, i.e. the fourth quadrant of the I-V characteristic. The current and voltage values which minimize their product (I_M, V_M) define the *maximum power point*, P_M. This point is the absolute minimum of the power curve.

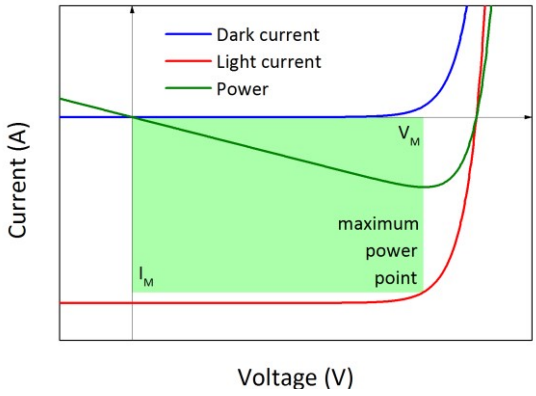

Fig. 1.4: The current-voltage characteristic of an ideal solar cell under dark (blue) and under illumination (red). The green curve is the current voltage product: the generated light power.

The quality of the solar cell behaviour is described by its power conversion efficiency, η, which is defined as the ratio:

$$\eta = \frac{P_M}{P_I} \tag{1.2}$$

where P_I is the power of the incident light. The incident light power which reaches Earth's surface at sea altitude after being reflected and scattered by atmosphere, clouds and pollutants, can be approximated to 1000 W/m^2.

As a summary of what has been described above, Fig. 1.5 shows a schematic of a solar cell p-n junction, where the energy loss mechanisms in a standard single junction photovoltaic device are indicated. These processes will be described in the next subsection.

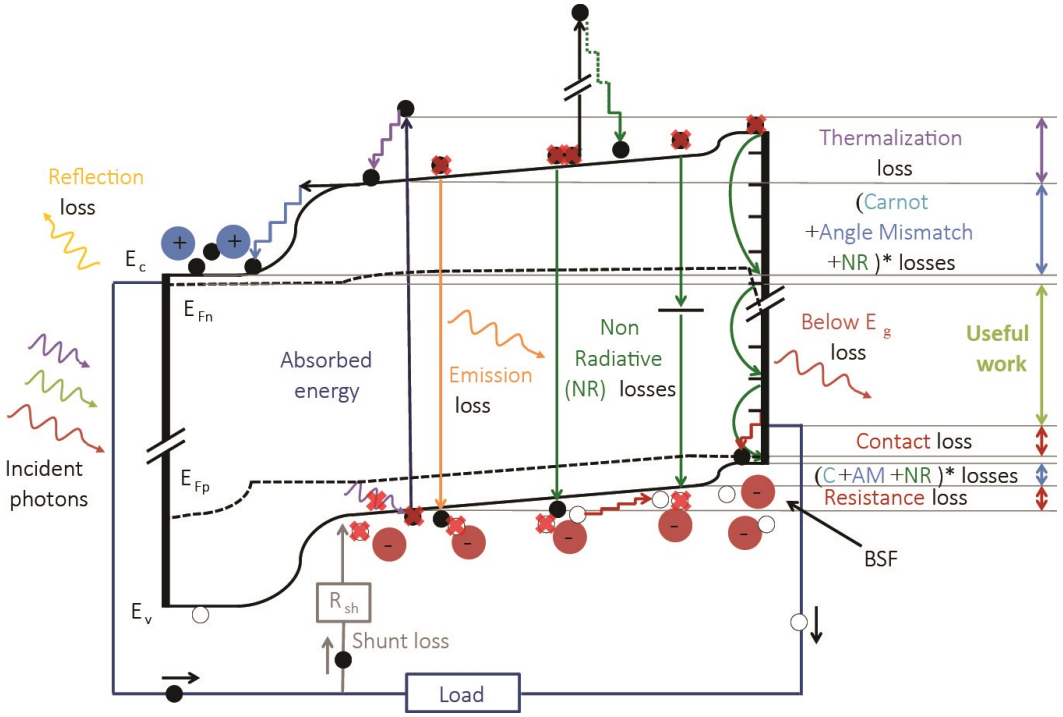

Fig. 1.5: The solar cell p-n junction diagram indicating the energy loss mechanisms in a standard single junction photovoltaic device. Adapted from [79].

1.1.1 Energy loss mechanisms

The device efficiency is lower than its theoretical maximum, the SQ limit, and on its turn, the SQ limit is always < 1 because many factors limit the performance of an ideal device. The loss mechanisms which affect solar devices are briefly discussed (see Fig. 1.5).

- *Optical losses*: light impinging on the solar cell is partially reflected at every interface, because of the refractive index variations; since absorption is a statistical phenomenon, there is a probability for which photons can be transmitted instead of absorbed.
- *Spectral mismatch losses*: photons with energies above E_g generate carriers which lose the energy excess by thermalizing to the band edge (*thermalization losses*), whereas photons with energies below E_g, cannot be absorbed.
- *Recombination losses*: the excited charge carriers can recombine before being separated by the junction built-in field or by involving a third particle. The latter process is called *Auger recombination*. The recombination events, can be divided in two types: band-to-band direct recombination and multi-step defect levels aided recombination or *Shockley-Read-Hall recombination*. Furthermore, recombination events can be radiative or non-radiative. In the first case, photon

emission occurs: the photon could leave the material or be re-absorbed. In the latter case, carries could recombine by giving their energy to the lattice by phonons creation. Auger recombination takes place when an electron-hole pair recombines transferring its energy to a second excited carrier, which will quickly thermalize back on the band edge.

- *Transport losses*: three main loss mechanisms are involved in charge carrier transport process. The first one is called *junction loss* and is due to the bands energy misalignment across the p-n junction: when carriers have crossed the p-n junction, they lie above the band edge, and thus they quickly relax colliding in their motion with lattice atoms. The second loss mechanism is called *contact loss* and its origin is again a bands energy misalignment between the semiconductor and the metal contact needed for extracting charges, in other words it is necessary to spend energy to extract carriers across the metal-semiconductor junction. The last contribute is the *series resistance (R_S) loss*: carriers during their entire path toward the load lose part of their energy by colliding with lattice atoms thus heating the device by Joule effect.
- *Shunt losses*: the presence of low resistance paths due to defects, impurities, across the device edges, or across an incompletely formed junction provides alternative paths for charge carriers which result in recombination losses and thus in barrier height reduction.

1.2 Tin sulphide: state of the art

Tin sulphide is a IV-VI semiconductor material (chalcogenide) constituted by non-toxic and Earth abundant tin and sulphur. SnS is characterized by an indirect band-gap of about $E_g \approx 1.0$ eV and a direct band-gap in the range $1.3 \div 1.5$ eV depending on the deposition technique[18], and an absorption coefficient > 10^4 cm^{-1} above the direct absorption edge[19]. SnS exhibits intrinsic p-type conductivity with a charge carrier density of about 10^{15} cm^{-3}.[19] Tin sulphide crystallizes in an orthorhombic structure, forming layered structures weakly bounded by Van der Waals forces[20]: this feature makes SnS surface chemically inert[18]. All these properties make SnS a promising candidate as an alternative light absorber layer for thin film photovoltaic applications.

Tin sulphide has been firstly proposed for photovoltaics about 30 years ago by Engelken *et al.*[21], and in 1994 Noguchi *et al.*[19] reported the first SnS-based working solar

cell exhibiting a power conversion efficiency η ≈ 0.3 % (n-CdS/p-SnS heterojunction). Starting from this work, SnS has been widely investigated, although accordingly to Banai *et al.*[22] inconsistent SnS optoelectronic properties are reported in literature, and this is mainly due to the fact that the relationship between microstructure and SnS properties is still unknown. Thin films of SnS have been prepared for photovoltaics application by several deposition methods, but every experimental technique results in a different SnS microstructure, and this influences SnS optoelectronic properties. Chemical bath deposition[21,23], electrochemical deposition[24,25], chemical vapour deposition[26–28], atomic layer deposition[16,18], spray pyrolysis[29,30], thermal evaporation[19,31–33], sputter deposition[34-36], and Sn sulfurization[37,38] are some examples of the investigated SnS deposition methods. Thanks to its optoelectronic properties SnS has been used also in other PV fields like inorganic-organic heterojunction solar cells[39], nanowire-based solar cells[40], and photoelectrochemical cells[41].

The current best working device has been presented by Sinsermsuksakul *et al.*[16]. They produced their record sample in substrate configuration using the glass/Mo/SnS/SnO_2/N:Zn(O,S)/ZnO/Sn:In_2O_3/Al stack, see Fig. 1.6.

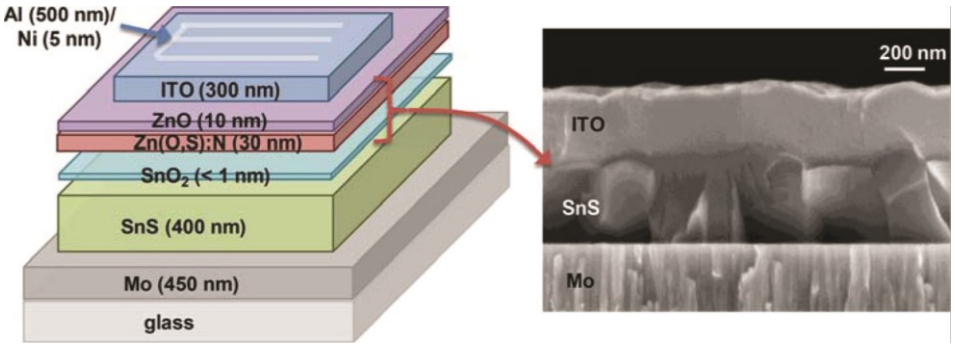

Fig. 1.6: The best SnS-based working device presented by Sinsermsuksakul et al.[16].

A thin 400 nm-thick SnS absorber layer is deposited by Atomic Layer Deposition (ALD) on a Mo back contact substrate. The SnS layer is subsequently annealed in H_2S atmosphere to enlarge SnS grains and thus to reduce recombination loss at grain boundaries. The SnS surface is then oxidized before junction formation to suppress recombination centres close to the junction region. The p-n junction is formed by depositing 30 nm of nitrogen doped Zn(O,S): this layer is deposited by ALD by alternating cycles of ZnO deposition with cycles of ZnS deposition with a specific ZnO:ZnS cycle ratio; nitrogen doping requires a further step after every ZnO cycle. The tin doped In_2O_3 (ITO) transparent front contact layer is deposited by RF sputtering after the atomic layer deposition of a thin ZnO passivation layer, required to protect the underlying layers. The

device is completed depositing a Ni/Al metal contact. The device described here exhibited the world record certified power conversion efficiency η = 4.36 % (0.232 cm^2 active area).

Atomic layer deposition is a challenging technique for industrial scaling, because of its slow deposition rate (typical ALD deposition rate ≈ 0.004 nm/s[32]). Other deposition techniques, such as thermal evaporation, are more suitable for industrial scale-up. Steinmann *et al.*[32] demonstrated that it is possible to produce SnS-based solar devices exhibiting good power conversion efficiencies by thermal evaporation technique. They deposited a 1.2 µm-thick SnS layer by thermal evaporation and maintained the main structure optimized for the case of Sinsermsuksakul *et al.*[16] (see Fig. 1.7). This device exhibited a certified power conversion efficiency η = 3.88 % (0.25 cm^2 active area).

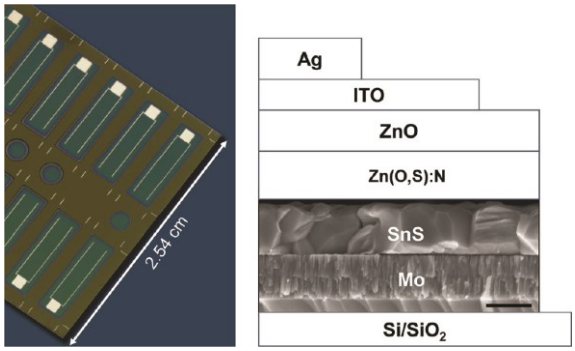

Fig. 1.7: Steinmann et al.[32] presented the best working device with the absorber deposited by thermal evaporation. Figure from [32].

1.2.1 Background on tin sulphides

In the work of Steinmann *et al.*[32] the congruent evaporation of SnS is demonstrated and the evaporation coefficient α_v value far from unity (α_v = 0.34) is confirmed.

Wiedemeier et al.[42] demonstrated that the dominant SnS vaporization process is sublimation. Furthermore, Piacente *et al.*[43] demonstrated that other sulphides – SnS_2 and Sn_2S_3 – vaporize through the following reactions.

$$\mathrm{SnS}(s) \rightarrow \mathrm{SnS}(g) \tag{1.3}$$

$$\mathrm{SnS_2}(s) \rightarrow \frac{1}{2}\mathrm{Sn_2S_3}(s) + \frac{1}{4}\mathrm{S_2}(g) \tag{1.4}$$

$$\mathrm{Sn_2S_3}(s) \rightarrow 2\mathrm{SnS}(s) + \frac{1}{2}\mathrm{S_2}(g) \tag{1.5}$$

Steinmann *et al.*[32] also emphasized that the 99.5 % pure SnS powder they purchased from Alfa Aesar were pure in composition, but contains significant quantities of SnS_2 and Sn_2S_3 phase impurities. They reported that the SnS powder annealing at 500 °C for

60 minutes under vacuum were able to remove any detectable signal from phase impurities.

Since Sn has two possible valences – Sn^{2+} and Sn^{4+} – SnS can form different phases accordingly to its actual composition. Burton and Walsh[44] investigated the phase stability of tin sulphides SnS, SnS_2, and Sn_2S_3. The SnS stable phase at room temperature is α-SnS with orthorhombic structure (space group *Pnma*, Fig. 1.8-a): it is a layered structure due to the arrangement of the tin lone pair electrons. The SnS phase is also known as Herzenbergite from the mineral name. Because of its layered structure, SnS is a highly anisotropic material and this is reflected on its properties. A different orthorhombic phase (space group *Cmcm*, Fig. 1.8-c) forms at high temperature: β-SnS. Other phases are the rock salt phase (space group *Fm-3m*, Fig. 1.8-b) and the zinc blende phase (space group *F-43m*, Fig. 1.8-d). These high energy SnS phases can form when SnS is deposited by high energy deposition methods (such as sputter deposition or pulsed electron deposition)[22].

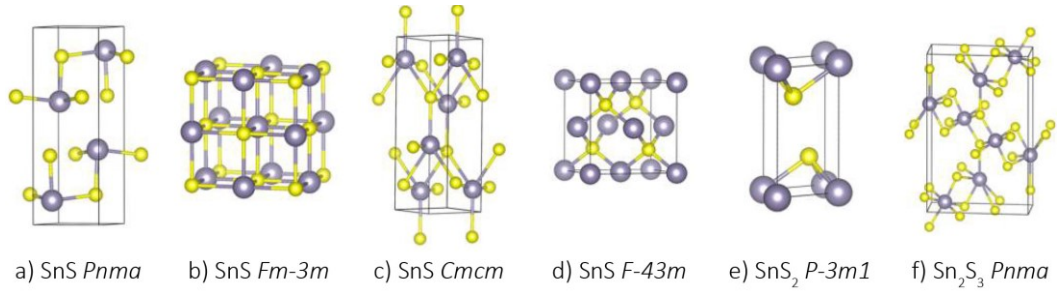

Fig. 1.8: Crystal structures SnS (tin atoms are grey, sulphur atoms are yellow) and the ground-state structures of SnS_2 and Sn_2S_3. Adapted from [44].

Burton *el al.*[45] also studied the properties of SnS, SnS_2, and Sn_2S_3 single crystals. In SnS, tin has its divalent form, whereas in SnS_2, tin has its tetravalent form. Sn_2S_3 is a multivalent compound and it can be correctly described as Sn(II)Sn(IV)S_3. These facts can be correlated to the material conductivity: divalent Sn is associated with hole conduction (i.e. SnS ↔ p-type conduction) and tetravalent Sn with electron conduction (i.e. SnS_2 ↔ n-type conduction). Sn_2S_3 could exhibits both p- and n-type conduction[22]. Burton *el al.*[45] also stated that a deviation from ideal stoichiometry of only 15% is enough to change SnS conduction from p- to n-type, and that deviations from ideal stoichiometry could be the reason for poor SnS-based device performance.

Vidal *et al.*[46] calculated the formation enthalpy for the six basic defects in SnS: tin and sulphur vacancies (V_{Sn}, V_S), tin and sulphur interstitials (Sn_i, S_i), tin-on-sulphur and sulphur-on-tin (Sn_S, S_{Sn}) antisite defects. Their results are shown in Fig. 1.9.

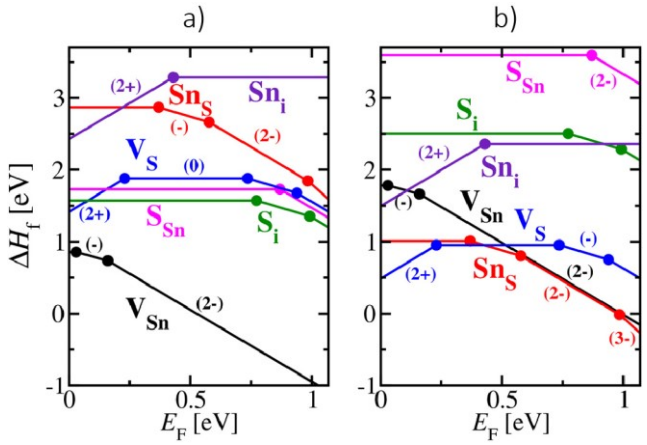

Fig. 1.9: Calculation of the formation enthalpies of intrinsic defect of SnS in the (a) S-rich and (b) Sn-rich limits. Adapted from [46].

Since the sulphur vapour pressure is very different (higher) than the tin one[22], it is challenging to produce stoichiometric SnS thin films (or to anneal SnS thin films keeping unchanged the Sn:S ratio). The calculation has thus been performed in two limits to consider this aspect: Sn-rich and S-rich SnS. In the first case, V_{Sn}, V_S and Sn_S antisite defects have a sufficiently low formation enthalpy to modify SnS properties. The authors ascribed SnS p-type conductivity to V_{Sn} which generate shallow acceptor-like vacancy defects. Sulphur vacancies generate instead donor-type defects. Since the formation enthalpy of V_S states is larger than the one for V_{Sn}, and the energy of sulphur vacancy defect states lie close to the valence band maximum, the V_S defects ineffectively compensate the positive carrier excess due to tin vacancies. Moreover, V_S and Sn_S antisite can cause the presence of deep gap states which are detrimental for electric transport properties. V_S could even cause tin to change to is +IV oxidation state in correlation to an atomic relaxation effect. Since in the S-rich SnS limit, only V_{Sn} defects resulted to have a low formation enthalpy, the authors suggested to move toward this direction enough to avoid the formation of the other defects but not much to favour the formation of sulphur rich secondary phases, i.e. SnS_2 and Sn_2S_3.

1.2.2 Post deposition annealing

Sulphur high vapour pressure – i.e. S volatility – is not necessary a negative feature of tin sulphides, in fact the possibility to produce SnS by a post deposition annealing of a SnS_2 thin film has been successfully reported[47]. The SnS_2 thin films were deposited by sputter deposition, and the resulting SnS films exhibited improved properties than SnS sputtered thin films[48].

Thermal annealing is a common procedure in metallurgy and material science. In the thin film semiconductor field, thermal annealing is a process used to favour atoms re-arrangement and grains growth to improve crystallinity and thus optoelectronic properties. In the case of SnS, many studies on the effects on SnS thin films of thermal annealing in different environment (vacuum, air, inert atmosphere, sulphur atmosphere, or H_2S atmosphere) have been performed.

Devika *et al.*[49] reported that the thermal treatment of SnS under vacuum led to an increment of the Sn/S ratio – i.e. sulphur loss – which grows linearly with the treatment temperature, and a reduction of grain size and SnS resistivity. Annealed SnS thin films exhibited a higher transmittance which the authors eventually ascribed to a reduced thickness or to the stoichiometry variation effects on optical properties of the films. According to their XRD spectra, their samples seem to be free from secondary phases both before and after thermal annealing (in all cases, their Sn/S ratio is bigger than one). Ogah et al.[50] reported instead the opposite: grain size and SnS resistivity resulted increased as a consequence of the annealing process, and the treated film exhibited a lower transmittance which is ascribed to the improved crystalline properties of SnS. The thermal treatment was not able to remove secondary phases from their samples.

Ikuno *et al.*[35] reported that the annealing in air of their glass/Sn:In_2O_3/$Zn_{1-x}Mg_xO$/SnS stack (superstrate configuration) was a critical step necessary to obtain the required diode properties. They deposited a very thin absorber layer (50 nm-thick SnS) and despite this fact, their solar device was able to reach a power conversion efficiency $\eta = 2.1$ %. The authors attributed this result to the conduction band offset obtained by pairing SnS with an optimized $Zn_{1-x}Mg_xO$ n-type buffer layer. Also Ristov *et al.*[51] investigated the effects of thermal annealing of SnS layers in air. They showed that a short treatment in air – 30 minutes – at 285 °C resulted in the change of the conductivity (from p- to n-type) with no detectable modification to film structure. By extending the treatment to 4 hours, the sample composition became a mixture of SnS and SnS_2, whereas a further extension of the treatment to 24 hours resulted in the complete transformation in SnS_2, with only traces of SnS. The treatment at higher temperature led to the formation of SnO and SnO_2.

To prevent SnS oxidation, the annealing could be performed in inert atmosphere (N_2 or Ar). Ghosh et al.[52] investigated the SnS recrystallization process by annealing in Ar environment for several treatment temperatures and durations. The annealing treatments under inert atmosphere did not lead to neither conductance type variation –

i.e. all samples remained p-type – nor to secondary phases removal. At every annealing temperature, samples suffered from desulphurization, in particular the thermal treatment at 400 °C resulted in the segregation of tin phase. Sample morphologies have been influenced by thermal treatment at high anneal temperature only, where grains coalescence took place.

Thermal annealing of SnS in H_2S atmosphere has been investigated in several works[16,38,53,54]. This thermal treatment is one of the key factor which leads Sinsermsuksakul *et al.* to reach their world record efficiency device[16]. Since thermal annealing in vacuum, air and even inert atmosphere of SnS samples caused sulphur loss and the consequent creation of sulphur vacancies and the discussed detrimental effects V_S could cause to a solar device, the annealing in H_2S atmosphere can be an attempt to suppress V_S creation. This treatment caused ALD-SnS grain size to increase, almost halved film resistivity and triple hole concentration[55]. Similarly, Hartman et al.[54] reported a non-negligible grain growth and coalescence for vacuum evaporated SnS annealed in H_2S atmosphere. They also demonstrated a performance increase of about 0.6 % by adding the H_2S treatment to their samples – from η = 3.0 % for no H_2S annealing, to η = 3.6 % for annealed sample.

All the thermal treatments described above have been investigated as a possible way to improve device performance by improving the SnS layer crystallinity; only in the H_2S case a performance improvement has been reported.

1.2.3 The n-type partner for p-SnS

Despite its toxicity, CdS is one of the most used partner n-type semiconductor. CdS is successfully used with CdTe, CIGS, and CZTS p-type absorbers. In the case of SnS, Sugiyama *et al.*[17] calculated from XPS measurements the energy band diagram for the CdS/SnS heterojunction, which resulted to be a type-II hetero-structure. A type-II hetero-structure is not the ideal structure for photovoltaics application. A negative conduction band offset, which in the CdS/SnS case is about ≈ -0.5 eV[31,56], could led to interface recombination preventing the device to exhibit good performance (see Fig. 1.10-a). Similarly, a large positive conduction band offset could cause the back diffusion of photoelectrons into the absorber by preventing their collection[57] (Fig. 1.10-c). A small positive conduction band offset is a reasonable compromise to reduce interface recombination and photoelectron loss (Fig. 1.10-b).

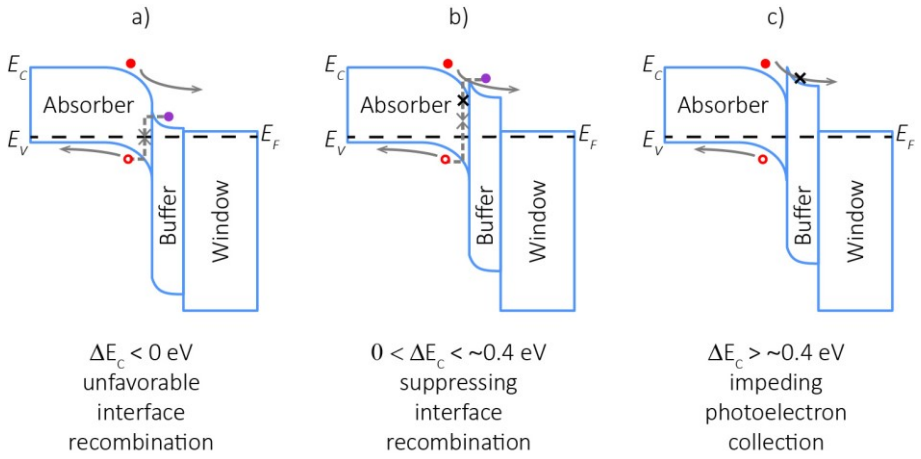

Fig. 1.10: Charge carriers transport properties are influence by the conduction band offset (ΔE_C) between absorber and buffer layer. Adapted from [55].

Sugiyama *et al.*[58] investigated many n-type semiconductors as possible partners for high efficiency SnS solar cells. They found that it is possible to form type-I hetero-structure by pairing p-SnS with $ZnIn_2Se_4$ or $Zn_{1-x}Mg_xO$ (with $0 \leq x \leq 0.3$). The latter has been investigated by Ikuno *et al.*[35]. Other investigated n-type buffer layer are for example InS_xO_y[56], $Cd_{1-x}Zn_xS$[25]. It is necessary to mention also Zn(O,S) since it is the buffer layer which led Sinsermsuksakul *et al.*[16] and Steinmann *et al.*[32] to achieve the two highest power conversion efficiencies for SnS-based solar cell.

1.3 Conclusion

In this thesis, some aspects of SnS – tin(II) monosulphide – will be investigated as an alternative inexpensive and non-toxic absorber layer for thin film photovoltaics. The deposition apparatus for SnS thermal evaporation will be described, its limitations will be pointed out, and our attempt to solve these issues will be discussed. The starting point for our investigations has been the standard CdTe solar cell developed in our laboratory (LAPS – Laboratory for Applied Physics, University of Verona). This means that we adopted the superstrate configuration to produce our standard glass/Sn:In_2O_3/ZnO/CdS/SnS/Au stack devices, and that we used the CdS/SnS heterojunction despite its known limitations. We will compare our results to those of literature – in particular with those of Schneikart et al.[31] which studied a very similar device. We will discuss a performance reproducibility issue which affected our samples, focusing the attention on what we think to be the origin of this phenomenon. Since the best performance we obtained is far from the theoretical limit, we will investigate post deposition thermal treatments as tools for

improving SnS crystalline quality and thus SnS solar device performance. We will apply two group of thermal treatment, those in vacuum and controlled atmosphere, and those in air, and the results will be discussed. In the last part of the thesis, we will leave our standard SnS device stack: alternative transparent conductive oxides, buffer layers and back contact will be investigated and compared with the standard ones, and the new properties of our device will be discussed.

Chapter 2.

THIN FILM SOLAR CELLS: DEPOSITION AND CHARACTERIZATION

During my research activity, I focused my attention on the design, production and characterization of CdS/SnS thin film solar cells.

In this chapter, the typical production process of these solar cells will be described, and in the following the main parameters involved in their electrical characterization will be presented. The current-voltage characteristic will be further discussed. Finally, the experimental techniques used to characterize the produced samples will be shortly described. Atomic Force Microscopy (AFM), Scanning Electron Microscopy (SEM), Energy-Dispersive X-ray spectroscopy (EDX), X-Ray Diffraction (XRD) and Raman Spectroscopy will be briefly introduced.

2.1 The CdS/SnS thin film solar cell production process

A thin film solar cell device is produced as a stack of different thin layers subsequently deposited on a substrate, by using different experimental techniques. A detailed

description of the deposition techniques will be given in Chapter 3. The production procedure of a solar cell is outlined in Fig. 2.1.

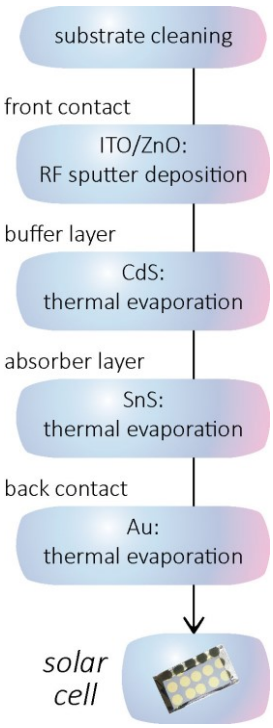

Fig. 2.1: Outline of thin film solar cell production.

The standard device is a CdS(n)/SnS(p) heterojunction deposited in superstrate configuration. A bilayer of tin doped indium oxide (ITO) and zinc oxide is used as TCO. The back contact (BC) is constituted by a thin Au layer. Hence, the complete stack is glass/ITO/ZnO/CdS/SnS/Au.

The first step of the solar cell production process is the substrate cleaning. The chosen superstrate configuration requires a transparent substrate: soda lime glasses were usually used. The substrates are glass squares with a side of 3 cm, and 4 mm thick. The standard cleaning procedure requires three steps. After the removal of particulates using a compressed argon gun, the substrate goes through a mechanical brushing phase, intended to remove skin greasy residues from its surfaces by using commercial soap. The substrate is then rinsed with deionized water and subsequently placed in a beaker with deionized water on a hot plate at 100 °C for 20 minutes. During the last phase, the sample undergoes four subsequent ultrasonic baths (10 minutes per bath) with acetone, acetone, methanol and finally isopropyl alcohol. The substrate is finally dried with the compressed argon gun, to remove the solvent and to avoid its evaporation from the substrate.

The TCO layers are then deposited on the cleaned substrate by *RF magnetron sputter deposition* (Section 3.1.2). Both the 3 inch ITO and ZnO targets are purchased from Testbourne Ltd and are 99.99 % pure (ITO target have a 90-10 % weight fraction and a 99 % density). Once the deposition chamber reaches a pressure below 10^{-5} mbar, the deposition can take place. A 400 nm-thick ITO layer is firstly deposited in reactive atmosphere at a working pressure of $6 \cdot 10^{-3}$ mbar (argon fluxes at 50 sccm, oxygen at 0.3 sccm), and at a sputtering power of 160 W. During the deposition, the substrate temperature is kept at 400 °C. After the ITO deposition, the chamber is again evacuated and the system prepared for the ZnO layer deposition, without breaking the vacuum. The 100 nm-thick ZnO layer is deposited at the same working pressure, partial gas pressures, and substrate temperature of ITO, but the sputtering power is reduced to 60 W. Our TCOs exhibits an average resistivity $R_{SQ} \approx 10\ \Omega \cdot \square$, and an average light transmittance $T \approx 83$ %.

Industrial TCOs were also used

- ITO/ZnO coated glass from Arendi S.p.A., typical resistivity $R_{SQ} < 8\ \Omega \cdot \square$, and transmittance $T \approx 85$ %.
- NSG TECTM C15 (Fluorine doped tin oxide (FTO) coated glass) from Pilkington plc., $R_{SQ} < 15\ \Omega \cdot \square$, $T \approx 84$ %.

In last cases, the TCO substrate undergoes the same cleaning procedures described for glasses.

The sample is then moved into a second deposition chamber, where the buffer layer is deposited by *thermal evaporation* (TE). In this apparatus, CdS and CdTe are usually deposited. The deposition chamber is evacuated at a pressure below 10^{-5} mbar, and the annealing of the TCO substrate is performed before CdS deposition. The TCO is annealed at a temperature of 450 °C for 30 minutes, to prepare it to the consequent deposition of the buffer layer. For the CdS deposition, 99.999 % pure CdS lumps (3-12 mm) from Alfa Aesar were used. The material to be evaporated is hosted inside a molybdenum boat crucible which is heated by a DC current flowing through it. A 50 nm-thick cadmium sulphide layer is deposited at a substrate temperature of 100 °C, with an evaporation rate of 0.2÷0.4 nm/s. Finally, the buffer layer is annealed for 30 minutes at 450 °C without breaking the vacuum before the absorber layer deposition.

In our laboratory, it is possible to deposit the SnS absorber layer with three experimental techniques: thermal evaporation deposition, sputter deposition, and pulsed electron deposition. The current description refers only to the thermal evaporation

process. The deposition of the SnS layer is carried out in a third deposition chamber. This deposition apparatus is reserved to SnS thermal evaporation. For the detailed description of the evaporator machine see Section 3.2. The heating element for SnS deposition is a Knudsen crucible wrapped in a resistive wire. The source material is 99.99 % pure SnS lumps (1-6 mm) from Huizhou Tian Yi Rare Material Co., Ltd. Typically, the crucible is filled with ≈ 2 g of SnS pieces: this amount of material is enough for two subsequent deposition processes, after which the emptying, cleaning and refilling of the crucible is required. Once a pressure below 10^{-5} mbar is reached, the deposition of 2 µm-thick SnS absorber layer is performed by heating the substrate at a temperature of 270 °C, and by setting the evaporation rate at 0.5 nm/s.

Finally, the solar cell is completed with the deposition of the back contact. The sample is moved into the last deposition chamber, which is then evacuated. Once the base pressure ($P < 10^{-5}$ mbar) is reached, the deposition of a 50 nm-thick gold layer takes place without heating the substrate. The source material, 99.99 % pure Au pieces from Argor Heraeus, is hosted in a boat crucible for its thermal evaporation. The typical evaporation rate is 0.3 nm/s.

To generate high vacuum, each apparatus is equipped with turbomolecular pumps except for the SnS deposition machine, which is evacuated by a diffusion pump. Low vacuum is generated by rotary-vane or scroll pumps. All vacuum machines use infrared ceramic elements to heat up the substrate; the only exceptions are the CdS/CdTe machine, which uses halogen lamps, and the back contact machine, which does not need any heating element. Standard K type thermocouples are present in every machine to measure the temperature in situ. Water-cooled quartz crystal thickness monitors are used in all the apparatus to estimate layer thicknesses and to measure evaporation rate.

2.2 Device and materials characterization

To analyse sample properties, many tools were used. In the following sections, the most important ones will be described.

The main property of a solar cell device is its electrical behaviour. By measuring the current-voltage characteristic, we identify a set of parameters which defines the solar device performance.

The material characterization is performed with several techniques. Atomic Force Microscopy (AFM) and Scanning Electron Microscopy (SEM) were used to investigate film

morphologies. The chemical composition was measured by Energy Dispersive X-Ray Spectroscopy (EDX) which is a useful tool integrated in electron microscopes. As electrons are used as probe, we obtain information about the sample surface. X-Ray Diffraction (XRD) is a commonly used technique to obtain information about the microcrystalline structure. Raman Spectroscopy is used to observe the vibrational dynamic of a lattice, and to identify its constituents. However, Raman spectroscopy has a limited penetration depth.

Other techniques were used to characterize samples in detail, such as Capacitance-Voltage characteristic, 4 point probe resistivity measurement, spectrophotometry (to measure sample transmittance, to estimate film thickness and energy band gap), …, that will not be described here.

2.2.1 Current-voltage characterization

To measure the I-V characteristic of a solar device under illumination a light source and a tool to measure the current while sweeping over the appropriate voltage domain are needed.

The light source spectrum must resemble the terrestrial solar irradiation spectrum as much as possible. The blackbody radiation emission at a temperature of about 5800 K is a good approximation of the solar spectrum. A tungsten halogen lamp in combination with a xenon arc lamp are typically used to simulate the solar spectrum.

To allow the comparison among devices manufactured by different laboratories or companies, the measurement of a solar cell I-V characteristic has been standardized. The solar cell must be measured with a light spectrum called *Air Mass 1.5* (AM1.5), which considers the sunlight path inside Earth's atmosphere at a zenith angle of $z \approx 48\,°$ (this value corresponds to the Earth's most populated latitudes). The device must be measured under one Sun illumination condition, which corresponds to a light power of $Pin = 1000\ W/m^2 = 100\ W/cm^2$, at a temperature of 25 °C. The current I, is usually replaced with its current density J, which is the ratio between the current and the solar cell active area (expressed in cm^2).

As seen in Chapter 1, the ideal current density voltage characteristic of a solar cell follows equation (1.1). The performance of a solar cell is conventionally express by four parameters: the short circuit current density J_{SC}, the open circuit voltage V_{OC}, the fill factor

F.F., and the solar cell power conversion efficiency η. In Fig. 2.2, the parameters are plotted with a typical J-V curve.

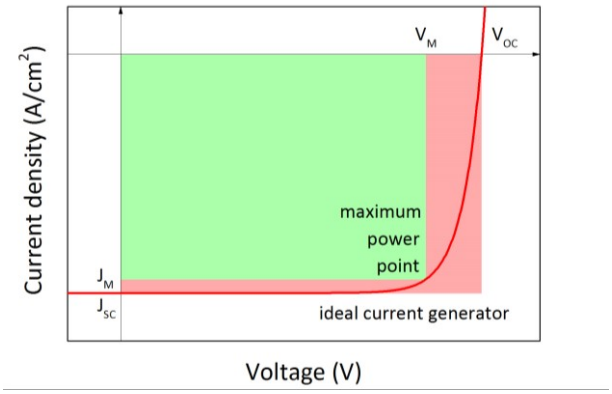

Fig. 2.2: The J-V characteristic of an illuminated solar cell.

The short circuit current density J_{SC} is the maximum current density that a solar cell can generate under illumination. Under short circuit condition means an applied voltage equal to zero. The value of the maximum power point current density (J_M) lies between $0 < J_M < J_{SC}$. In a similar manner, the maximum possible voltage in the fourth quadrant is reached under open circuit condition ($J = 0$ mA/cm^2) and its value is called open circuit voltage V_{OC}. The value of the maximum power point voltage (V_M) lies between $0 < V_M < V_{OC}$.

The fill factor indicates the rectifying ability of the p-n junction, or in other words, how much the device is close to an ideal current generator. The fill factor is defined as

$$F.F. = \frac{P_{Mreal}}{P_{Mideal}} = \frac{J_M \cdot V_M}{J_{SC} \cdot V_{OC}} \tag{2.1}$$

The power conversion efficiency of a solar cell device, already defined as the ratio between the output power and the input power, could then be expressed as a function of these parameters

$$\eta = \frac{P_{out}}{P_{in}} = \frac{J_{SC} \cdot V_{OC} \cdot F.F.}{P_{in}} \tag{2.2}$$

where P_{in} is the incident light power, as defined by the standard test conditions.

Two further parameters are used to give a more detailed description of the real device performance: the series resistance (R_S) and the parallel (shunt) resistance (R_P). The two loss mechanisms have been discussed in Chapter 1.

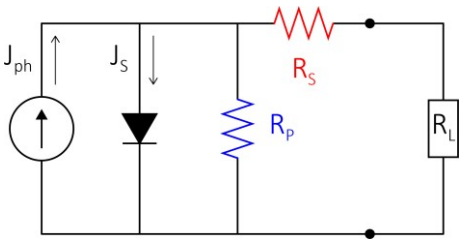

Fig. 2.3: The equivalent circuit of a solar cell. R_S and R_P take into account the series and shunt losses.

To take into account the contribution due to the two resistances, the equivalent circuit modifies as depicted in Fig. 2.3 and consequently the current density-voltage characteristic becomes

$$J = J_S\left[e^{\left(\frac{q(V-J\cdot R_S)}{n_{id}\cdot k_B\cdot T}\right)} - 1\right] + \frac{(V - J\cdot R_S)}{R_P} - J_L \qquad (2.3)$$

where the factor n_{id} is the ideality factor. This transcendental equation is not analytically resolvable.

A rough estimation of the parallel resistance could be done by calculating the slope of the J-V characteristic in J_{SC}. Similarly, a rough estimation of the series resistance could be calculated as the J-V curve slope in V_{OC}. The ideal device has $R_S = 0\ \Omega$ and $R_P = \infty\ \Omega$, any deviation from these values reduces both F.F. and η. The effects of R_S and R_P on the J-V characteristic are depicted in Fig. 2.4 and Fig. 2.5: increasing R_S the J-V characteristic tends to flatten towards the abscissa axis, whereas the decrease of R_P affects the J-V characteristic by changing the slope of the low voltage branch. In both cases the power density as well as the power conversion efficiency, and the fill factor decrease by moving away from ideality.

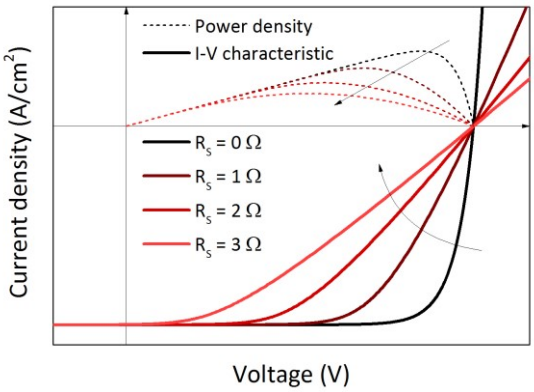

Fig. 2.4: The effects of the series resistance R_S on the J-V characteristic while increasing from its ideal value $R_S = 0\ \Omega$.

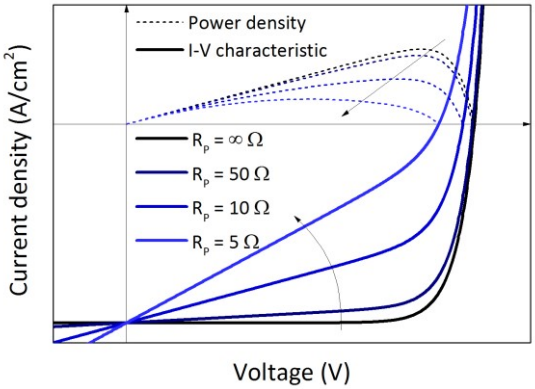

Fig. 2.5: The effects of the parallel resistance R_P on the J-V characteristic while decreasing from its ideal value $R_P = \infty\ \Omega$.

Current-voltage characterization @ LAPS, UNIVR

A home-made system was used to measure the solar device I-V characteristic. An Osram Decostar 51 superstar 4000 35 W 12 V 36° GU3.5 halogen lamp is used to simulate the solar spectrum. A silicon photodiode is used to calibrate the lamp power output to 100 W/cm^2. A Keithley 2420 Source Measure Unit remote controlled is used to measure the I-V curve. A National Instrument's LabVIEW® computer software drives the measurement by sweeping the typical voltage range -0.4 V < V < 1 V with 0.007 V steps. During measurements, sample temperature is not controlled, but is considered constant as sample exposure to simulated sunlight is limited in time (≈ 1 s).

2.2.2 Atomic force microscopy

Atomic Force Microscopy is a relatively young technique used to characterize samples surface properties with a very high resolution. AFM is a particular class of Scanning Probe Microscope, which uses a probe to scan a surface and consequently to form an image of the scanned area. The information contained in the image depends on the specific probe. The probe will measure its interaction force with the sample point by point; this interaction map will then be showed as an image of the surface topography. Moreover, it is also possible to obtain mechanical, optical, electrostatic and magnetic information by simply changing the probe.

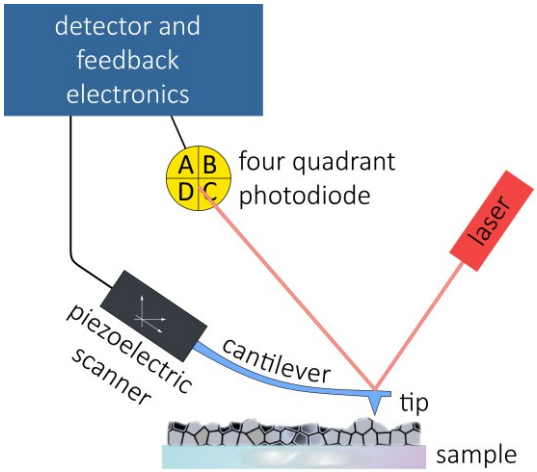

Fig. 2.6: Block diagram of an Atomic Force Microscope.

In Fig. 2.6 the basic elements of an AFM are sketched. The probe consists in a cantilever which ends in a tip; the probe tip is in direct contact with the sample surface and thus is subjected to van der Waals forces, causing the cantilever deflection. The tip is usually made of silica or silicon nitride, and has a typical height of tens of µm. A laser diode is used to transduce the cantilever deflection on a four quadrant photodetector – a position sensitive photodetector. The cantilever is placed on a piezoelectric scanner, with which the motion to scan the sample surface is obtained. This operating mode is called *contact mode*.

All the scans were taken instead in *semi-contact mode*, which means that the tip is kept close to the surface, but not in direct contact. In semi-contact mode the cantilever is placed on a piezoelectric crystal; the crystal drives the cantilever to oscillate close to its resonance frequency and with an amplitude of tens of nm. An electronic feedback circuit/actuator is used to keep constant the tip-surface distance, through a negative feedback circuit. The interaction tip-surface is thus so weak to cause only a variation in the amplitude of the oscillation of the cantilever. The semi-contact mode allows to preserve both the tip and the sample, since there is no contact between them.

Even the phase oscillations and the cantilever lateral deflections are usually recorded since they can give information about the local inhomogeneity of the surface (variation of elasticity, adhesion, friction, …).

AFM images can be affected by artefacts. The main sources of artefacts are

- The probe: its shape and size can modify the measurement resolution and lead to the so-called fat tip effect.

- The sample: while measuring the sample with low adhesion, debris could stich to the tip leading to the double tip effect.
- The piezoelectric scanners: scanners suffer from hysteresis effects, and have an intrinsic non linearity in their behaviour.
- External vibrations.

Atomic force microscopy @ LAPS, UNIVR

The thin films morphology was studied in our laboratory with a NT-MDT Smena-A Atomic Force Microscopy in semi-contact mode with NSG01 high resolution non-contact golden coated silicon AFM probes from NT MDT with nominal radius < 10 nm (cantilever length about 125 µm). Scans area were set to 60x60 μm^2, 30x30 μm^2, 10x10 μm^2, 5x5 μm^2 or smaller.

2.2.3 Scanning electron microscopy

Scanning Electron Microscopy is a microscopy technique which uses a collimated electron beam as probe. Electromagnetic lenses move the focused beam on the sample surface to scan it. Several detectors will record the emitted signal. When impinging, electrons interact with the sample many effects take place, and all of them give information about the sample topography and composition. SEM spatial resolution depends on the electron spot size (which depends in turn on electrons wavelength and the system used to focalize the beam), and on the *interaction volume* size – the volume where probe electrons interact with the sample. SEM magnification can reach 10^6 times, with a typical resolution of 10 nm.

In Fig. 2.7 is shown a schematic of the phenomena caused by the electrons-matter interaction.

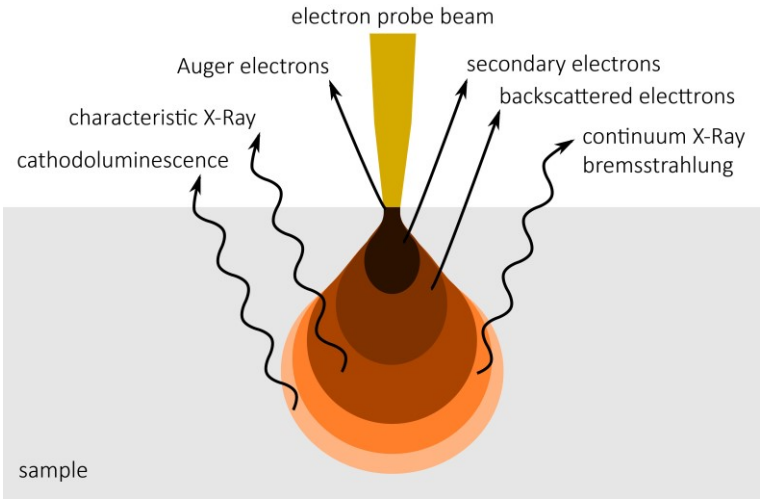

Fig. 2.7: Electron-matter interaction: the main phenomena and the typical "pear shape" interaction volume. Adapted from [80].

The interaction volume has a tear-drop shape and extends from hundreds of nm to few µm depending on the beam energy. From different regions of the interaction volume, different signals arise. Only the most relevant will be described here.

- Secondary Electrons (SE): this is the most commonly recorded signal used for studying sample topography. Probe interaction with sample can lead to the ionization of sample atoms – the emission of outer shells electrons or secondary electrons. These electrons are characterized by low energy (< 50 eV) and originate from a few nm from the sample surface.
- Characteristic X Rays: the emission of X-Rays leads to an analytical technique for elemental characterization known as Energy-Dispersive X-ray spectroscopy (EDX). X-Ray emission occurs when the incident beam knocks out an inner shell electron creating a hole; the system minimizes its energy when an outer shell electron migrates to the empty state, and its energy excess is dissipated by radiative emission. These photons are characterized by specific energies (X-Rays), typical of each chemical species. By collecting the characteristic X-Rays, it is thus possible to estimate the elemental abundance of the sample. Due to the low penetration depth of electrons in matter, EDX spectroscopy is considered a surface analysis technique.

Unlike AFM, generally SEM does not produce 3D images. In fact, even if the resulting images could be similar, the signal recorded by SEM depends mainly on the electron-matter interaction.

Scanning electron microscopy @ UNIVR

The SEM and EDX analyses were carried out at the Department of Neurosciences of the University of Verona with a Philips FEI XL30 Environmental Scanning Electron Microscope equipped with an Energy Dispersive X-ray analyser. Typical electron beam energies are in the 10÷25 kV range.

2.2.4 X-ray diffraction

X-Ray Diffraction is an analytical technique for phase identification and characterization of crystalline materials widely used in physic, material science, engineering, geology and biology.

In a crystalline material, its constituents are arranged in a highly regular structure called *crystal lattice*. The basic element is the *unit cell*, it is the smallest group of atoms that constitutes the crystal structure and defines the symmetry and structure of the whole crystal; to fully define the crystal, this basic element is translated in a repetitive way on all the points of the crystal; this array of discrete points is called *Bravais lattice*.

X-Rays could be used as a probe to investigate the crystalline structure of a wide range of samples, as their wavelength is comparable to the typical interatomic distances in crystals or molecules.

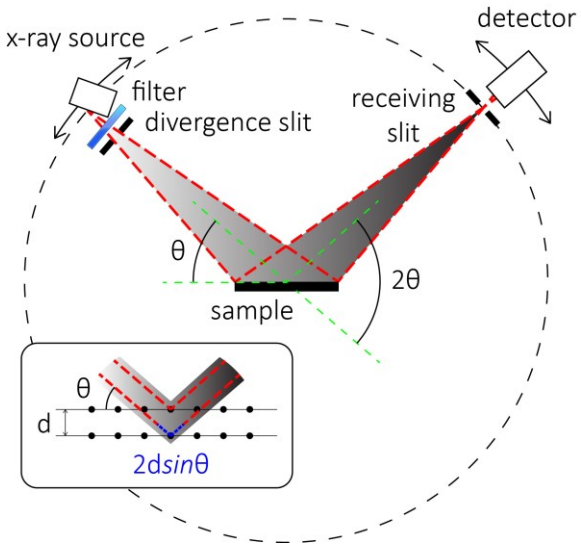

Fig. 2.8: The Bragg-Brentano geometry of a x-ray diffractometer. In the inset is highlighted the optical path difference which originates the diffraction pattern.

An x-ray beam, which impinges on a crystal, interacts with the electronic cloud of atoms and it is elastically scattered. For certain specific angles of incidence – which depends on the crystal structure – the Bragg's law (Eq. (2.4)) is satisfied and constructive

interference gives rise to a bright reflection (*Bragg's reflections*, Fig. 2.8-inset) of the incident beam.

$$n\lambda = 2d \sin\theta \tag{2.4}$$

For angles of incidence in which the Bragg's law is not verified, destructive interference occurs and there is no signal. The entire diffraction pattern of a sample can be recorded by scanning the sample at all the incident angles.

Modern diffractometer adopts the Bragg-Brentano geometry (depicted in Fig. 2.8): the source of X-Rays emits a divergent beam, which is focused on a circumference of radius equal to the source to sample distance. The detector lies on the same circumference. While the X-Rays source is scanning a sample moving of an angle θ, the detector is moving of an angle - θ. This geometry allows good peak intensities and high resolution.

From XRD data, it is possible to identify unknown phases, unit cell dimensions, sample purity; it is also feasible to determine crystal structures by Rietveld's refinement method, to determine lattice mismatch between films, to estimate stress and strain, as well as many other features.

X-ray diffraction @ UNIVR

All the XRD patterns were collected at the Solid State Chemistry Laboratory of the University of Verona with a Thermo ARL X'TRA powder diffractometer. The instrumentation works in Bragg-Brentano geometry, and it is equipped with an X-Ray source emitting at a wavelength of λ = 1.5418 Å by exciting a Cu-anode. The diffraction pattern is recorded with a Si (Li) solid state detector cooled by Peltier effect.

2.2.5 Raman spectroscopy

Raman spectroscopy is a non-destructive analytical tool, which uses visible light as probe to determine crystalline structure and chemical composition of a wide range of samples. It is widely used in many scientific areas. The light interaction with matter gives rise to the Raman effect, which is a very weak effect of inelastic scattering of photons; laser light is used to excite samples due to its very intense and highly collimated beam.

Micro Raman spectroscopy is a technique where a Raman spectrometer is combined with an optical microscope. Microscope optics will both focus incident light and collect scattered light. This setup allows to achieve high spatial resolution (< 1 um). With a Micro

Raman experimental setup, it is also possible to perform local measurement, to verify sample homogeneity, to map surfaces, ….

We describe the macroscopic phenomenon of Raman scattering by following a classical approach to the problem. This approach provides a consistent description of the phenomenon, although only the quantum mechanical description overcomes its limitations. For the complete description of the phenomenon, refer to ….

When a light beam impinges on a physical system (atoms, molecules, crystalline or amorphous solids, …), the incident photon electromagnetic field E, induces an electric field distributed among the system constituent, the scatterers: the system locally polarizes. Since the incoming electromagnetic field and the induced electric field are time dependent, the scatterers can be approximated as oscillating dipole moments P, which are the origin of scattered radiation. The incident field and the induced dipole moment are connected through the electrical susceptibility of the medium:

$$\boldsymbol{P} = \alpha \cdot \boldsymbol{E} \tag{2.5}$$

The properties of the medium are contained in the electrical susceptibility α.

The atoms in a solid oscillates around their equilibrium position with a characteristic frequency. These collective oscillations of atoms are called phonons: quasi particles characterized by a wave vector and a frequency. In first approximation, is it possible to write the induced dipoles as the sum of three contributes.

$$P = P(\omega) + P(\omega - \omega_k) + P(\omega + \omega_k) \tag{2.6}$$

The first term explains Rayleigh scattering – i.e. elastically scattered radiation – while the remaining two terms represent the Raman scattering: i.e. inelastically scattered radiation due to the modulation mechanism caused by phonons; the two terms are called Stokes and Anti Stokes scattering. The two signals are symmetrically shifted in frequency with respect to the excitation light frequency (Raman shift) and represent the cases in which photons give energy to the system by creating phonons (Stokes signal), and the case in which photons take energy from the system by destroying phonons (Anti Stokes signal). These phenomena are briefly shown in Fig. 2.9.

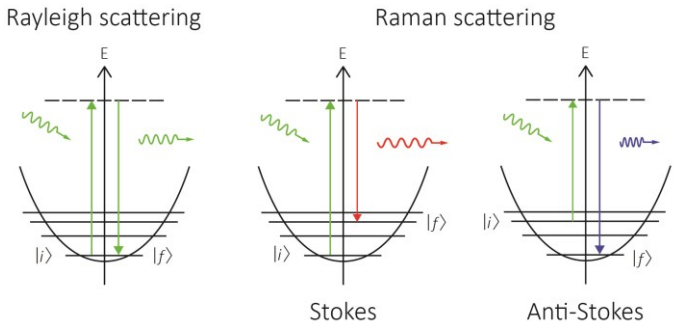

Fig. 2.9: A schematic of the physical interpretation of the Rayleigh and Raman scattering.

The Raman bands intensity, position and shape will give direct information about phonons in a material. Phonon properties strictly depends on many parameters, the main are crystalline structure and chemical composition of which it is thus possible to obtain indirect information. Since the technique is sensitive to local inhomogeneity, it is possible to study also crystalline defects, impurities, strain and to identify secondary phases.

Raman spectroscopy @ UNIVR

The Raman spectroscopy measurements shown in the present text were recorded at the Raman Laboratory of University of Verona. A He-Ne laser emitting at 632.8 nm was used to excite the samples. An 80x objective (NA = 0.75) is used to focus the laser beam to a spot size of about 1 μm^2. The acquisition system is a Horiba-Jobin-Yvon LabRam HR800 Micro-Raman microprobe (focal length of 80 cm, grating of 600 lines/mm) with a cryogenically cooled CCD detector. A notch filter is used to filter the elastically scattered light. Measurements resolution in this configuration is 1 cm^{-1}/pixel.

Chapter 3.

DEPOSITION TECHNIQUES AND EXPERIMENTAL APPARATUS

Three main deposition techniques were applied during the research activity. In the first part of this chapter Thermal Evaporation (TE) deposition and Sputter Deposition (SD) techniques will be briefly discussed.

TE and SD belong to Physical Vapour Deposition (PVD) methods, which are used to produce thin solid films by vaporization of a solid source material and its consequent condensation on a substrate surface without involving any chemical reaction.

Independently from the chosen experimental technique, the deposition of a thin film requires to follow three basic steps:

1. Generation of the vapour from the source material.
2. Transportation of the vapour to the substrate.
3. Condensation of the vapour on the substrate surface, and subsequent formation of the film.

All PVD techniques require the process to take place in vacuum. The required entity of vacuum strongly depends on the chosen deposition method. Generally high vacuum is always reached before deposition to minimize the possible contamination or interaction of particles with surrounding gases.

In the second part of this chapter, the SnS evaporation machine will be described. This apparatus required a constant development and maintenance to perform research activities on SnS thin film solar cells. Most of the apparatus subsystems have been developed or improved. The improvement of the systems and the reasons leading to it will be discussed, since this activity considerably increased the stability and the reproducibility of deposition process.

3.1 Deposition techniques

3.1.1 Thermal evaporation

Thermal Evaporation or Vacuum Evaporation is the basic PVD method. TE is one of the oldest coating technique, and one of the most widely diffused thin film deposition method, due to its simplicity and limited requirements, which make it an inexpensive technique. TE allows the deposition of both metals and metal alloys, as well as semiconductors, at a reasonable fast deposition rate. It is a low energy deposition process.

In the TE case, the vapour is generated by heating the source material – the evaporant – which is loaded into a container placed inside a vacuum chamber. The container could be a conductor (wires, coated dimpled boats, …) or not (graphite or ceramic crucibles, Knudsen cells, …); in the latter case the container needs a heating element like a resistive wire.

The evaporant must be heated to a temperature higher than its corresponding vapour pressure, value at which both solid and gas phases of the source material coexist. In general, the lower the chamber pressure, the lower the required temperature to generate the vapour.

The vapour flows from the container to the whole deposition chamber; vapour constituents travel with an almost straight path, and due to high vacuum inside the chamber their mean free path is increased, as the probability of collision with background gas molecules is minimized.

The mass evaporation rate from a free surface A_e follows the Hertz-Knudsen relation

$$\Gamma = \alpha_v \cdot (P^* - P) \cdot \sqrt{\frac{m}{2\pi m k_B T}} \qquad (3.1)$$

where α_v the sticking coefficient for vapour molecules onto the surface, m is the evaporant molecular mass, P* the equilibrium vapour pressure of the evaporant and is a

function of the temperature T and P the environment pressure. Evaporation from a free surface is isotropic whereas effusion (i.e. evaporation through an orifice) from a Knudsen cell follows an angular distribution and thus is said to be directional.

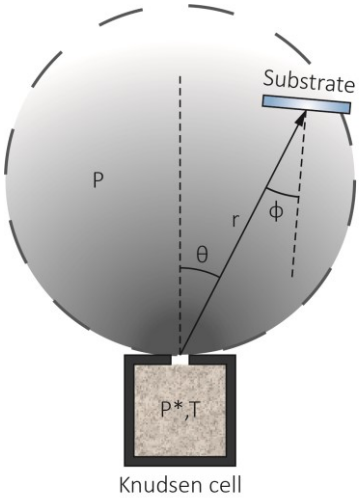

Fig. 3.1: Evaporation from a Knudsen cell. The vapour condenses on a substrate located at a distance r from the source. Adapted from [81].

In Fig. 3.1 the Knudsen cell case is depicted. The orifice is an evaporation surface of area A_e – the orifice area – at pressure P*. Thus, the mass deposition rate per unit of condensation surface dMc/dAc and per unit of time can be calculated:

$$\frac{dMc}{dAc \cdot dt} = \frac{\Gamma}{\pi r^2} \cdot cos\varphi \cdot \cos\theta =$$

$$= \alpha_v \cdot (P^* - P) \cdot \sqrt{\frac{m}{2\pi m\, k_B T}} \frac{1}{\pi r^2} \cdot cos\varphi \cdot \cos\theta \qquad (3.2)$$

This relation takes into account the mass evaporation rate Γ, which depends on the thermodynamic parameters of the system (source temperature, chamber pressure, evaporant vapour pressure and molecular mass) and geometrical factors (from which rises the cosine law angular distribution, which depends on Knudsen cell shape and orifice area, source-to-substrate distance, substrate position and orientation respect the source).

When the vapour reaches the substrate, its condensation on the substrate surface could take place with the consequent formation of the film. This process, see Fig. 3.2, could be considered as a sequence of the following steps:

1. Adsorption: molecules impinging on the substrate surface could adsorb when they could dissipate part of their momentum interacting electrostatically with the surface atoms; too energetic molecules will immediately reflect from the surface.
2. Diffusion: molecules trapped in a weakly-adsorbed state could spend their residue momentum diffusing from site to site, upon the surface (this is called "physisorption"); these molecules could furtherly interact forming chemical bonds with the surface atoms ("chemisorption"), or could even desorb by gaining enough energy during their migration.
3. Nucleation: adsorbed molecules could then interact one another, by forming firstly subcritical embryos, which grow to form critically sized nuclei.
4. Condensation: nucleation centres grow, becoming "island" clusters (island stage); clusters then coalesce into new bigger clusters (coalescence stage) which grow leaving empty holes and "channels" (channel stage). Finally, channels and holes fill and a continuous film is formed (continuous film stage).

The actual way in which the film forms depends on the local surface tension of the substrate. The fundamental parameter to control the condensation upon the substrate is its temperature. By increasing substrate temperature is it possible for example to increase the diffusivity of the weakly-adsorbed molecules, to shorten their residence time, or even to re-evaporate the film; the annealing of the deposited film is a common step, which could lead to its recrystallization.

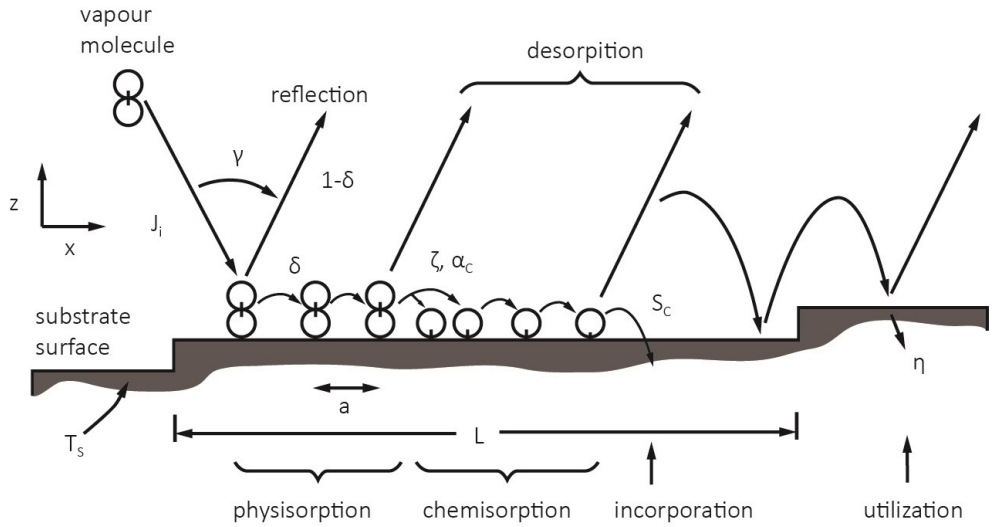

Fig. 3.2: Vapour condensation sequence on a substrate at a temperature T_S. Adapted from [82].

To sum up, TE is a low energy process with which it is possible to deposit thin films in high vacuum (sample low contamination), by simply heating the source material over its vapour pressure. Films structure is affected by the deposition geometry, and could suffer from limited uniformity and from a poor step coverage; in the case of multi-component source material, thermally evaporated films could suffer also from poor stoichiometry due to the different vapour pressures and so deposition rates of the source components.

3.1.2 Sputtering and sputter deposition

Sputtering is the physical phenomenon of particle ejection from a solid target material through its bombardment with an energetic ion beam. Sputtering is widely used for surfaces erosion (cleaning of surfaces, …), thin films deposition (coatings, …), and analytical analysis techniques (Secondary Ion Mass Spectrometry, …).

Sputter Deposition is a PVD technique that allows the deposition of a wide range of materials, both metals and dielectrics. Even if SD is technologically complex if compared to TE, SD is a widely diffused deposition method in industries since it permits to coat wide surfaces with highly uniform films.

The vapour generation that occurs during SD involves a non-thermal physical process – ion bombardment – to drive both the vapour generation and its transport to the substrate.

In the following only the so-called glow discharge sputter deposition technique will be described.

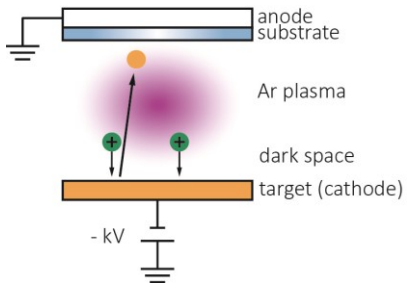

Fig. 3.3: Typical setup for DC sputter deposition. Adapted from [81].

The basic SD method is called DC sputter deposition (Fig. 3.3); the entire process can be described through the following sequence of events, which start with the evacuation of the vacuum chamber:

1. A low pressure (10^{-3} mbar) of inert gas, typically Ar, fluxes in the vacuum chamber.

2. A voltage of few kV is applied to two parallel electrodes, where the target (the source of material to be deposited) and the substrate are placed, respectively the cathode and the anode.
3. Stray electrons close to the cathode are driven and accelerated towards the anode; in their path, electrons can collide with Ar atoms giving place to two different phenomena: the excitation of Ar atoms (with the following radiative de-excitation) and the ionization of Ar atoms; in the latter case, two energetic free electrons can collide with other Ar atoms, and a cascade process brings to the plasma ignition.
4. Near the cathode, the ionization process is more probable than excitation: a dark region of positive ions forms there, causing voltage reduction and screening effects. When positive ions enter in the dark space, they are accelerated toward the target, thus ions bombard the target surface.
5. The interaction of impinging ions with the target surface can lead to several phenomena (see Fig. 3.4), which depend exclusively on the impinging ion energy: in the low energy regime (few eV), ions can be adsorbed or reflected, or (tens of eV) can damage the surface or cause target atoms migration; increasing ions energy (below few keV), sputtering of the surface happens, while in the high-energy regime (above tens of keV) there is ion implantation.

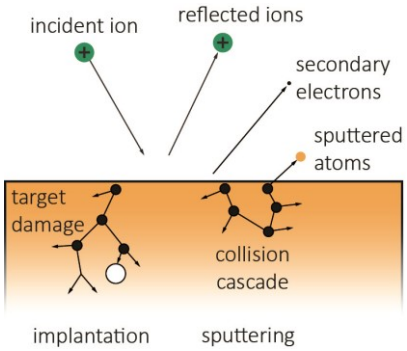

Fig. 3.4: The main phenomena of ion bombardment of a surface. Adapted from [83].

6. In the sputtering regime, every impinging ion dissipates its energy colliding with many target atoms in a process called “collision cascade”; energy and momentum are conserved in these collisions. After the collision cascade, there will be target atoms with enough energy and momentum to leave the target surface, and these are the sputtered atoms.

The most important parameter in sputtering theory is the sputtering yield Y which is defined as

$$Y = \frac{n.\,ejected\ atoms}{n.\,incident\ atoms} \tag{3.3}$$

the ratio between the number of the emitted particles and the number of incident particles. This parameter is proportional to the deposition rate, and depends on the nature of the target atoms, on their binding energy, on the relative mass of ions (Ar) and atoms (target) and on the energy and angle of incidence of ions.

The angular distribution of sputtered atoms follows the cosine law, similarly to TE.

Another important parameter which influences the deposition rate is the chamber pressure, and it is strongly related to the mean free path of sputtered atoms. In fact, if the pressure during sputtering is too low, the plasma will extinguish; on the contrary, if the pressure is too high, the sputtered atoms will collide many times before eventually reach the substrate, and this reduces significantly the deposition rate. These collisions can lead also to the adsorption of ions or neutralized Ar atoms on the substrate as impurities. The *magnetron sputter deposition technique* has been adopted to overcome this limitation by applying a magnetic field parallel to the target surface (refer to Fig. 3.5).

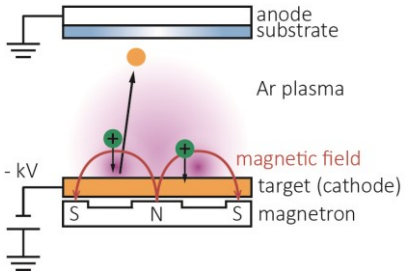

Fig. 3.5: Typical setup for magnetron sputter deposition. Adapted from [81].

In this case, electrons are confined in a region close to the target, where they move in a cycloid trajectory, and can contribute to sustain the plasma. The interaction of heavy Ar ions with the magnetic field is weak: this allows to reduce the required discharge pressure of orders of magnitude (increasing film quality), and to increase the deposition rate of orders of magnitude.

The DC sputter deposition technique described here cannot be used to deposit dielectrics; the Ar ions bombardment of an insulating target will result in the charging of its surface, thus the voltage between the electrodes will reduce to the point that the discharge extinguishes. The solution is called *radio frequency (RF) sputter deposition*

technique: in place of a DC voltage, an AC one is applied to the electrodes by coupling the system with an oscillating circuit (see Fig. 3.6).

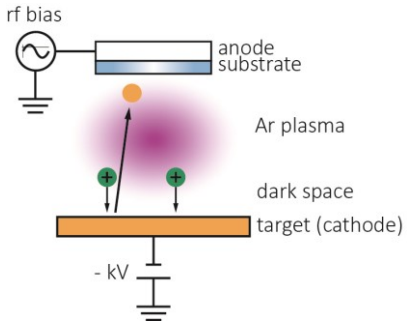

Fig. 3.6: Typical setup for Radio-Frequency sputter deposition. Adapted from [81].

The AC voltage drives free electrons to neutralize the positive charge which grows on both the electrodes. A high frequency, typically 13.56 MHz, is required to influence only electrons motion: during the positive cycle, electrons are attracted to the cathode creating a negative bias, whereas during the negative cycle, electrons increase plasma density. Heavy Ar ions do not follow the high frequency changing force, so the net effect is the continues bombardment of the target. Finally, both electrodes can be sputtered because a second dark space forms close the anode, but this effect is limited by using target with area smaller than the anode one (cathode dark space voltage become bigger).

It is possible to use different gases to form the plasma, inert gases like Ar or Kr are chosen as they will not react with the sputtered atoms to form compounds, thus to limit film contamination. By adding small molecular gases like N_2 or O_2, one deliberately chooses to let happen their reaction with sputtered atoms. This technique is called *reactive sputtering*. The reactive gases will chemically interact with the sputtered atoms and are usually used to deposit nitrides or oxides. The reactive gas flow can be used to control the film stoichiometry.

In conclusion, sputter deposition is a PVD technique where ion bombardment is the physical mechanism used to form the “vapour”. Sputtering is a high-energy process, which results in denser film with small grain size and a better adhesion, compared with TE. The low vacuum requirement means a higher contamination because the gas atoms can be implanted in the films. Moreover, SD allows a better step coverage and film uniformity than TE. Thanks to the erosion mechanism, the deposited film will have the same stoichiometry of the target, due to a self-regulation process.

3.2 The SnS thermal evaporation apparatus

The evaporation apparatus used for producing the SnS absorber layer is depicted in Fig. 3.7.

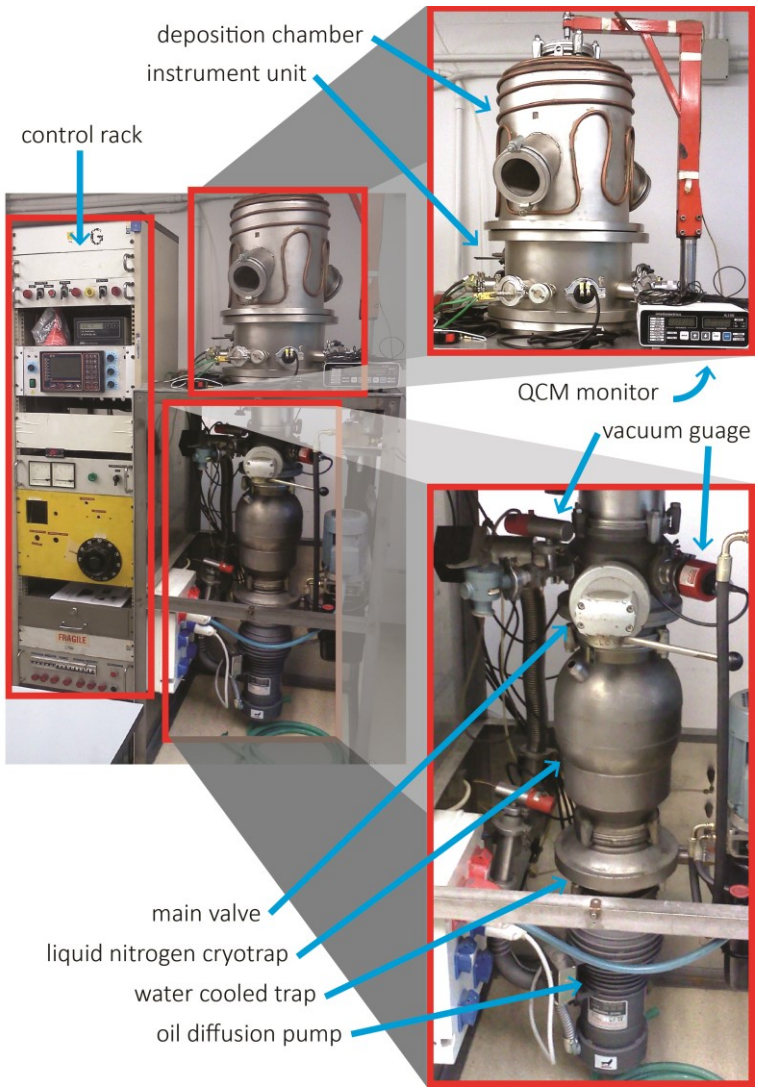

Fig. 3.7: The thermal evaporation machine used for tin sulphide deposition.

This apparatus consists in different parts that will be described in the follow.

- The vacuum needed for the deposition process is generated by an *oil diffusion pump*, which is located in the bottom part of the instrument; this pump is coupled with a powerful *rotary pump*, which provides the backing (not shown in Fig. 3.7).
- The vacuum column is divided in two regions by a manual valve, the *main valve*, which can isolate the principal chamber from the pumping system.
- An electro valve system allows the rotary pump to bypass the diffusion pump to obtain the pre-vacuum condition in the deposition chamber.

- Oil back streaming from the diffusion pump can contaminate the deposition chamber. To avoid this contamination, a *water-cooled trap* and a *liquid nitrogen cryotrap* are located between the diffusion pump and the main valve. These traps cool down the vacuum chamber walls, creating a region where oil and background gas molecules are easily adsorbed, with the consequent further decrease of the pressure.
- On top of the main valve there is the *instrument unit*, the part of the apparatus containing the hardware for the deposition processes. The evaporation sources are located here.
- Finally, on top of the whole system, there is the *deposition chamber*, that can be opened by uplifting the steel bell with a hydraulic arm (when the pressure difference is compensated).
- The deposition process is driven by the instrumentation located on the control rack.

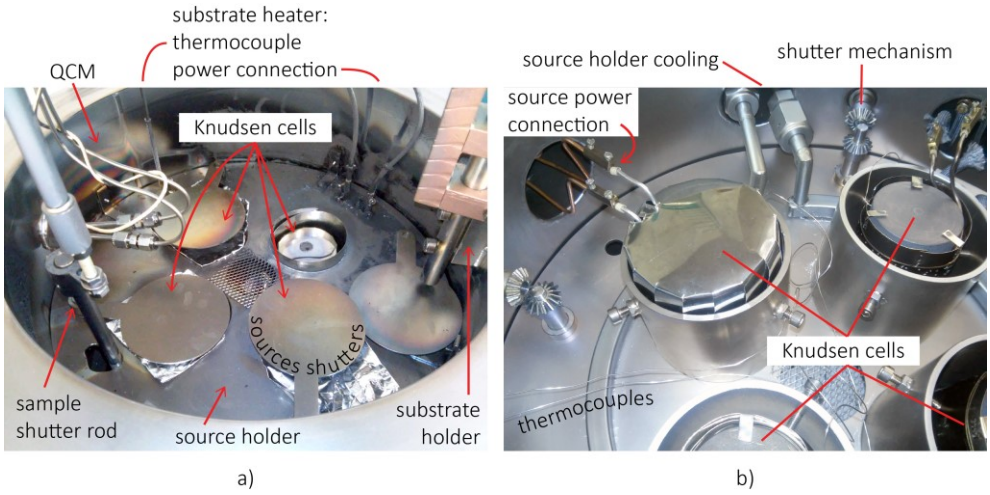

Fig. 3.8: The instrument unit seen from a) above and b) below. It is possible to see the four Knudsen cells housed in the source holder, the power connections without insulation, and their shutters.

Inside the instrument unit depicted in Fig. 3.8, there are:

- Four evaporation sources, i.e. four Knudsen graphite cells, each of which is heated up by a resistive wire. Each source and its heating wire are enclosed into a thin molybdenum foil, used to thermally isolate the source. Four shutters are located on top of the sources.
- The resistive wire, also known with the commercial name of *thermocoax*, is a coaxial one: the current flows in the internal wire heating it up by joule effect; the

external coating is metallic in order to transmit and withstand the heat, and it is electrically isolated from the internal wire.

- The sample holder (Fig. 3.9) is located above the sources, and its distance from the sources can be varied following the research needs. It carries only one sample at a time. Moreover, the holder provides sample heating with a dedicated thermocoax heating circuit.

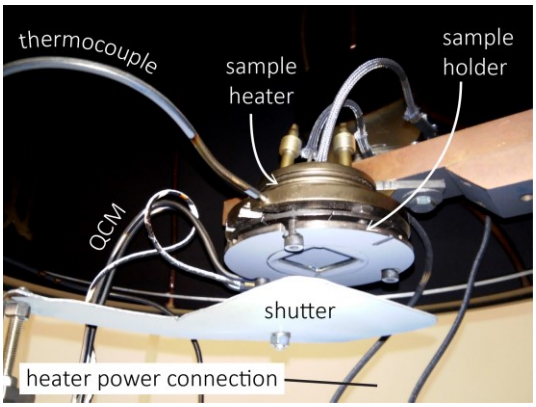

Fig. 3.9: The sample heater/holder.

- A shutter (Fig. 3.9) is used to control sample exposition to evaporating vapors.
- A water-cooled quartz crystal microbalance (QCM) is located at the same height of the sample, 2 cm far away from it. This is used to measure the deposition rate.

The instrument unit has ten KF-40 openings.

- Four of them are closed by plastic power feedthroughs used for the power supply of the four Knudsen cells.
- Two of them are utilized with custom thermocouple feedthroughs (two thermocouples per feedthrough); these thermocouples are used to measure the temperature at the source bottom.
- Another plastic feedthrough is used to feed the power to the sample heater and one other for the thermocouple measuring the substrate temperature.
- The last two feedthroughs are employed for the water cooling system and the signal of the QCM, and for the water cooling system of the sources holder, the steel plate depicted in Fig. 3.8, which houses the evaporation sources.

Every source is connected to a custom power supply (Fig. 3.10). It consists in a Pixsys ATR300 Process controller coupled with a Pixsys PL300 I/O Data acquisition/actuation module which control the sources through a feedback system. The operator can vary the maximum power to supply to the single source by using a variable resistor, and can

impose a temperature set point on the microcontroller. The microcontroller on its turn would read the source temperature, and calculate how to reach the set point through PID parameters. Moreover, the controller is connected to four power modules – Tecnel VM570 610 manual voltage variator, phase-controlled, for single-phase AC loads – which supply the power to the sources.

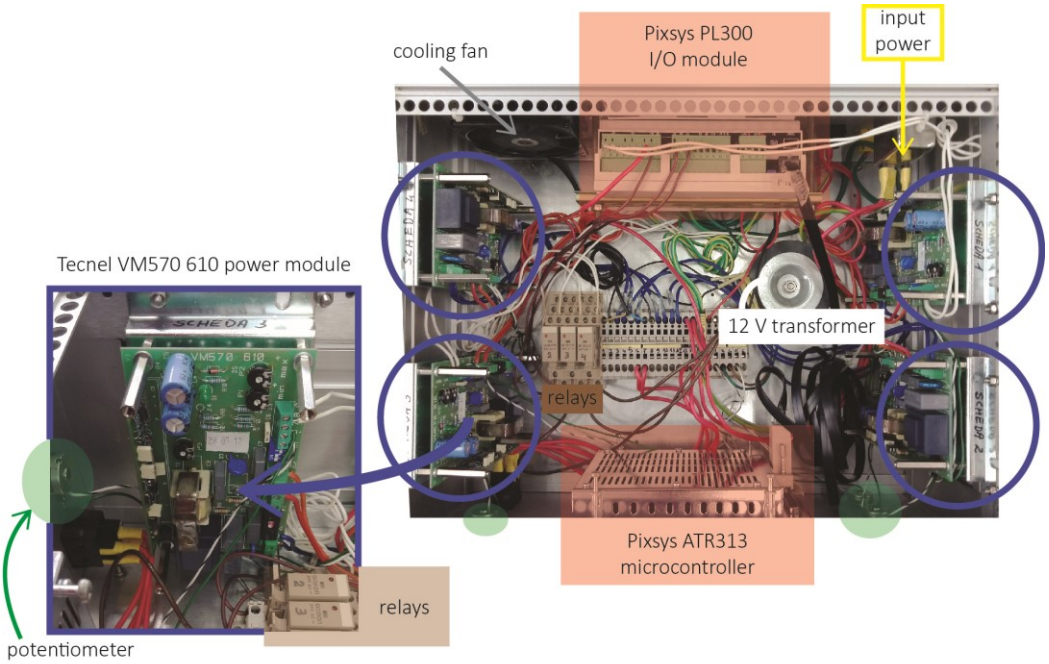

Fig. 3.10: The four sources custom power supply. The microcontroller drives the power modules to feed the sources.

A separate PID controller, model AC1-5J from LAE electronic, is used to supply the sample heater. Also in this case the operator can set the maximum power and the temperature, and the controller manages independently the apparatus. The power is set by using a Variac autotransformer.

3.2.1 Development of the deposition apparatus

Some parts of the evaporation apparatus were previously used for other applications. To remove elder deposition residues and avoid future contamination, the bell has been sandblasted before its use.

The instrument unit and its custom power supply were produced and purchased as a single block. These parts were realized at Tecna S.r.l. in Parma for this instrument, and they were designed for the co-evaporation of four different materials from four sources, with the aim of using the apparatus for a new research branch in the emerging field of CZTS quaternary solar cells.

However, even if the power supply was designed to control four sources, it can manage only two separate processes at a time, and thus it is not able to control the four sources needed for the co-evaporation of the single components of CZTS. For some reason, the Pixsys microcontroller memory corrupted before I started my PhD, and this required its reprogram. During the study on the electrical system that I performed in the first months of my research activity, it was clear that the power supply was not able to modulate the power feed by the power modules: it can only switch on and off the output in the so-called time-proportional control. Furthermore, the power modules are not designed for supplying all the needed power to the sources (further details will be discussed), and thus their time-proportional automatic control has never been used: the sources were driven in the manual operation mode.

However, my PhD project was focused on the deposition of a binary semiconductor, the tin sulfide as solar cells absorber layer. The apparatus so far described was thus used for this purpose. It was programmed to deposit SnS thin films by the co-evaporation of Sn and S from two distinct sources. However, the instrument unit designers underestimated the requirements for the Sn evaporation.

At the beginning of my research activity, the first step was the assembling of the apparatus, and then the first tests were performed.

1. **Vacuum test.** The vacuum pressure required to guarantee thin film depositions without contamination by background gases is below 10^{-5} mbar. We experienced a non-optimal vacuum level in comparison to the potentialities of the pumping system. The main causes of this problem were essentially two: 1. after the sandblast of the bell, the apparatus was not adequately cleaned, and 2. the system was subjected to vacuum leaks due to its complexity. We found the main leak sources being one faulty O-ring and the five plastic electric power feedthroughs: in fact, when the related load was active, the feedthroughs were heated up by joule effect thus losing their vacuum sealing. The cleaning of the apparatus from sand residues, the substitution of the old and broken O-rings, and the substitution of the plastic feedthroughs with steel ones (from K.J. Lesker Company) were sufficient to reach an adequate pressure for the aim of the research.
2. **Substrate heater test.** We have encountered instability of the sample heating system, which was subjected to unexpected electrical failures. Several times these

failures caused the blowing out of the power of the entire laboratory, by switching off the general magnetic thermal circuit breaker of the laboratory (set to 63 A). We found the old variac broken, and thus we substituted the whole substrate heater system. A new substrate holder/heater system was designed and built (see Fig. 3.11); it allows the deposition on two samples at a time. The initial thermocoax heated copper plate was substituted with a more versatile IR ceramic heater, able to permit the study of a wider range of temperatures. This new prototype receives the power from an external power supply, shared with another deposition apparatus.

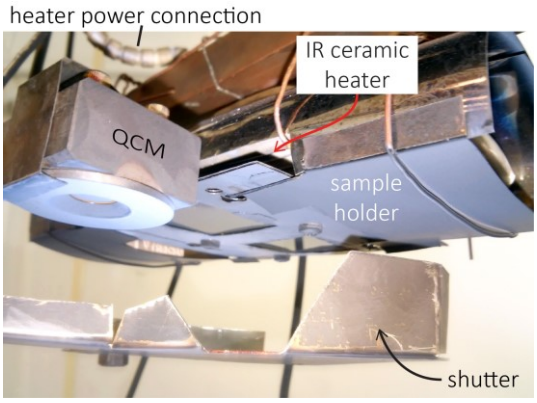

Fig. 3.11: The improved substrate heater.

3. **Sn source test**. As already said, the sources and their power supply were designed for the co-evaporation of Cu, Zn, Sn and S, but they were not sufficient for their purpose. During the tests on Sn evaporation, we experienced frequent shortcuts and discharges (see Fig. 3.12-a and Fig. 3.12-b).

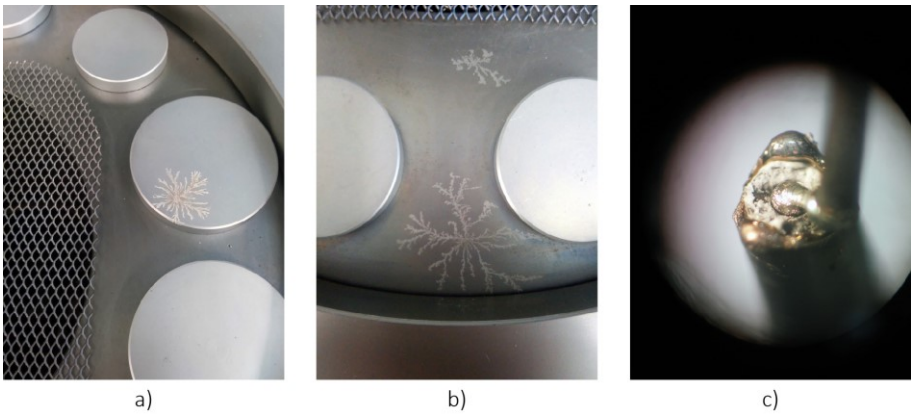

Fig. 3.12: a) and b) Arc discharge evidences on steel; c) the damage on the hot end of a resistive wire caused by a too high current flowing on it.

One current failure was so dramatic that one power board resulted burned to the point that was irreparably broken and thus required its substitution. Moreover,

due to the geometry of the instrument unit (the sources electrical connections are inaccessible, as they are below the steel plate sources holder of Fig. 3.8), when these shortcuts happened and thus the source power supply circuit resulted "opened", we were forced to disassemble the vacuum system, moving away the heavy and bulky instrument unit. These operations are very time consuming and required the help of at least 3 people.

There were two main issues causing the shortcuts: 1) the heating elements was not enough powerful to heat up the source – the resistive wire was simply too short – and 2) the source was not adequately thermally isolated – the enormous thermal loss requires a surplus of energy to keep the source temperature constant. These two issues were the reasons why we were forced to work beyond the apparatus limits: the power module had to supply more power than its design to, and the current needed by the source was too high, causing the degradation of the electric connections of the resistive wire end (an example of the damage caused to the thermocoax end is depicted in Fig. 3.12-c)).

At the beginning, the current failures were charged to bad electric connection between the supply elements and the thermocoax hot ends. To fix this problem, some modifications were applied:

a. We improved the thermal isolation of the sources by covering its top and bottom surfaces with a molybdenum foil. Before this solution, in fact, only the lateral surface was isolated. An improvement of the performance was recorded but it was not enough, hence we designed and built a new source.
b. The new source was constituted by the old graphite crucible and the old resistive wire (with a resistance of R = 3.7 Ω) located on the crucible lateral surface was substituted with a longer one exhibiting a resistance of 9.1 Ω. Moreover, a second molybdenum foil was added on the lateral surface of the crucible to further improve its thermal resistance.
c. We used some ceramic terminal blocks for the connections among the feedthroughs and the cold conductors (copper wires). The cold conductors were isolated with an insulating sheath. We used Be-Cu inline barrel connection (from K.J. Lesker Company) for connecting the cold and the hot ends (thermocoax). Ceramic insulating beads were used to avoid arc discharges between the conducting wire and the thermocoax metallic sheath.

d. The broken power board was substituted with a new one (Tecnel VM570 type 620), able to provide more power (a repetitive peak current of 16 A instead of 8 A).
e. We connected an amperemeter in series to each source power supply circuit, to monitor the current provided to each source.

These modifications also helped to maintain the whole vacuum chamber colder.

The described actions considerably improved vacuum quality, from $1 \cdot 10^{-4}$ mbar to $5 \cdot 10^{-6}$ mbar. The source dedicated to Sn deposition now can reach a maximum temperature above 1100 °C, instead of the former 700 °C. However, all these improvements were not enough to evaporate Sn thin films. In fact, we reached a maximum evaporation rate of 0.02 nm/s (QCM span measurement limit) with the source draining almost 300 W, heated up to a temperature of 1080 °C, at a pressure of $4 \cdot 10^{-5}$ mbar with the source in crucible configuration – i.e. without the Knudsen top part.

Since the experimental apparatus cannot evaporate Sn, the co-evaporation of Sn and S as a possible way to deposit SnS thin films was no more considered.

The possible alternative to the co-evaporation is the evaporation of the SnS compound. Hence, the modified apparatus was used to verify the possibility of SnS evaporation from its compound. As said, the 99.99 % pure SnS compound lumps have been bought from Huizhou Tian Yi Rare Material Co., Ltd. The temperature needed for SnS evaporation is lower than the tin one, therefore, a non-improved source was initially used. We succeeded in evaporating SnS with an evaporation rate of 1 nm/s under the following conditions: source draining 150 W, source temperature 760 °C, chamber pressure $1 \cdot 10^{-5}$ mbar.

However, the power module used for supplying the original sources was still working close to its upper limits also for SnS evaporation. Frequent power faults affected the deposition apparatus during evaporation processes. We decided to use the most powerful power module in combination with the improved source. For doing that, the improved source has been emptied from the molten Sn, and then has been cleaned by using isopropanol; the solvent was removed before its evaporation by using the Ar pressurized gun. The source was then reassembled into the instrument unit, and the instrument unit in the apparatus; the vacuum was made and the cleaning procedure was completed by heating up the source at the maximum temperature, to remove eventual residues.

The electrical stability was considerably improved, the shortcuts occurred rarely compared to the previous case and therefore, also the maintenance of the apparatus required less efforts.

We found that the remaining current faults were due to a problem related to the SnS deposition. During the evaporation, the material is deposited all over the chamber, not only on the substrate. SnS residues were found even under the source holder steel plate. This material, due to the high temperature reached there during deposition, have the chance to re-evaporate, forming a SnS thin film in the electrical connection area. While soon after the electrical connection restoration, the resistance between the conductor wires and the ground of the apparatus was of hundreds of MΩ. after some deposition processes without any maintenance, this SnS thin film deposited everywhere reduced the resistance to few kΩ, thus virtually grounding all the conductor wires. This effect was even more evident after a high number of evaporation processes without maintenance, to the point that maintenance is needed to perform standard operation with the machine. At that point, in fact, it was not possible to supply to the sources the current needed for achieving the SnS evaporation temperature.

A long-term evaluation of the apparatus behavior equipped with improvement discussed in this chapter leads us to some further improvements. In fact, it was necessary to improve the stability of the machine by working far from its operation limits and to simplify the maintenance operation making it a simpler and less frequent task.

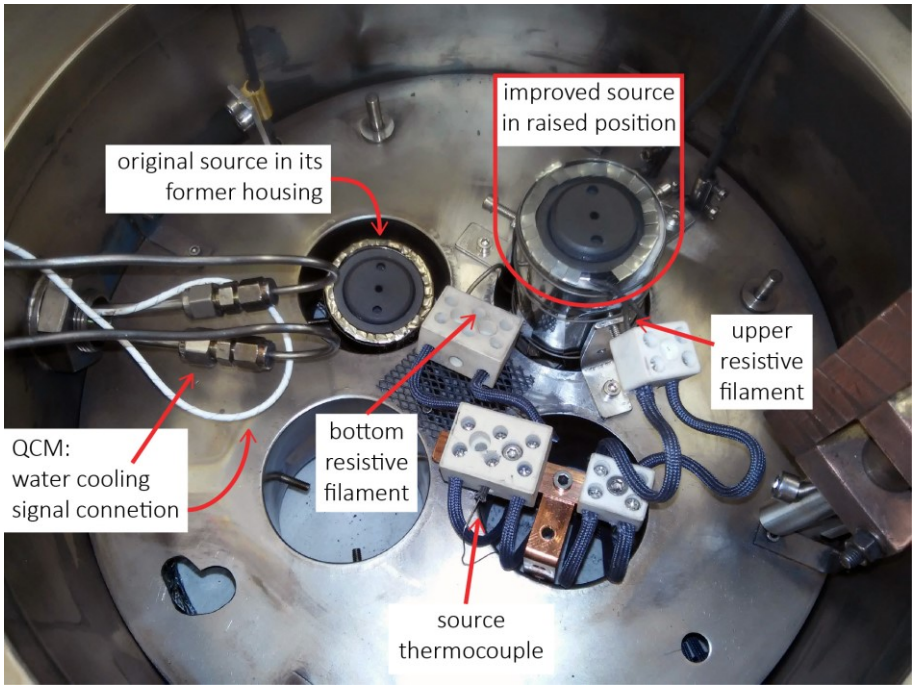

Fig. 3.13: The instrument unit at the end of the last improvement stage. It is possible to see the renewed Knudsen cell in its new raised position as well as the electrical connection finally available from above, as well as a non-upgraded source in the original source holder position.

The following improvements (refer to Fig. 3.13) were finally applied.

1. To remove SnS residues from the previous deposition processes, the cleaning of the deposition chamber was firstly carried out. The bell and the instrument unit were mechanically cleaned with isopropyl alcohol; once the apparatus was reassembled, it was heated in vacuum with the cooling system isolated to re-evaporate adsorbed materials from the machine walls.
2. We built an evolution of the substrate heater (see Fig. 3.14), constituted by a single molybdenum foil carved, to guarantee a better stability of samples. Four samples can be deposited at a time.

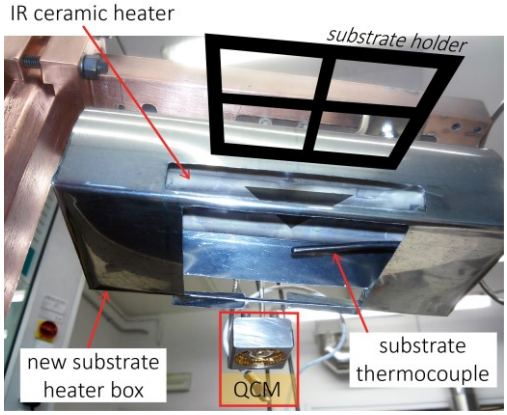

Fig. 3.14: The substrate holder/heater in its final version.

3. Two different shutters were used for controlling samples and QCM exposure to evaporant.
4. The sources and its electrical connections maintenance procedures were simplified by moving the SnS Knudsen cell and its connections over the steel plate (the former source holder), to permit an easy access to them. This required the building of a new housing for the source and its power connections. In this configuration, it is no longer needed to remove the heavy instrument unit from its place for maintenance. Moreover, the former source housing was water cooled, hence now the dissipated power is reduced, allowing to decrease the source draining power. This required the removal of all the source shutters.
5. The SnS source was rebuilt: no new thermocoax was available, so two old wires were recovered to heat it up. The 9.1 Ω resistance thermocoax now heats only the lateral surface of the graphite crucible, whereas the 3.7 Ω resistance thermocoax heats the crucible base only. Moreover, the two thermocoax were supplied by to different power modules, the old one for the 3.7 Ω resistance thermocoax, the new one for the higher resistive thermocoax. In this way, the same temperature requires a lower power supplied to the source. Furthermore, the source received an improved thermal insulation by alternating two quartz wool and two molybdenum layers. This combination allows to choose the source area to be heated, to reduce the power furnished by the single power module obtaining a higher total power with respect to the previous configuration. For instance, the source can reach a temperature of 800 °C by draining only 130 W (80 W from the base circuit, 50 W from the lateral circuit).
6. The ceramic terminal blocks are now enclosed into a tin foil layer to protect them from the SnS residues during its deposition, and thus furtherly reducing the shortcut probability.
7. Finally, we prepared a sort of small chamber inside the main chamber constituted by a molybdenum cone covered by tin foil which surrounds the evaporant path. The tin foil walls have to collect the SnS material which will not condense to the sample, before it reaches the main chamber walls. The tin foil can thus be substituted as often as possible to limit the SnS chamber self-contamination. A roof tin foil located over the sample holder completes the small chamber.

These last improvements made the apparatus even more stable, and, above all, sample reproducibility has improved. No maintenance procedures have been performed since this last machine upgrades were applied. Some power failures have still been encountered, but their frequency has been reduced significantly, and their effects on the machine behavior are negligible. Nevertheless, the improvements to the sample holder allow us to produce a doubled number of sample for deposition process, which widen the possibilities of sample post deposition treatments studies.

The apparatus evolution followed the research necessities. All the changes described so far improved the deposition machine.

Chapter 4.

CdS/SnS THIN FILM SOLAR CELLS

As described in Chapter 2, the CdS/SnS heterojunction investigated in this work is deposited by thermal evaporation on the front contact in superstrate configuration. In this chapter, the SnS based solar cell which exhibited the best performance will be presented and its properties discussed. Then, we will focus our attention on the limited performance reproducibility that affected our samples, hypothesizing that this behaviour could be correlated with the thermal history of the SnS raw material. Finally, we will present a systematic study of the influence of both the substrate temperature (T_{sub}) and the SnS raw material thermal history on the properties of the SnS solar cells and their performance.

Part of this work has been presented and published in the PVSEC 2015 conference proceeding[59]. Section 4.3 was presented in a poster at EMRS 2016 Spring Meeting.

4.1 Our best performing device

The best performing device produced as described in Section 2.1, will be presented in the next pages. The 2 µm SnS absorber layer have been deposited over the glass/ITO/ZnO/CdS stack at a substrate temperature of 250 °C, and setting an evaporation

rate of 0.5 nm/s. After this step, the device was moved to the back contact deposition machine and soon after completed by depositing 50 nm of Au over the absorber layer.

In Fig. 4.1 the J-V characteristic of the sample is shown.

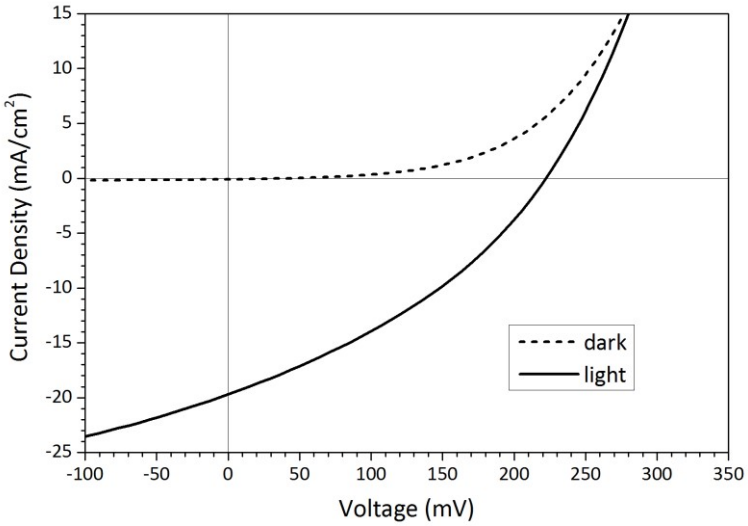

Fig. 4.1: J-V characteristic of the best produced device under dark (dashed line), and under light (black line). The sample stack is glass/ITO/ZnO/CdS/SnS/Au.

The sample exhibits a power conversion efficiency $\eta = 1.51$ %, a fill factor F.F. = 34.0 %, an open circuit voltage $V_{OC} = 226$ mV and a short circuit current density $J_{SC} = -19.6$ mA/cm^2. The parallel resistance is $R_P = 21.3$ Ω·cm^2 and the series resistance is $R_S = 5.0$ Ω·cm^2. All the eight solar devices of the sample showed a similar behaviour; J_{SC} and R_S are the parameters which mostly deviates from their average values.

Our result is comparable with those published by Schneikart *et al.*[31], the best CdS/SnS heterojunction based solar cell produced in superstrate configuration and with the same deposition technique. However, that device has an active cell area of 0.01 cm^2 whereas ours has a 0.13 cm^2 area. This means that the uniformity of our film has been demonstrated for a wider area.

The cell parameters are summarized in Table 4.1.

Table 4.1: Best glass/ITO/ZnO/CdS/SnS/Au cell performance parameters compared to those of Schneikart et al.[31] (ref. [31]).

	A [cm²]	η [%]	F.F. [%]	V_{OC} [mV]	J_{SC} [mA/cm²]	R_P [Ω·cm²]	R_S [Ω·cm²]
best cell	0.13	1.51	34.0	226	-19.6	21	5
average	0.13	1.23 ± 0.22	32.8 ± 1.2	227 ± 2	-16.4 ± 2.6	24 ± 2	7 ± 2
ref. [31]	0.01	1.42 ± 0.14	38.0 ± 0.9	208 ± 7	-17.9 ± 0.3	31 ± 4	5 ± 1

It is known that all photovoltaic technologies modify their performance during illumination. In particular, in the thin film polycrystalline photovoltaic case, it has been

reported[60] a non-negligible performance improvement due to light exposure. The authors ascribed this behaviour to the presence of trap states in the middle of the gap in the junction region which populates during light exposure thus being deactivated as recombination centres. Another work[61] reports an initial improvement of the performance, but followed by a long-term degradation due to the same process.

To investigate the effects of light soaking on the performance of the device, the last has been exposed to continuous light for ten minutes and, at the same time, cooled with a fan to maintain constant its temperature. The effects of light soaking on the solar cell electrical behaviour are shown in Fig. 4.2, while the parameter variation is reported in Table 4.2.

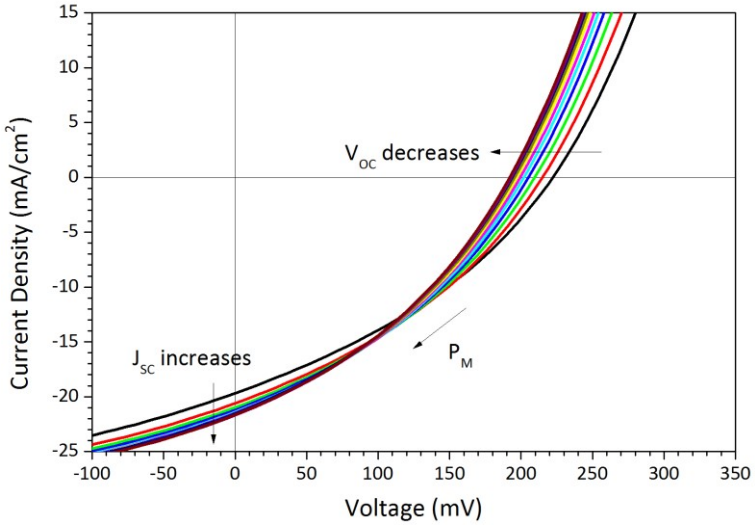

Fig. 4.2: The current density-voltage characteristic variation due to light soaking effect.

The solar cell responded to the light stimulation.

During the first half of exposure time, the performance resulted improved: after the first minute, the biggest performance improvement was recorded, after which efficiency decreased monotonically. After five minutes of exposure, the performance was comparable with its starting value. During this period, the fill factor increased to its maximum value as well as J_{SC}, whereas V_{OC} decreased almost linearly. After ten minutes, no further J_{SC} increment or V_{OC} decrement was recorded.

The behaviour can be summarized as follows. Firstly, the efficiency resulted increased, but soon after it decreased linearly. Fill factor exhibited a similar behaviour, but its maximum values has been reached in the mid of the experiment. V_{OC} and J_{SC} shown

a compensatory effect: while V_{OC} decreased during the whole experiment, J_{SC} had grown, but both reached saturation between six and seven minute of exposure.

Table 4.2: The solar cell parameter variation due to light soaking and due to storage in dark during following year.

		η [%]	F.F. [%]	V_{OC} [mV]	J_{SC} [mA/cm²]	R_P [Ω·cm²]	R_S [Ω·cm²]
light soaking	0 mins	1.51	34.0	226	-19.6	21	5
	1 min	1.56	34.5	219	-20.6	21	5
	2 mins	1.55	34.9	212	-20.9	21	5
	3 mins	1.54	34.2	212	-21.2	20	4
	4 mins	1.52	34.9	205	-21.3	20	4
	5 mins	1.51	34.5	205	-21.4	20	4
	6 mins	1.50	35.3	198	-21.5	20	4
	7 mins	1.50	35.0	198	-21.6	20	4
	8 mins	1.48	34.7	198	-21.5	19	4
	9 mins	1.48	34.6	198	-21.6	19	4
	10 mins	1.47	34.3	198	-21.6	19	4
stored in dark	1 day	1.21	30.6	226	-17.5	20	8
	1 month	1.05	29.8	226	-15.6	20	10
	4 months	0.95	29.3	226	-14.4	21	11
	1 year	0.88	28.5	233	-13.2	23	13

The device was then stored in dark in our sample “closet”, and measured at time intervals (months scale).

In Fig. 4.3 the device performance during time is shown, while the J-V parameters are reported in Table 4.2. It is possible to see an overall degradation of the device performance. A non-negligible performance loss is recorded the day after the light soaking experiment: we can very likely correlate these two things. While V_{OC} recovered to its initial value, J_{SC} did not, while R_P and R_S moved far from their starting values and from ideality. The rectifying power of the device seemed to be the worst loss, F.F. reduced strongly and the J-V characteristic flattened. This behaviour continued slowly during the following year.

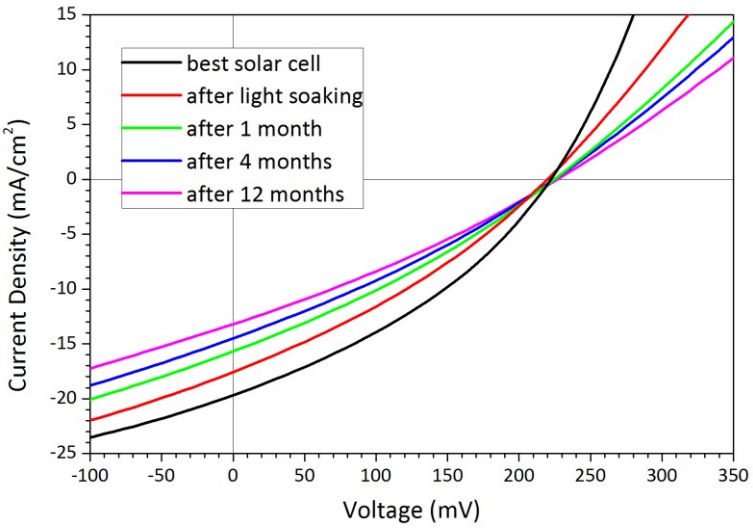

Fig. 4.3: The J-V characteristic of the device along time.

4.1.1 SnS layer characterization

In Fig. 4.4 the SnS layer morphology is shown. The AFM image shows the coexistence of grains with various sizes, from hundreds of nm to above one µm in diameter. Furthermore, the morphology shows SnS lamellar structure.

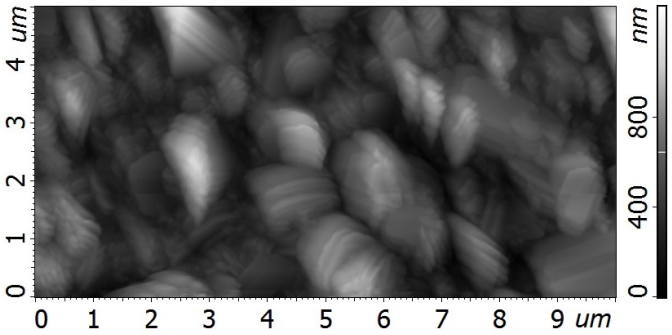

Fig. 4.4: The morphology of the sample as recorded by AFM.

By continuing the comparison with the work of Schneikart *et al.*[31], the morphology shown here is slightly different from what they have published, even if the substrate temperature T_{sub} value during SnS deposition is nominally the same. They describe their sample morphology (not shown) as constituted by rectangular grains with an average grain size of 0.9 µm[31]. In our case, it is possible to find a more uniform grain size distribution, and the grain shape is far from being rectangular.

Moreover, in that work[31] and in the one of Kawano *et al.*[33], it has been highlighted that over a T_{sub} value of 250 °C it is not possible to deposit any SnS film, due to its re-evaporation: we obtained the same at T_{sub} = 420 °C. By roughly rescaling our

temperature range to their ones, our sample would grow at a substrate temperature of 150 °C, and thus turn to agree with Schneikart and Kawano observations. We ascribe to this different range of temperature the different morphology. It is important to stress that the different temperature scale can be due to different and not well-controlled factors, ranging from the thermocouples calibration to their actual position in the deposition chamber.

The effect of T_{sub} on SnS morphology will be further discussed in Section 4.3.

Finally, in Fig. 4.5 the microcrystalline structure of the sample is shown. The x-ray diffraction pattern confirms that our absorber layer is a polycrystalline material. Moreover, by comparison with JCPDS card 39-0354, it resulted to be SnS in its orthorhombic phase. In Fig. 4.5 only the main reflection planes are indicated. Only two peaks do not belong to SnS: the peak at 2θ = 35.5 ° can be attributed to the ITO layer, whereas the one at 2θ = 38.2 ° is the (111) reflection of Au, i.e. the back contact. The comparison with the XRD data presented by Schneikart *et al.*[31] requires again to keep in mind the different substrate temperature at which the samples were deposited. The two diffraction patterns are very similar, in fact, both exhibit the main diffraction peaks of orthorhombic SnS. The different relative intensity of diffraction peaks is most probably due to the different temperature ranges of the two apparatus. In the diffraction pattern recorded by Schneikart *et al.*[31], the main peak at 2θ ≈ 34.3 ° is due to the front contact layer.

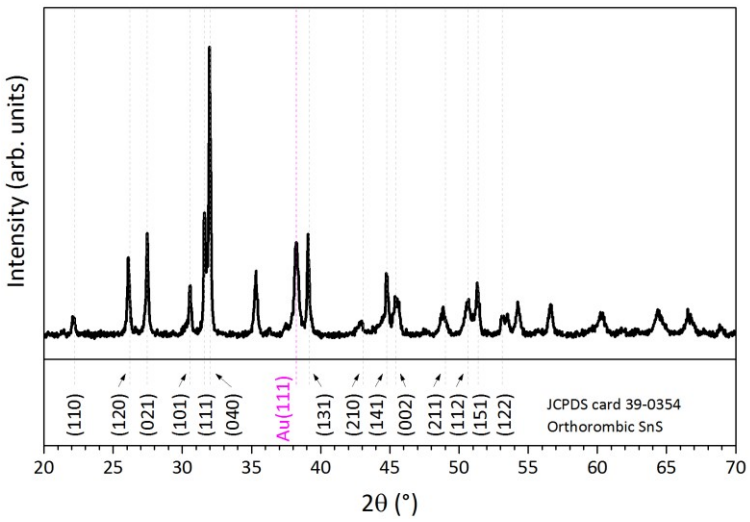

Fig. 4.5: The XRD pattern of our sample.

4.2 Performance irreproducibility

In this section, we will discuss the irreproducibility that we observed about the performance of our devices. Four samples (A, B, C, D) will be discussed. Although these four samples were deposited on the same substrate stack (glass/ITO/ZnO/CdS), with the same thickness (≈ 2 µm), at the same substrate temperature (T_{sub} = 250 °C), and evaporation rate (Γ = 0.5 nm/s), their performance is rather different. The J-V characteristics of Fig. 4.6 show at a different behaviour of the four samples.

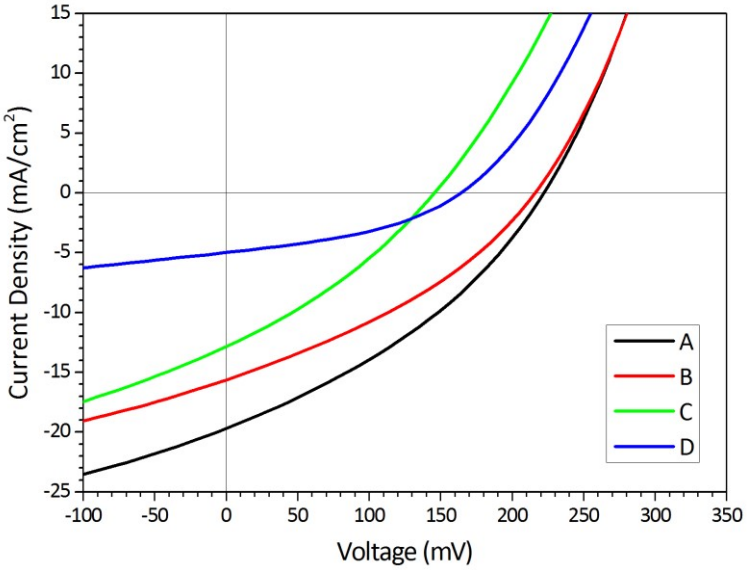

Fig. 4.6: J-V characteristic of four samples. Even if the samples were deposited with the same deposition parameters, their electrical performance varies.

The device working parameters are summarized in Table 4.3. The efficiency strongly varies from one sample to one another, ranging from η = 0.32 % to η = 1.51 %.

It is possible that the different performance, i.e. something which seems not correct to call *sample irreproducibility*, could be attributable to another parameter which we have not initially considered: the "thermal history" of the SnS material inside the Knudsen cell. In Table 4.3 an explicative example of the possible impact of this effect is shown: before the deposition of sample C, raw SnS had never been heated; in the case of samples A and B, those exhibiting the best performance, but deposited during different processes, the material was heated up once before the sample depositions; finally, for sample D, the raw material was heated up twice before its deposition.

Table 4.3: The working parameters of the four solar cells depicted in Fig. 4.5.

	η [%]	F.F. [%]	V_{OC} [mV]	J_{SC} [mA/cm²]	R_P [Ω·cm²]	R_S [Ω·cm²]
A	1.51	34.0	226	-19.6	21	5
B	1.16	33.8	219	-15.6	25	6
C	0.59	30.8	149	-12.8	18	7
D	0.32	38.2	170	-5.0	75	11

To study this phenomenon, we decided to fill the SnS crucible with a large amount of SnS (40 g), enough to allow a wide number of following depositions. In order to maintain the comparability between different processes, we decided to deposit samples keeping constant the substrate temperature, the evaporation rate and the absorber layer thickness (2 µm).

In Fig. 4.7, the efficiency of the samples produced in this way is plotted as a function of the number of heating/cooling processes experienced by the raw material. The error bars in the figure represent the standard deviation from the average efficiency of the eight solar devices constituting the same sample.

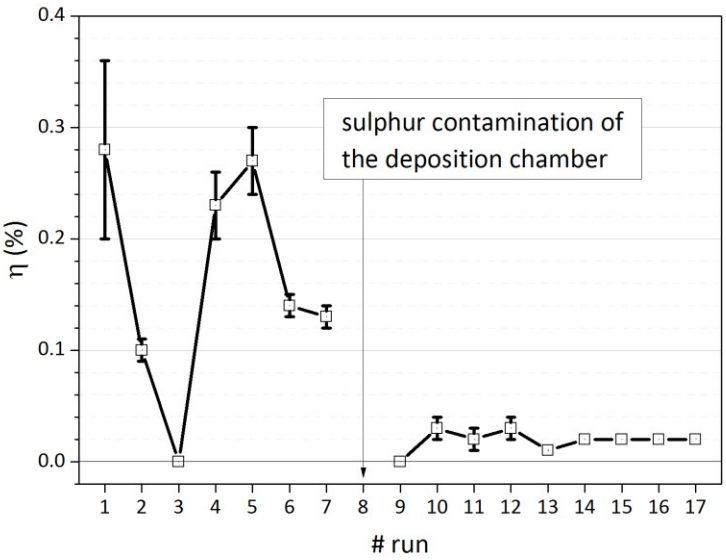

Fig. 4.7: The efficiency of identical samples produced with subsequent processes from the same raw material.

A clear trend is not visible; a very high variability affects the device performance. However, a general worsening of the performance can be seen before the eighth run.

The eighth run changed the apparatus behaviour for a very long time. As it can be seen, after that process, the sample efficiency collapsed and remained very close to zero. The cause of that behaviour can be imputed to an experiment carried out in parallel with the main one, during which elemental sulphur was evaporated in the chamber: the

sulphur contamination of the deposition apparatus is most likely linked to that, even if the apparatus is used to evaporate a sulphur compound.

To solve the problem, which persisted for a long time, we decided to manually clean the deposition chamber. This procedure brought us to the final cycle of improvement actions made on the deposition apparatus, as described in Section 3.2.

We applied two different types of thermal treatment on raw SnS before its deposition. The first treatment was an annealing in vacuum of the SnS lumps in the Knudsen cell at 550 °C for 30 minutes, whereas the second treatment was the annealing of the material inside a quartz tube furnace in controlled atmosphere – Ar at a pressure of 500 mbar – at 500 °C for 60 minutes. A similar thermal treatment of the raw material has been proposed by Steinmann *et al.*[32] to clean the SnS powders from impurity phases.

In Fig. 4.8 the efficiency (normalized to 100 % of the first device) of the solar devices produced from the treated SnS is shown alongside the first four devices produced in the previous case with no treatment of the raw material.

In this case a trend can be seen: the treating of the SnS raw material seems to cause a non-negligible improvement of the performance of the devices produced during the second process compared to those produced within the first process. After that, in both the third and the fourth processes the performance decreases below the previous cases.

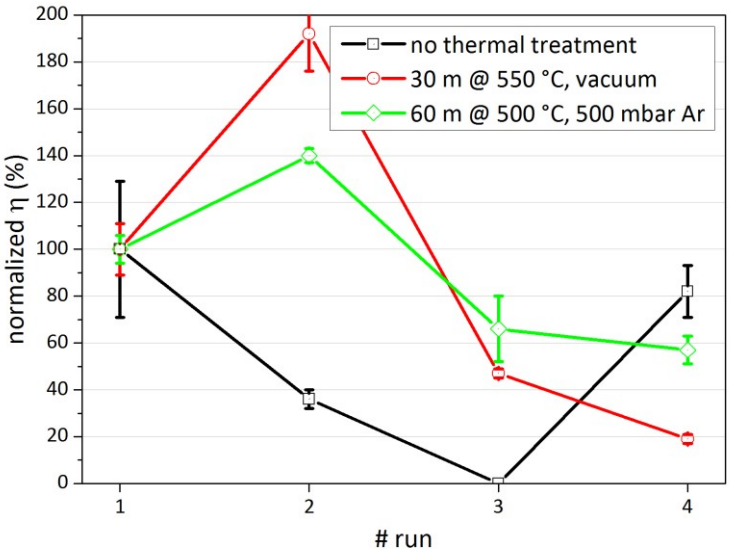

Fig. 4.8: The normalized efficiency normalized of the solar devices produced from the SnS raw material: untreated (black), annealed in vacuum (red), and annealed in Ar (green).

4.2.1 Analyses of the SnS raw material

To identify any reason for the problem described in the previous section, the raw material was studied by using XRD, Raman and EDX spectroscopy.

4.2.1.1 X-ray diffraction

The XRD analysis was carried out on three different samples, see Fig. 4.9. Firstly, the batch material sold by Huizhou Tianyi Rare Material Co., Ltd. – from now on TRM – with no modification was analysed. We decided to analyse also the raw material after its 60 minutes annealing in the furnace at 500 °C; the part of treated SnS we did not use for the analysis was used to fabricate the devices, for which the normalized efficiency trend is shown in Fig. 4.8. The final diffraction pattern of Fig. 4.9 was recorded from the material recovered from the SnS Knudsen cell after two heating/cooling cycles – i.e. two deposition processes. All the samples have been pulverized before recording their diffraction pattern.

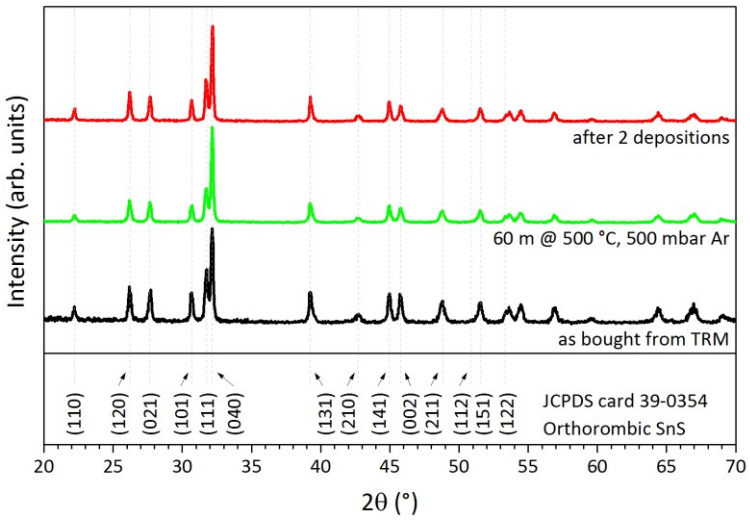

Fig. 4.9: The XRD patterns of the SnS raw material, as bought from TRM (black), treated in quartz tube furnace for 60 minutes at 500 °C at a pressure of 500 mbar of Ar (green) and the material after two deposition processes (red).

In all the three cases, XRD confirmed that the analysed material was orthorhombic SnS. The only variation among the patterns is the change of the relative intensities of the diffraction peaks: especially in the latter case, it could be explained by the double phase transition that the material experienced: the double cycle of sublimation and condensation subdue by SnS.

We have also taken in consideration ≥ 99.99 % pure SnS powders from Sigma-Aldrich Co. LLC. (SA) (product 741000-5G) to confirm the observed phenomenon. In Fig. 4.10, the

XRD spectra of the raw material is depicted alongside with the XRD pattern of material recovered from the SnS Knudsen cell after two deposition processes.

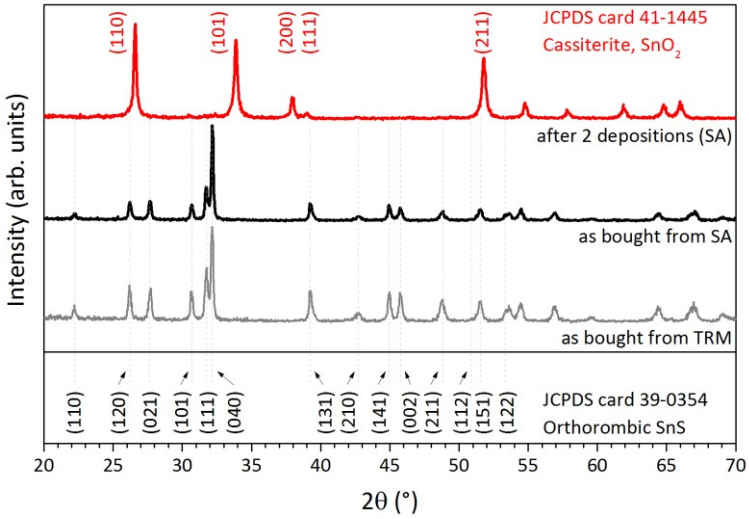

Fig. 4.10: The XRD patterns of the SnS raw material, as bought from TRM (grey), as bought from SA (black) and after two deposition processes (red).

The XRD pattern of the SnS bought from SA is very similar to the case of the TRM SnS. However, it is rather evident that the SA material suffered a strong modification: from the analysis of the XRD pattern resulted that the SnS residues in the Knudsen cell was actually pure SnO_2.

Probably the different form of the two SnS supplies – lumps for the TRM case against powders for the SA one – would cause the different behaviour.

Schneikart in her PhD thesis[62] studied SnS provided by several suppliers in form of powders (abcr gmbH Co. KG, Alfa Aesar, American Elements), and reported a strong pressure variation during heating of source material and the formation of SnS_2 film instead of SnS before the raw material stabilizes. She demonstrated that the sulphur excess in her samples was due to the presence of SnS_2 and SnO_2 in the powders of the batch material. Also in our case, we experienced a comparable pressure variation. Although the same SA material has been successfully used by Steinmann et al.[32] in producing the thermal evaporated record efficient solar device (η = 3.88 %), we avoided any further use of SA powder SnS preferring the more stable SnS lumps.

As many authors[18,37] reported that XRD measurement was not able to reveal the presence of SnS_2 or Sn_2S_3 due to the overlapping of the main diffraction peaks of the different phases, we tested our samples with other techniques – Raman and EDX spectroscopy – to verify the presence of different stoichiometric phases.

4.2.1.2 Raman spectroscopy

Micro-Raman spectroscopy is a very punctual technique (the illuminated area of the sample is in the order of few μm^2), therefor the measurement was repeated many times on different areas of the sample with the aim of having a more representative vision of the sample. In Fig. 4.11, Fig. 4.12 and Fig. 4.13 only the more representative spectra are shown.

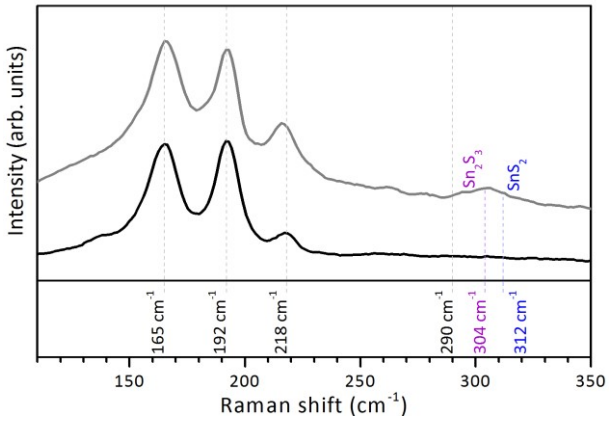

Fig. 4.11: Raman spectra of the SnS raw material, as bought from TRM. The two measurements were carried out on the same sample in different areas.

In the first case, the SnS raw material as bought from TRM (Fig. 4.11), the µRaman measurements showed the main Raman peaks of SnS at Raman energy shifts of 165, 192, 218 and 290 cm^{-1}. The relative intensity of the Raman peaks slightly changes from point to point. The presence of the Raman peaks strongly depends on the incident and scattered light direction of polarization[63]. In our case, the simultaneous presence of all the Raman peaks is due to the absence of any polarizing filter in the experimental setup. Moreover, we report in some measurements the presence of two peaks at 304 cm^{-1} and at 312 cm^{-1} which are ascribed respectively to the Sn_2S_3 and SnS_2 phases[37].

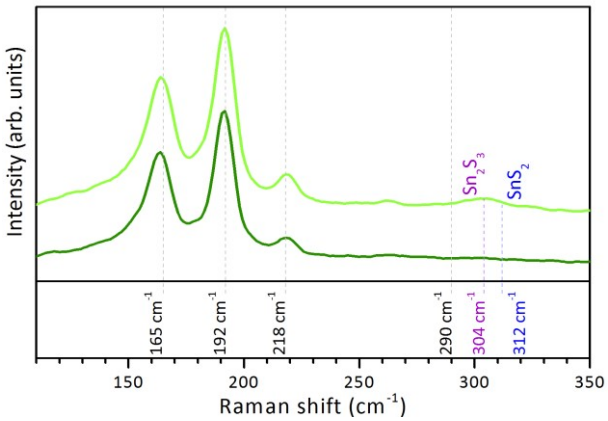

Fig. 4.12: Raman spectra of the SnS raw material from TRM, treated in the quartz tube furnace for 60 minutes at 500 °C at a pressure of 500 mbar of Ar. The two measurements were carried out on the same sample in different areas.

A similar result was obtained for the SnS material after being treated in the quartz tube furnace at 500 °C (Fig. 4.12): the main SnS peaks are always present and the only variation is related to the relative intensity of the peaks. The peak at 192 cm^{-1} is always more intense than the 165 cm^{-1} one; this was not true in the non-treated case seen above. This can be due to the presence of a preferential orientation of the sample crystals, different from the previous case. Finally, also in this case we report that some spectra exhibited the presence of the Sn_2S_3 and/or SnS_2 phases.

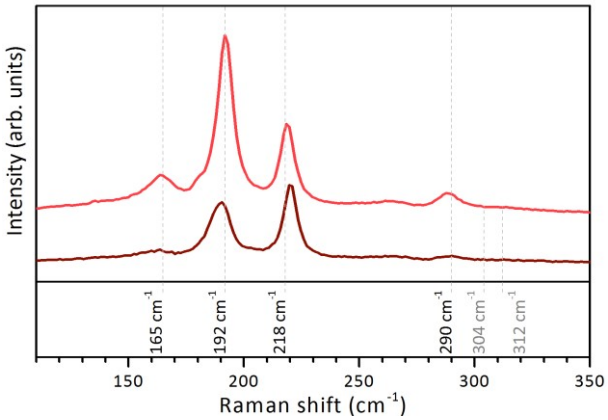

Fig. 4.13: Raman spectra of the SnS raw material from TRM, after two deposition processes. The two measurements were carried out on the same sample in different areas.

In Fig. 4.13 a representative of the Raman spectra of the samples which underwent the double cycle of sublimation and condensation in the Knudsen cell, is shown. Again, all the SnS Raman peaks are present indicating SnS as the main phase present in the sample. A different relative intensity of the peaks appeared: in all the measurements, the peak at 165 cm^{-1} is weaker compared to the previous cases, whereas the peak at 218 cm^{-1} is now

more intense, and in one case the most intense. Moreover, there is no signal in the region over 300 cm^{-1} indicating the absence of impurity phases. It seems that the sublimation/condensation cycles have purified the SnS from phase impurities.

4.2.1.3 EDX Spectroscopy

In Fig. 4.14 the surface of the samples is shown. By comparing Fig. 4.14-a and Fig. 4.14-b, the as-bought raw material and those treated in the quartz tube furnace at 500 °C, it is possible to say that the treatment seems to have cleaned the sample from its own powder, which is present in the picture on the left side. In Fig. 4.14-c the double phase transition effect is depicted: it shows a completely different morphology, which is compatible with SnS sublimation and condensation on a different surface (the top part of the Knudsen cell). This structure is similar to the one of the evaporated SnS when a thin film is deposited at the maximum substrate temperature value before its re-evaporation, as it will be discussed in Section 4.3.

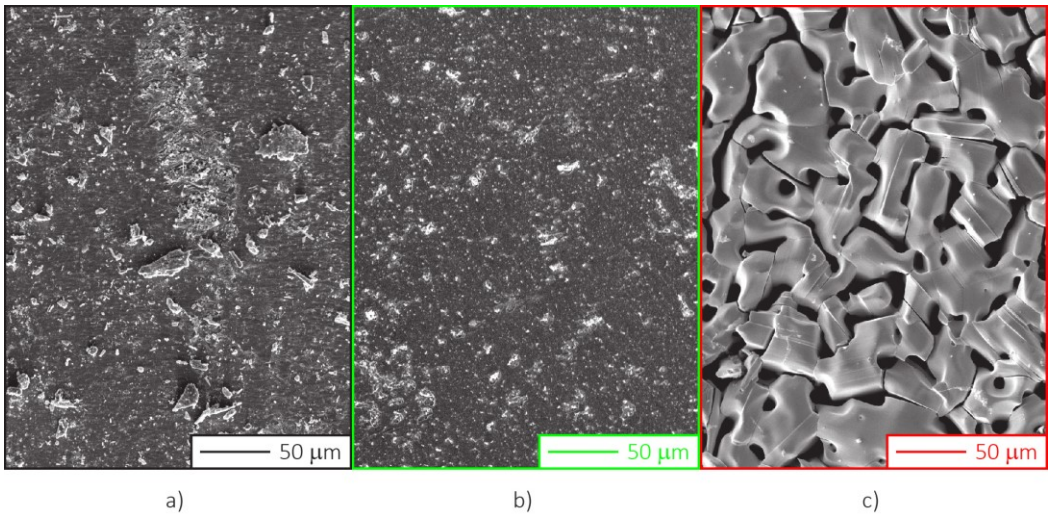

Fig. 4.14: SEM scans of the surface of a piece of the a) as-bought SnS, b) the raw material after its thermal treatment at 500 °C, and c) the raw material after two sublimation/condensation cycles.

From the EDX measurements performed on these samples, we obtained a result which confirms the Raman analyses. In Table 4.4 the calculated Sn/S ratio is summarized. The Sn/S ratio of the "as-bought" material is about 1.09. This indicates a sulphur excess in the studied material, which is compatible with the presence of the phase impurities highlighted by some of the Raman spectra. The absence of the Sn_2S_3 and SnS_2 peaks in some of the Raman spectra can be explained by the fact that the impurity phases would be spread in localized areas of the sample. By applying the thermal annealing to the raw SnS, a slight decrease of the Sn/S ratio to 1.08 appeared. This could be due to the

disappearance of the SnS powder as observed in Fig. 4.14-b, which again leads us to think that the small particulate can be responsible for a part of the sulphur excess. Finally, the Sn/S ratio in the case of the material taken from the Knudsen cell, which experienced the sublimation/condensation double cycle, exhibited a value close to unity; this is in agreement with the absence of the Sn_2S_3 and SnS_2 peaks in Raman spectra.

Table 4.4: The S/Sn ratio calculated from EDX measurement.

	Sn/S ratio
As bought from TRM	1.09
60 m @ 500 °C, 500 mbar	1.08
After 2 deposition	1.01

Therefore, we can stress that the SnS raw material phase purity is a key factor in SnS deposition.

It seems that the operation required to deposit SnS thin films on the substrates will correct the raw material poor stoichiometry, since the sublimation and the condensation of the material always happen during a deposition process. This could explain the different performance of SnS solar devices due to the thermal history of the raw material, but it leads to hypothesize that once the raw material is purified from other phases, the solar devices should show a better performance; however, as seen in Fig. 4.7, it is not necessarily true. Most likely, other phenomena were mainly influencing our devices. For example, the sulphur contamination of the deposition chamber might have killed the efficiency of many devices during many runs.

Moreover, this is consistent with what has been seen by Schneikart[62], i.e. after some deposition processes during which there was SnS_2 deposition instead of SnS, at a certain point, they were able to deposit SnS, probably when the sulphur excess in the raw material ended. They also reported the formation of a thin (1 nm-thick) layer of SnS_2 on CdS layer.

A different probe would help in the identification of different phases on the sample in the bulk region, especially close to the junction and not only on the surface region.

4.3 Influence of T_{sub} and raw SnS material on SnS solar cells

In this section the correlation between sample performance and the thermal history of the raw material, as well as the dependence on the substrate temperature, will be investigated.

The samples described here were deposited soon after the last phase of improvements applied to the evaporation machine and, more important, after the cleaning of the chamber which has been discussed in the last part of Section 3.2.

We decided to fill the crucible with ≈ 2 g of raw SnS: this amount of material is enough for depositing two different runs of samples. The raw SnS did not undergo any thermal treatment. Once the two processes were completed, the crucible was emptied and refilled again, and the tin foil forming the small deposition chamber (inside the main chamber, see Section 3.2) was changed to remove any contaminant. In every process a 2 µm SnS thin film layer was prepared, whereas the substrate temperature was varied: the 210-390 °C T_{sub} range was studied, with 60 °C step.

We decided to take these precautions to avoid any possible contamination which could affect the results of the experiment.

The morphology of the samples was characterized by AFM, the crystalline structure by XRD, the film phase purity by Raman spectroscopy. The device performance was finally measured and reported.

A study of the SnS solar devices on the T_{sub} parameter has been already published by Schneikart[62] and Kawano *et al.*[33] thus the results will be compared where necessary. Both Schneikart and Kawano studied SnS solar cells deposited by thermal evaporation with the CdS/SnS heterojunction. The complete device stacks are similar: glass/ZnO:Al_2O_3/ZnO/CdS/SnS/Au – for Schneikart, in our case ITO replaced ZnO:Al_2O_3 as front contact – and glass/Mo/SnS/CdS/ZnO/ZnO:Al_2O_3/Al – for Kawano. The main difference is that Schneikart adopted the superstrate configuration whereas Kawano has chosen the substrate configuration. This means that in our case and in the Schneikart one, the CdS/SnS heterojunction is formed during SnS deposition, whereas in the Kawano case, the junction is formed during CdS deposition, which for them is a step that follows SnS deposition. It is worth noting that the best SnS solar cells device reporting an efficiency over η > 2 % were deposited in substrate configuration[16,32,33,37], however it is also true that this configuration has been more widely studied than the other one.

4.3.1.1 AFM analysis

The morphology of SnS samples is shown in Fig. 4.15. The T_{sub} parameter variations resulted in very different morphologies.

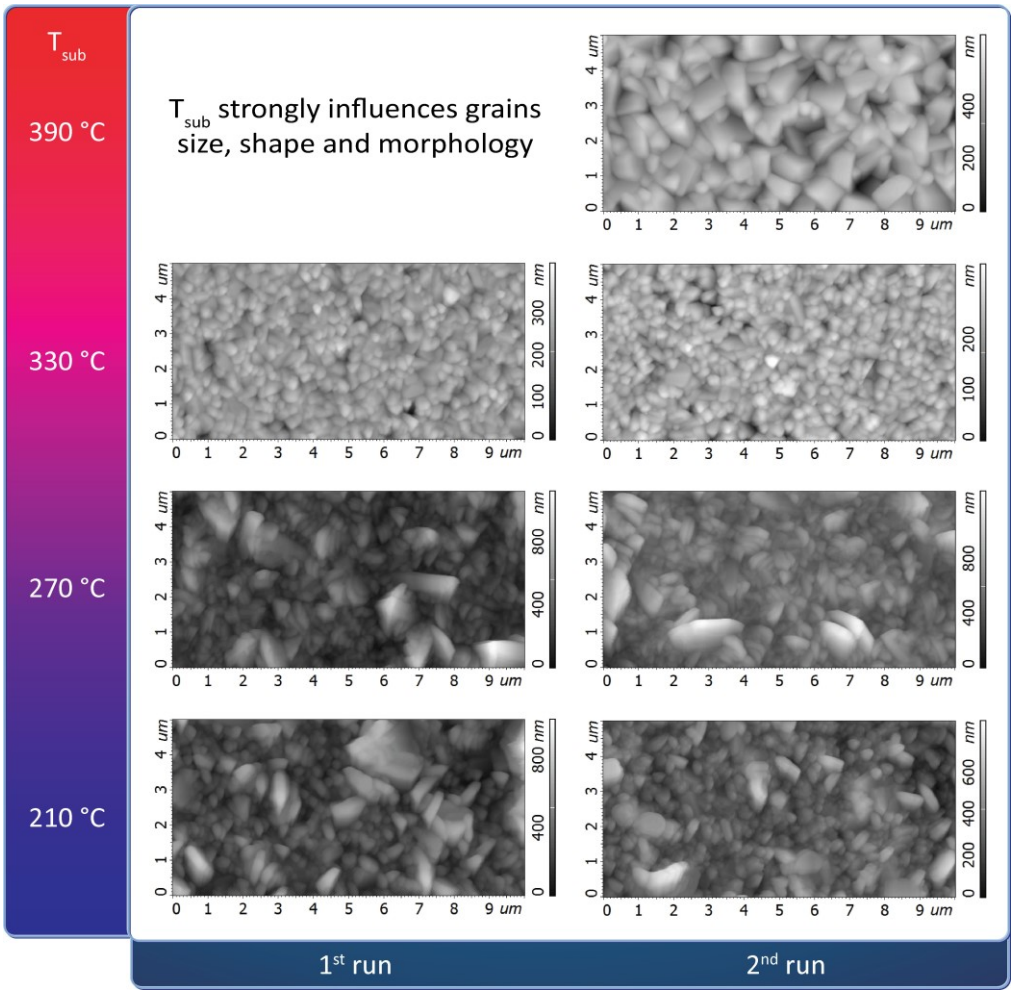

Fig. 4.15: The morphology of the SnS samples as function of the substrate temperature and the thermal history of the raw SnS material.

At 210 °C and 270 °C samples are characterized by a similar inhomogeneity in grain sizes: very big grains (over 1 µm) stand together with small grains (hundreds of nm). Moreover, while the shape of the bigger grains does not change increasing T_{sub} to 270 °C, the smaller grain shape seems to change from small "circular" grains to elongated ones. From the macroscopic point of view, the surface of the samples was easily damaged by scratches.

At T_{sub} = 330 °C the size distribution homogeneity has improved dramatically, only small circular grains with a diameter ≈ 500 nm are found.

Finally, at 390 °C, a very different morphology was found: big rectangular grains of over 1 µm appeared. In this case, small grains re-appeared, causing a decrease in the homogeneity of size distribution. Most likely at this T_{sub} value, the thin film suffered re-evaporation during its deposition.

The comparison of the samples belonging to the 1st run-set (left side of Fig. 4.15) to those of the 2nd run-set (right side) showed that the thermal history of the raw material seems not to affect the morphology.

Finally, the comparison with the works of Schneikart[62] and Kawano *et al.*[33], shows similar morphologies in the high temperature region (over 300 °C), while we cannot report the flake-like morphology at low temperature. We ascribe this evidence to the different substrate temperature scales discussed in Section 4.1.1.

4.3.1.2 X-ray diffraction

The XRD spectra of the samples are shown in Fig. 4.16. All the samples showed the main diffraction peaks of orthorhombic SnS, and T_{sub} influenced their crystalline structure as it does with their morphology.

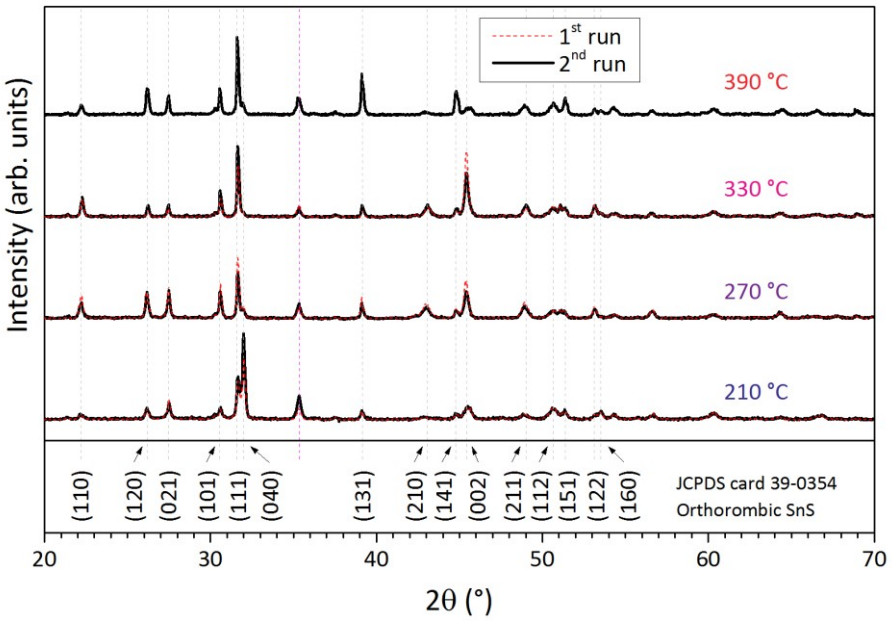

Fig. 4.16: The XRD diffraction pattern of the samples prepared at different T_{sub} values. The spectra of the 1st run-set (red dotted lines) are superimposed to those of the 2nd run-set (black lines).

The peak at 2θ ≈ 35 ° is due to the front contact.

The analysis of the XRD spectra confirms different preferential orientations of SnS thin films increasing T_{sub}. The studied T_{sub} range can be divided into three regions.

- Low T_{sub} region (210 °C). The reflections from the (111) and the (040) planes are the most intense peaks.
- Medium T_{sub} region (270 °C and 330 °C). This region is characterized by an intense (111) reflection, whereas the (040) one is weak. Furthermore, the (002) peak intensity increases as T_{sub} increases.

- High T_{sub} region (390 °C). The (111) reflection is still the dominant peak of the spectra. The intensity of both (040) and (002) peaks is weak, whereas the one of (131) increases significantly.

From the comparison of the XRD spectra of 1st run-set with those of the 2nd run one, no significant differences could be found. Only in the T_{sub} = 330 °C case there is a not negligible variation. In both the samples the most intense peaks are those due to the (111) and (002) reflections, but in the 1st run sample the (002) peak is more intense of the (111) one, while in the other case the opposite has been exhibited.

4.3.1.3 Raman Spectroscopy

A representative of the Raman spectra recorded from the samples are shown in Fig. 4.17. The effects of the change in T_{sub} value are visible also in the Raman spectra even if a clear trend cannot be recognized. The main Raman peaks of SnS are visible, furthermore no peak is present in the region above 300 cm^{-1}: this means that ours SnS thin films seems to be free from Sn_2S_3 and SnS_2 phases at any T_{sub} value.

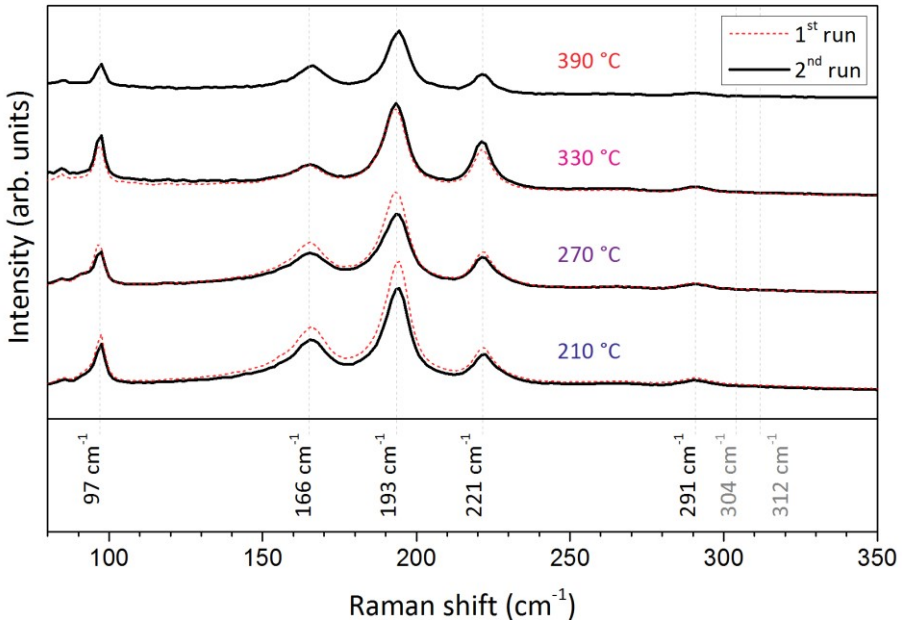

Fig. 4.17: Raman spectra of the samples prepared at different T_{sub} values. The spectra of the 1st run-set (red dotted lines) are superimposed to those of the 2nd run-set (black lines).

Comparing these spectra with the ones of the raw SnS material, the Raman peak positions are slightly changed (from 1 to 3 cm^{-1}). This can indicate the presence of stress in the SnS thin film than the bulk SnS. Nevertheless, the small shift of the peak position that seems to affect the samples prepared at different T_{sub} values resulted to be within the experimental error. A more resolved measurement would probably lead to a

correlation between film stress and substrate temperature. This can be suggested as a future development.

The comparison among the Raman spectra shows that by changing T_{sub}, the relative intensity of the Raman modes changes. The most intense peak is always the 193 cm^{-1} mode, which corresponds to the symmetric stretching of the Sn-S bond. In all cases the 166 cm^{-1} mode is more intense than the 221 cm^{-1} one, expect for the 330 °C case. The first mode corresponds to the anti-symmetric stretching along the inter-layer direction while the second to the Sn-S bonding symmetric stretching. The peak at 221 cm^{-1} seems to increase it intensity by increasing T_{sub} in the 210-330 °C range. At 390 °C the peak is instead weak, and this weakening of the peaks at 390 °C happens also for the 97 cm^{-1} and 221 cm^{-1} Raman modes.

Finally, a clear trend is visible in the region between the mode at 97 cm^{-1} and the one at 166 cm^{-1}, where a plateau region appears by increasing T_{sub}.

As in the previous cases, the comparison between the 1st run and the 2nd run-sets shows a very similar behaviour between them.

4.3.1.4 J-V characteristic

In Fig. 4.18 the J-V characteristic of the best device of each sample is shown, whereas in Table 4.5 the electrical parameters averaged over all the sample devices are reported.

For both the sample sets, the best performance is achieved at T_{sub} = 270 °C, whereas at the other T_{sub} values the efficiency drops down.

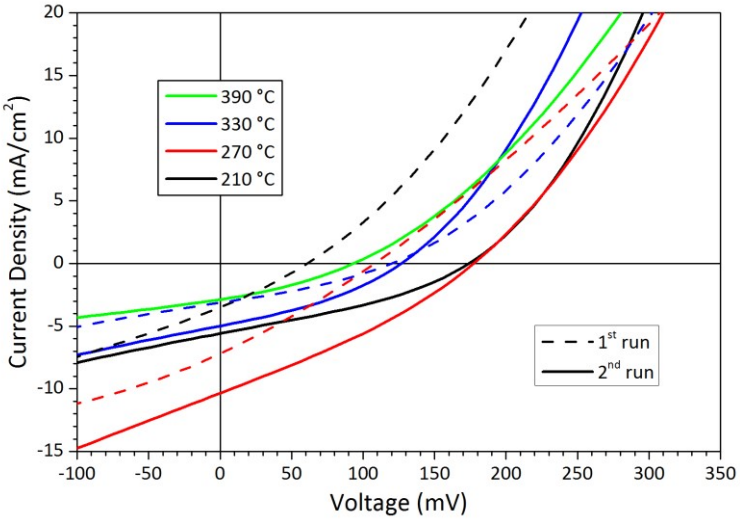

Fig. 4.18: The J-V characteristic of the samples prepared at different T_{sub} values belonging to the 1st run-set (dashed line) and to the 2nd run-set (continuous line).

Schneikart *et al.*[31] reported their best power conversion efficiency η = 1.6 % by depositing the absorber layer at T_{sub} = 250 °C, while Kawano *et al.*[33] have achieved a maximum power conversion efficiency η = 2.53 % at T_{sub} = 200 °C. Although we have a similar T_{sub} influence on grain size and shape but at a different T_{sub} scale, our result is not easily comparable to their ones due to the different T_{sub} measurement scale. Their devices exhibited the best performance at T_{sub} values higher than ours, i.e. where our devices showed the worst performance.

Table 4.5: The parameters of the 1st and 2nd run set of samples as a function of T_{sub}.

	T_{sub} [°C]	η [%]	F.F. [%]	V_{OC} [mV]	J_{SC} [mA/cm²]	R_P [Ω·cm²]	R_S [Ω·cm²]
2nd run	390	0.08 ± 0.01	31.2 ± 0.5	94 ± 3	-2.6 ± 0.2	57 ± 3	21 ± 1
2nd run	330	0.19 ± 0.02	33.5 ± 0.5	126 ± 3	-4.5 ± 0.3	47 ± 2	13 ± 1
1st run	330	0.10 ± 0.02	31.4 ± 0.9	112 ± 7	-2.7 ± 0.3	60 ± 2	23 ± 1
2nd run	270	0.50 ± 0.04	29.2 ± 0.6	179 ± 8	-9.6 ± 0.4	23 ± 2	11 ± 1
1st run	270	0.20 ± 0.01	26.7 ± 0.4	110 ± 4	-6.8 ± 0.2	19 ± 1	13 ± 1
2nd run	210	0.29 ± 0.02	34.0 ± 0.3	177 ± 1	-4.8 ± 0.3	53 ± 3	15 ± 1
1st run	210	0.05 ± 0.01	26.4 ± 0.9	60 ± 4	-3.3 ± 0.1	20 ± 1	14 ± 1

The investigation of the performance of the samples of the 1st run-set shows that by increasing T_{sub} a first increment of both V_{OC} and J_{SC} is observed, and this explains the power conversion efficiency increase; however, R_P and R_S exhibited a very slight decrease and F.F. remained almost unchanged. A further increase of T_{sub} halved the device efficiency, due to a dramatic J_{SC} reduction. The V_{OC} did not change significantly, whereas F.F. exhibited a 5 % increase. Finally, R_P became three times the previous value (good) but R_S became twice (bad).

From the analysis of the samples made during the 2nd run, again the first increment of T_{sub} improved the device performance, which is mainly due to a major increase of J_{SC} whereas V_{OC} remained at the same value. The F.F. is reduced by 5 % and R_P is halved. Also, R_S decreased. The device performance decreased also in this case due to the second T_{sub} increment: both V_{OC} and J_{SC} values resulted reduced whereas F.F., R_P and R_S did tend to re-establish the values they had in the 210 °C case. Finally, setting up T_{sub} to 390 °C further worsen the device performance. All the parameters (but R_P) show this trend.

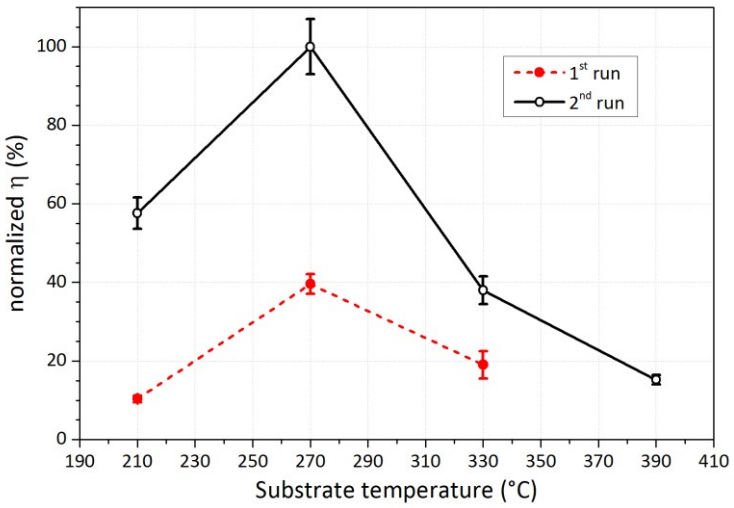

Fig. 4.19: The normalized efficiency of the samples produced by increasing T_{sub}. The samples of the 2nd run-set samples (black) always exhibited a better performance than those of the 1st run-set (red).

In Fig. 4.19 the comparison of power conversion efficiency as a function of T_{sub}, between the two sets of samples is shown. The efficiencies have been normalized to the overall best device value (100 %). This comparison shows that in every case the sample deposited during the 2nd run performed better than the other one. The improvement is at least doubling the performance showed by the 1st set of samples.

As we already discussed, the raw material can be purified by a thermal treatment, so the 1st run can be considered as a thermal treatment of the raw material for the 2nd run, i.e. in the last case the raw material can be purer than in the 1st run. Differently from what shown by Schneikart et al.[31], in our case, it is not possible to confirm or not if a thin SnS_2 layer would form directly on the CdS layer during SnS deposition, or if this layer would be deposited in different way in the two deposition processes. However, the presence or the absence of the SnS_2 layer could possibly explain the performance difference exhibited by the two sets of sample.

4.4 Conclusion

In this chapter our CdS/SnS based best solar device has been presented.

We achieved a power conversion efficiency comparable to the one achieved by Schneikart, at our knowledge the best performing device based on the CdS/SnS heterojunction deposited in superstrate configuration by thermal evaporation (SnS absorber layer).

Under light soaking, the device demonstrated firstly a performance improvement followed by its degradation. The sample performance was then irreparably deteriorated due to light soaking effect, and a constant degradation affected it during the following year.

Moreover, samples demonstrated poor reproducibility and we investigated the possible origin of this phenomenon. We observed a correlation between the raw material usage and the device performance thus we focused on that. The as-bought raw material has been analysed, demonstrating its purity in terms of its constituents (tin and sulphur) but not in terms of its phases – SnS_2 and Sn_2S_3 impurity phases were present as well. Therefore, the thermal treatment of the raw material has been investigated as a possible solution to the sample reproducibility issue. We have seen that an annealing at 500 °C in a dedicated furnace, in controlled atmosphere cannot remove all the impurities. On the other side, we observed that two sublimation/condensation cycles of the raw material inside the Knudsen cell were enough to clean it from the impurity phases. The same approach to SnS powder from SA resulted in the degradation of SnS to SnO_2.

For this reason, we decided to investigate the performance of SnS deposited in two consecutive processes of the same raw material, i.e. to study the SnS thermal history influence. Moreover, we decided to widen the investigation by studying in parallel also the influence of the substrate temperature on the SnS solar devices. The TRM raw material has been used with no thermal treatment before its use.

As expected, the substrate temperature parameter strongly affected the SnS thin film morphology, crystalline structure and vibrational dynamic as well as the device performance. This result is in agreement with those obtained in other studies. However, the thermal history of the SnS raw material seems to have no influence on morphology, crystalline structure and vibrational dynamic, whereas the device performance exhibited a dramatic change between the two sets of samples.

The best working devices for both the sets are those deposited at 270 °C, despite their morphology would not seems to be the most appropriate, especially because of the grain size distribution inhomogeneity. Surprisingly, the sample with the most appropriate morphology (T_{sub} = 390 °C) led to the worst power conversion efficiency. We can suggest that Schneikart and Kawano in their studies obtained their best working devices in similar conditions (high T_{sub} values).

Finally, from the comparison of the properties of the two sets of samples, it seems that only minor variations are present. On the other hand, the performance of the samples belonging to the 2nd run-set improved the performance of those of the 1st run-set sample of more than a factor 2. We hypothesize that a main difference has thus to be enclosed near the junction region – a region non-accessible to surface techniques like Raman or EDX spectroscopy – an example of which could be the SnS_2 thin layer forming on the CdS buffer layer, as reported by Schneikart.

Chapter 5.

POST-DEPOSITION TREATMENTS

The activation treatment in the CdS/CdTe heterojunction case requires the sample annealing at high temperature with the presence of a chlorine containing molecule, for example $CdCl_2$[64], $MgCl_2$[65] or $CHClF_2$[66], which have been recently studied in our laboratory. The annealing gives enough energy to the materials to react. After the thermal treatment, the CdTe layer has recrystallized to a better organized structure: enlarged grains, decreased defect density and passivated grain boundaries. The performance parameters resulted strongly improved and thus the device efficiency.

Also in the SnS case, a treatment has been showed to be very effective. The SnS thermal treatment in the presence of the H_2S gas is one of the key factors which leaded to the record efficiency device [16,32,54]. In these works, a Zn(O,S)/SnS heterojunction based solar cells were deposited in substrate configuration on a molybdenum back contact layer. The SnS layer was deposited by thermal evaporation by Steinmann *et al.*[32] or by Atomic Layer Deposition (ALD) by Sinsermsuksakul *et al.*[16] and Hartman *et al.*[54], and consequently annealed in a H_2S/N_2 mixed atmosphere at a temperature of 400 °C for 60 min. This annealing was used to recrystallize the SnS layer which is thus “optimized” for the buffer layer deposition.

As seen in Section 4.3, our devices did not exhibit their best performance on the SnS layer with the most appropriate morphology, i.e. the one obtained depositing SnS at high T_{sub} value (T_{sub} > 330 °C). In this chapter, we will focus our attention on the possibility of improving the SnS performance by improving its structure by applying a Post-Deposition Treatment (PDT).

We can divide the thermal treatments applied to the SnS solar devices into the two groups drafted in Fig. 5.1.

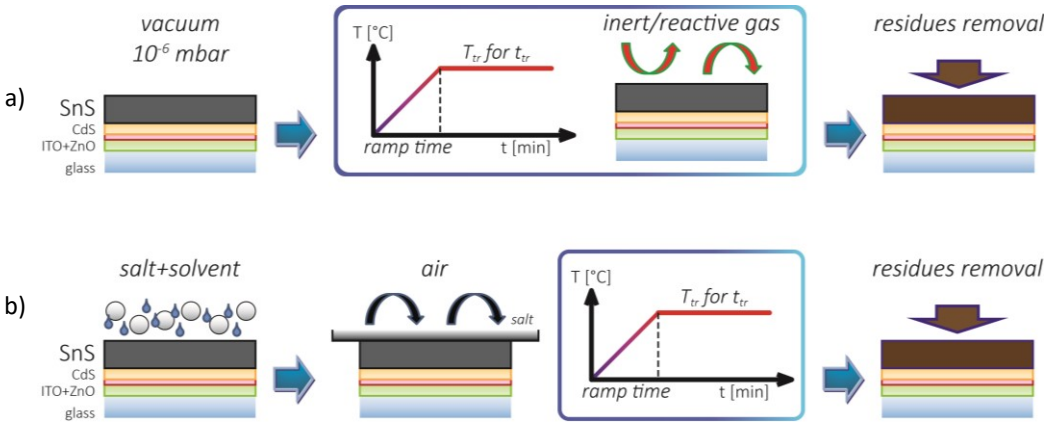

Fig. 5.1: A scheme of the two applied treatment groups: a) the annealing in controlled atmosphere and b) the "wet" treatment.

The annealing can be applied inside a vacuum chamber in controlled atmosphere, where the reactant is eventually contained as a gas (Fig. 5.1-a). Otherwise, the treatment can be applied in the "wet" form (Fig. 5.1-b). In this case, the reactant has been dissolved in a solution with an organic solvent (typically methanol in the $CdCl_2$ case) at a known concentration. Thus, a fixed amount of the solution would be deposited on the sample surface, the solvent was let to evaporate to leave a thin layer of the reactant. The sample was finally annealed in air into a furnace.

The samples were treated soon after the SnS absorber layer deposition. To compare the treated sample with a reference, the samples – 3x3 cm^2 glass squares – were broken into two pieces, one will be the reference, i.e. the as-deposited sample, which will be completed with the Au back contact layer deposition with no further modification, while the other one undergoes the treatment and after it there will be the back contact deposition.

Part of the present work – Section 5.1.2, Section 5.1.3 and Section 5.2.1 – has been presented and published in the PVSEC 2015 conference proceeding[59], whereas Section 5.2.2 was presented and published at the 43rd IEEE Photovoltaic Specialist Conference (PVSC) 2016 conference proceeding[67].

5.1 PDT in controlled atmosphere

In this section three PDTs will we applied to the SnS solar devices. These treatments will be applied inside a quartz tube furnace, equipped with inlets for the separate circuits of Ar and Freon® R-22 gases.

The following PDTs will be applied to SnS solar cells.

- Annealing in vacuum.
- Annealing in Ar atmosphere.
- Annealing in reactive atmosphere – a Freon®/Ar mixture.

5.1.1 Annealing in vacuum

This treatment followed the sample deposition. After both the sample and the source cooled down the heat fed for the deposition process, the sample was taken from the evaporation machine, broken into two parts (for the reference), and thus one part was moved back in the machine and annealed. The annealing lasted for t_{tr} = 30 minutes at a temperature T_{tr} = 350 °C.

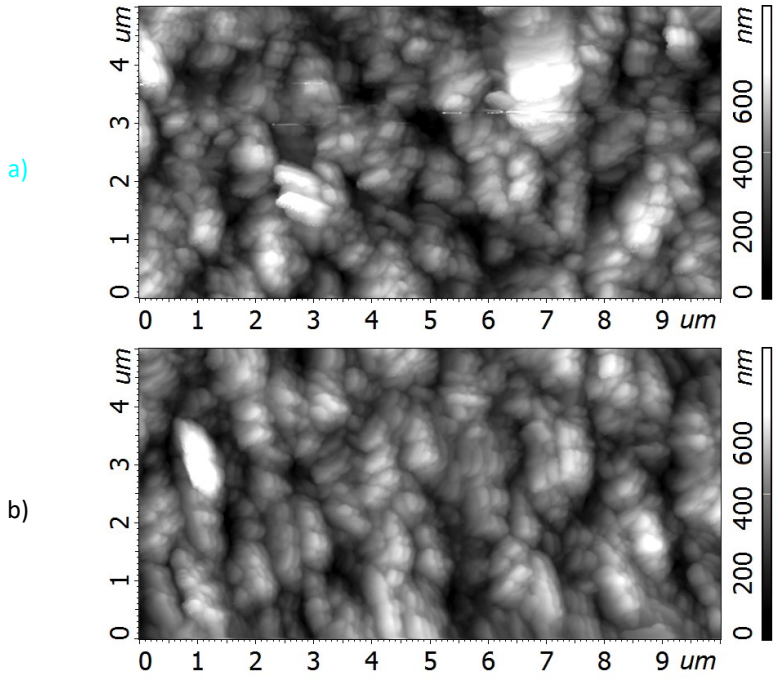

Fig. 5.2: The morphology of the SnS samples a) annealed in vacuum for 30 minutes at 350 °C and b) as deposited.

In the following only one sample will be shown, since very similar effects were exhibited after the thermal treatment. The sample that will be discussed has been deposited at

T_{sub} = 150 °C, while the other parameters were the same of the samples shown in the previous chapter (SnS layer thickness of 2 µm, deposited at a rate of 0.5 nm/s).

In Fig. 5.2 the morphology of the sample before and after the thermal treatment is reported. It seems that the treatment did not affect the SnS morphology. Grains with similar properties (size, size inhomogeneous distribution, and shape) are present in both cases.

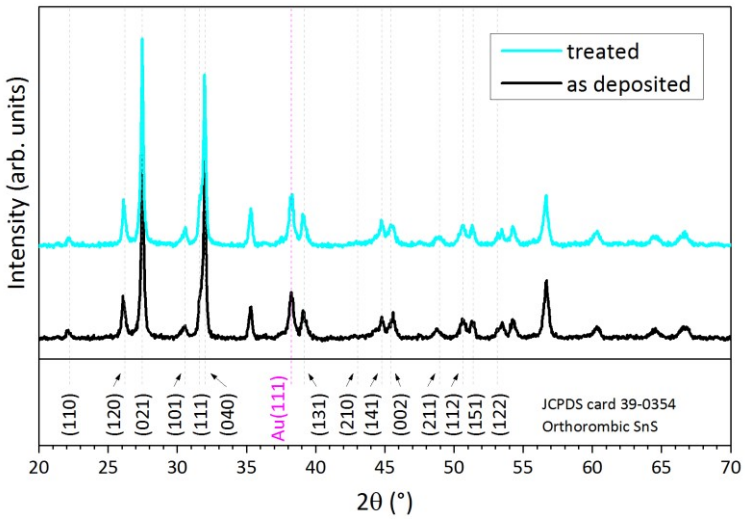

Fig. 5.3: XRD pattern of the as deposited sample (black) and the one after its annealing in vacuum (cyan).

Fig. 5.3 shows the XRD patterns of the non-treated sample compared with the one annealed in vacuum. The diffraction spectra are very similar; it does not seem the annealing had modified the sample microcrystalline structure.

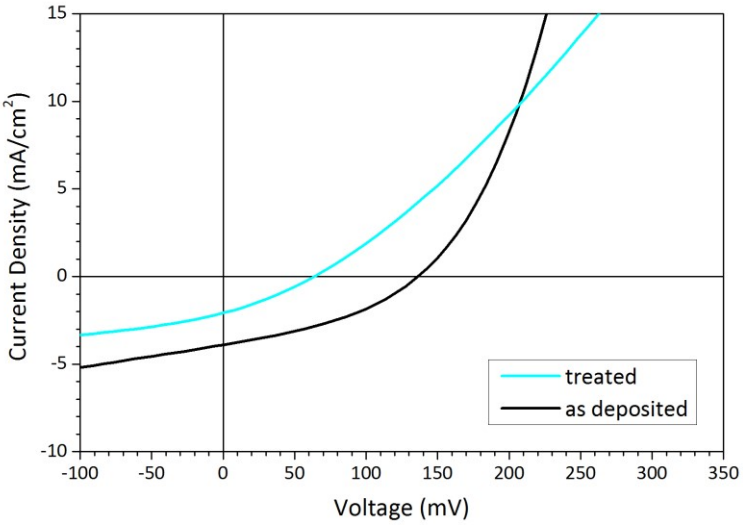

Fig. 5.4: J-V characteristic of the as deposited sample (black) compared with the treated one (cyan).

Finally, in Fig. 5.4, the J-V characteristic of the best cell of the as-deposited sample is compared to the best one of the treated sample. It is evident that the annealing process degraded the sample performance. Comparing the main parameters variation (Table 5.1) it is possible to see how the thermal treatment degraded the performance of all the parameters. We think the thermal treatment could have strongly damaged the non-optimal CdS/SnS heterojunction.

Table 5.1: The working parameters of the as deposited solar cell compared with the treated one (in vacuum).

	η [%]	F.F. [%]	V_{OC} [mV]	J_{SC} [mA/cm²]	R_P [Ω·cm²]	R_S [Ω·cm²]
treated	0.04	29.8	64	-2.1	45	22
as deposited	0.20	35.9	142	-3.9	72	13

Finally, it is interesting to compare the morphology of Fig. 5.2-b and the as deposited XRD pattern of Fig. 5.3 with those discussed in Section 4.3 (Fig. 4.14 and Fig. 4.16), studying how the reduction of T_{sub} below 210 °C affects these thin film properties. We can see at T_{sub} = 150 °C a more complex morphology characterized by grains with a smaller size than those of the T_{sub} = 210 °C case, whereas the grain size distribution inhomogeneity of the sample is similar. Moreover, the XRD pattern shows a different structure than those showed in Fig. 4.16. We highlighted that by decreasing T_{sub} the intensity of the (111) peak – the dominant one at high T_{sub} – is decreased, while the (040) peak one increased – and thus it becomes the dominant peak at low T_{sub}. At lower T_{sub}, like in this case, (040) is still one of the main peak, but the (021) one becomes more intense indicating another microcrystalline structure, as the AFM scans seem to confirm. Nevertheless, the performance of this device cannot be compared to the performance of the sample of Section 4.3.4 since this sample was prepared without all the precaution taken for depositing those ones.

5.1.2 Annealing in Ar inert atmosphere

This thermal treatment took place into a quartz tube furnace, where an inert atmosphere of Ar has been inserted at a treatment pressure of 300 mbar. The PDT duration was t_{tr} = 30 minutes at a temperature T_{tr} = 500 °C. Also in this case, only the most important sample is shown, since the response to the treatment was very similar for all the samples: it has been deposited at T_{sub} = 300 °C, and at an evaporation rate of 0.5 nm/s. The SnS layer has a thickness of 2 µm.

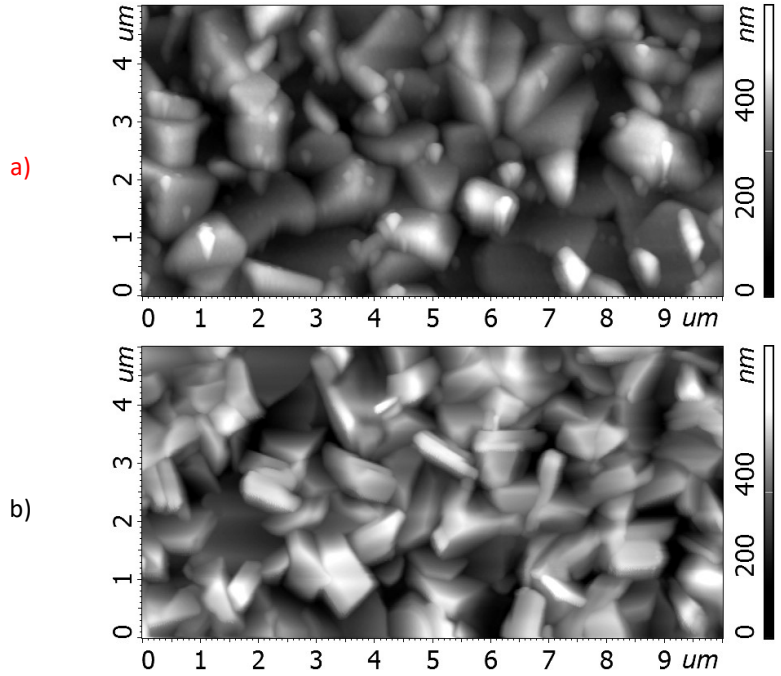

Fig. 5.5: The morphology of the SnS samples a) annealed in inert atmosphere for 30 minutes at 500 °C and b) as deposited.

The morphology of the reference sample is shown in Fig. 5.5-b, while the one of the SnS thin films annealed in Ar atmosphere at 500 °C is shown in Fig. 5.5-a. Some of the grains were restructuring and small new grains were forming. A similar effect has been observed in the case of CdTe recrystallization[68] after $CdCl_2$ activation treatment. This suggests that the SnS recrystallization process was starting at a temperature of 500 °C. Despite the high annealing temperature, only a weak change in film morphology was observed, and not a strong recrystallization of the SnS films.

We observed a variation of the colour of the sample surface, which acquired a yellowish component. Moreover, at the opening of the furnace quartz tube an intense sulphur smell was perceived. These facts would suggest that the SnS samples suffered from sulphur losses from the SnS matrix.

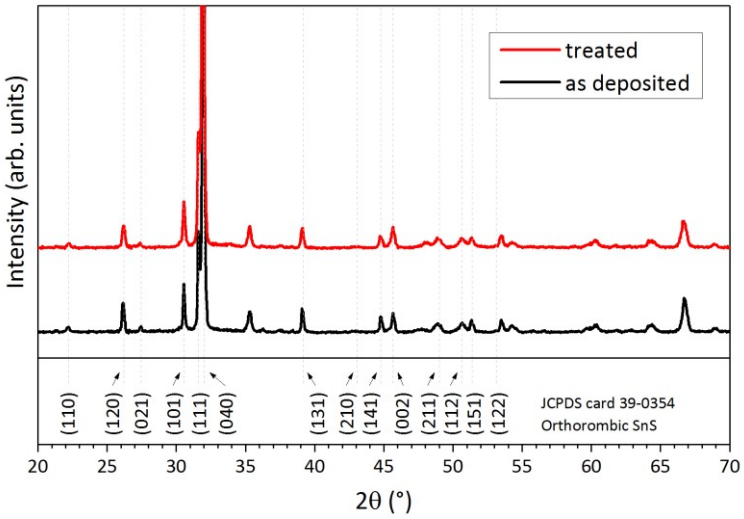

Fig. 5.6: XRD pattern of the as deposited sample (black) and the one after the PDT in inert atmosphere (red).

In Fig. 5.6 the XRD spectra of as deposited and treated SnS films are shown. No significant change has been observed by comparing the two XRD spectra.

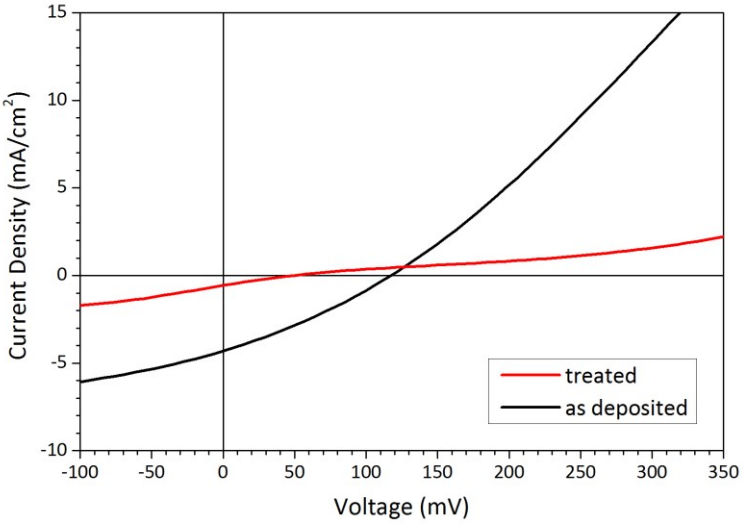

Fig. 5.7: J-V characteristic of the as deposited sample (black) compared with the treated one (red).

In Fig. 5.7, the J-V characteristic of the as deposited sample best cell is compared to the treated sample best cell. It is even more evident than in the previous case in Section 5.1.1, that the annealing process strongly degraded the sample performance, to the point that the cell lost its rectifying ability. All the parameters of the treated sample in Table 5.2 show the detrimental effect due to the high temperature thermal treatment.

Table 5.2: The working parameters of the as deposited solar cell compared with the treated one (in Ar inert atmosphere).

	η [%]	F.F. [%]	V_{OC} [mV]	J_{SC} [mA/cm²]	R_P [Ω·cm²]	R_S [Ω·cm²]
treated	0.01	22.7	50	-0.6	80	109
as deposited	0.15	29.1	120	-4.3	40	19

In our opinion, we are facing the same degradation process discussed in the previous case, but amplified from the higher T_{tr} value. The inert gas pressure helped only to reach higher treatment temperature without re-evaporating the whole stack. It seems that our samples have a very fragile junction that cannot tolerate strong PDTs.

5.1.3 Annealing in Freon® R-22 reactive atmosphere

The annealing in reactive atmosphere took place into the quartz tube furnace. The CdTe thermal treatment in Freon® R-22 gas has been demonstrated to be an efficient replacement for the $CdCl_2$ treatment[66]. Freon® R-22, or chloro(difluoro)methane ($CHClF_2$) is a greenhouse gas banned in EU with Regulation (EC) No. 1005/2009, and thus it can be only used for laboratory and analytical purposes[69]. However, for this application, many other chlorine containing gases can be used in place of Freon® since it has been chosen as a chlorine vector.

To facilitate SnS layer recrystallization by applying a PDT in reactive atmosphere, and Freon® R-22, a chlorine containing gas, has been chosen as reactant. The treatment lasted t_{tr} = 30 minutes, while the environmental conditions – i.e. the treatment temperature T_{tr}, and the Ar/Freon® R-22 partial pressures – were changed. We decided to study the T_{tr} in the 200÷300 °C range, since we demonstrated in the previous sections that too high annealing temperatures were detrimental to our samples. The chamber atmosphere was a mixture of Ar/$CHClF_2$; the Ar partial pressure was fixed to 500 mbar, while the $CHClF_2$ partial pressure was varied in the 5÷20 mbar range.

As the previous section, we will report only the most important sample, since the response to this PDT was similar for all the samples. The 2 µm of the SnS layer were deposited at T_{sub} = 270 °C, and at an evaporation rate of 0.5 nm/s. This sample was treated for 30 minutes at the temperature T_{tr} = 300 °C in a mixed atmosphere of 10 mbar of $CHClF_2$ diluted in 500 mbar of argon.

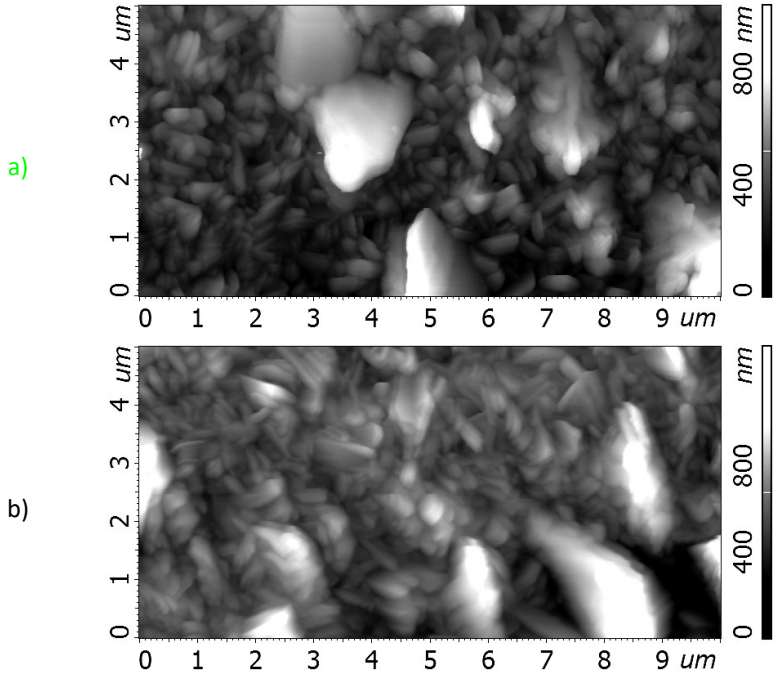

Fig. 5.8: The morphology of the SnS samples a) annealed in reactive atmosphere for 30 minutes at 500 °C and b) as deposited.

As shown in Fig. 5.8, where the as-deposited sample morphology is depicted below the treated sample one, no sign of SnS re-crystallization can be find due to the PDT in reactive atmosphere.

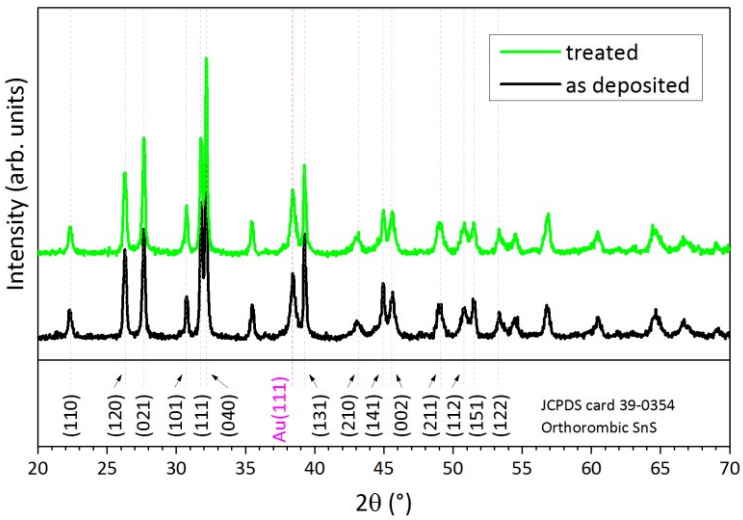

Fig. 5.9: XRD pattern of the as deposited sample (black) and the one after the PDT in reactive atmosphere (green).

The XRD patterns are shown in Fig. 5.9. XRD confirms the morphological analysis: there is no experimental evidence of any recrystallization process happened to this sample, as well as in all the SnS solar device to whom this PDT has been applied. The absence of any effect on morphological and microstructural characteristics of the SnS thin

films could be probably due to the annealing temperatures region which has been investigated, i.e. below 300 °C. In fact, in the CdTe case, the typical annealing temperature is $T_{tr} \approx 400$ °C, where Freon® R-22 gas dissociates, releasing its reactive component – chlorine[70].

In Fig. 4.16, it has been shown that at $T_{sub} = 270$ °C the main diffraction peak is the (111) whereas the (040) one is not very intense, and this is due to the microstructure evolution due to T_{sub} variation. In Fig. 5.9, the sample – deposited at the same T_{sub} value – exhibited a (040) peak more intense than the (111). This is not in contrast with the XRD peak evolution due to T_{sub}, discussed in Section 4.3. In fact, the XRD pattern of several samples deposited at this T_{sub} value – 270 °C – showed both the cases. The most interesting one – not shown – is the one where the two peaks exhibited a similar intensity. In our opinion, $T_{sub} = 270$ °C represents the turning point, i.e. the growth condition in which the sample can exhibit both trends.

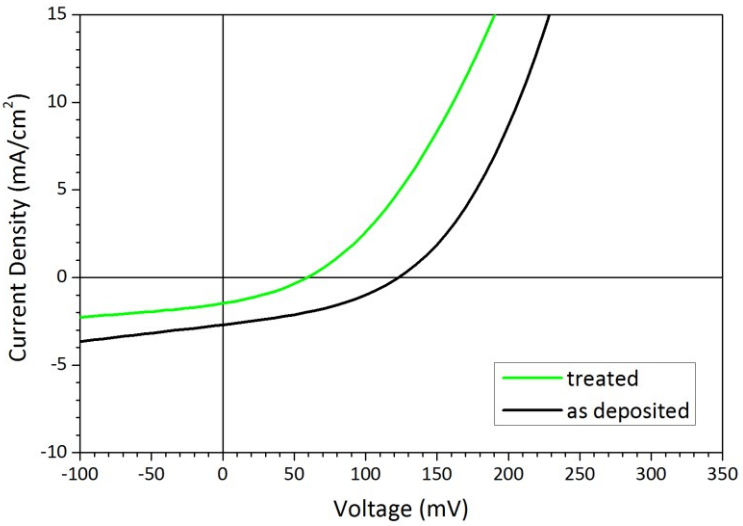

Fig. 5.10: J-V characteristic of the as deposited sample (black) compared with the treated one (green).

Although the PDT was ineffective, we can confirm again that any tentative to anneal SnS thin films result in the degradation of the performance, as shown in Fig. 5.10 and by the sample working parameters which are summarized in Table 5.3.

Table 5.3: The working parameters of the as deposited solar cell compared with the treated one (in Ar/Freon® R-22 atmosphere).

	η [%]	F.F. [%]	V_{OC} [mV]	J_{SC} [mA/cm²]	R_P [Ω·cm²]	R_S [Ω·cm²]
treated	0.03	30.5	64	-1.5	70	20
as deposited	0.13	36.5	128	-2.7	99	16

5.2 “Wet” PDTs in air

The application of all the PDTs discussed so far (Section 5.1) resulted to be ineffective to reach SnS recrystallization, maybe due to low treatment temperatures. On the other side, we saw how fragile are our samples, since their performance resulted deteriorated after the treatments.

In this section, we will study three other PDTs, those belonging to the “wet” treatment group. As described in the introduction, “wet” only means the way with which the reactant is deposited on the sample. Also in this case, the idea behind these PDTs is that we want to help the recrystallization process by bringing a reactant on the sample surface, and with the consequent annealing of the sample we want to drive the reaction that should recrystallize the sample.

The following reactants will be applied to the SnS solar cells.

- $CdCl_2$ – this is the most important reactant in the CdTe field.
- $SnCl_2$.
- KI.

The choice of $SnCl_2$ and KI is due to a recent paper[71] in which the recrystallization at high temperature of SnS crystals in presence of these two molten salts has been demonstrated. These salts are particularly interesting since they are *non-toxic*. Moreover, since these salts are very soluble in most organic solvents, they are also *easy to be used*.

5.2.1 $CdCl_2$ activation treatment

As reactant vector a saturated solution of $CdCl_2$ in methanol, which has been further diluted in the same volume of methanol has been used[64]. Our standard procedure requires the deposition of 6 drops of solution on the sample surface. The solvent evaporation was aided by heating the sample at 55 °C on a hot plate. Then, the sample was moved into a furnace where the thermal annealing will take place. The furnace is able to reproduce a temperature ramp by only setting the ramp time – usually 25 minutes – at which end the typical treatment temperature T_{tr} = 380 °C was reached and maintained for the whole treatment duration t_{tr} = 30 minutes. Since the annealing takes place in air, the treated surface resulted oxidized and thus an etching was required prior to deposit the back contact. Usually treated samples were etched in a solution of bromine in methanol, Br-MeOH.

As in Section 5.1, only the most important result will be shown. The treated sample which will be discussed is constituted by a 2 µm-thick SnS layer deposited at a substrate temperature of T_{sub} = 250 °C and an evaporation rate of 0.5 nm/s.

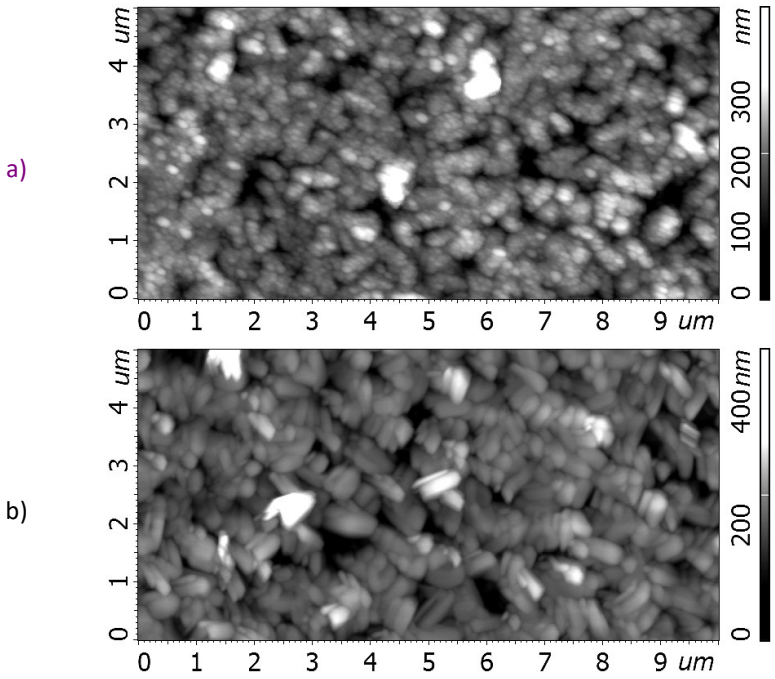

Fig. 5.11: The morphology of the SnS samples a) treated with $CdCl_2$ and b) as deposited.

In Fig. 5.11 the morphology of the as-deposited samples along the one of the $CdCl_2$ treated one. The recrystallization process of the SnS took place, although we found a reduced grain size, and the shape of grain changed to small spheres.

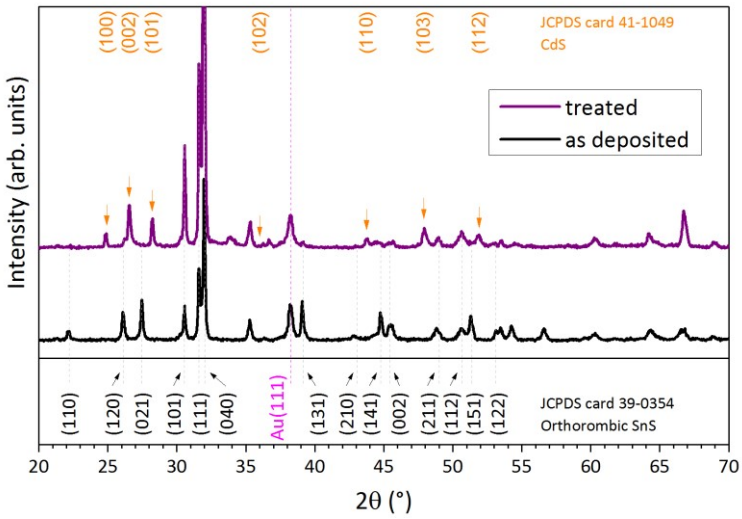

Fig. 5.12: XRD pattern of the as deposited sample (black) and the $CdCl_2$ treated on (purple).

The XRD spectra shown in Fig. 5.12 clarify the range of the modification induces by the $CdCl_2$ treatment to the sample. The XRD pattern of the treated sample exhibits several peaks which are not present in the as deposited one. It resulted that these peaks belong to the CdS buffer layer. The $CdCl_2$ treatments were so strong that the SnS recrystallization was achieved, but a remarkable intermixing of the two layers forming the CdS/SnS heterojunction was observed and most probably also part of the SnS could be lost.

Due to the damages caused by the $CdCl_2$ treatment to the junction, is worthless to show how the J-V characteristics of the treated samples resulted modified – they exhibit an ohmic behaviour.

5.2.2 $SnCl_2$ and KI “wet” PDTs

As said, it has been demonstrated that potassium iodide or stannous chloride molten salts induce SnS crystal recrystallization. To apply KI and $SnCl_2$ based PDT, in a similar manner to the $CdCl_2$ wet treatment, the two salts were dissolved into different solvents at different concentrations. The PDT is applied as the $CdCl_2$ case: the sample is prepared for the PDT by depositing a known amount of solution on its surface, the solvent is let to evaporate, thus a thin layer of the salt results formed. Finally, the annealing of the sample causes the reaction to occur.

The treatment lasts for 30 minutes after the temperature ramp set to 20 minutes. The typical treatment temperatures T_{tr} were 450 °C in the KI case and 350 °C in the $SnCl_2$ one. After the treatment, the samples were etched and/or cleaned by rinsing with de-ionized water to remove the residues of the treatments.

5.2.2.1 Etching of Treated Samples

In the inset of Fig. 5.13 the sample surface after thermal treatments is shown. The EDX analysis detected a very large Sn signal, suggesting that sulphur loss was taking place. However, measurements performed under higher electron accelerating voltages (30 kV), which penetrates deeper into the layer, show a different stoichiometry more similar to the expected one. Therefore, considering the high penetration of X-Rays (which will be discussed later) the combined results of XRD and EDX demonstrates that only the treated sample surfaces are Sn rich, while in the bulk, the layer seems to be SnS with a different recrystallized structure.

To study the effects of the post deposition treatment on SnS films, different etching procedures were applied to remove the Sn-rich layer and to study the structure under it.

Mainly two different cleaning procedures were applied: rinsing in water (with ultrasonic bath) or in ammonia solution. Also bromine-methanol etching has been applied with the procedure used for our standard CdTe solar cells fabrication process[72], however it was not successful.

In Fig. 5.13 the effect of water on $SnCl_2$ treated samples is shown. The large smooth grains are removed (only partially in Fig. 5.13) and EDX analysis reveals that there is no Sn-rich layer on the surface.

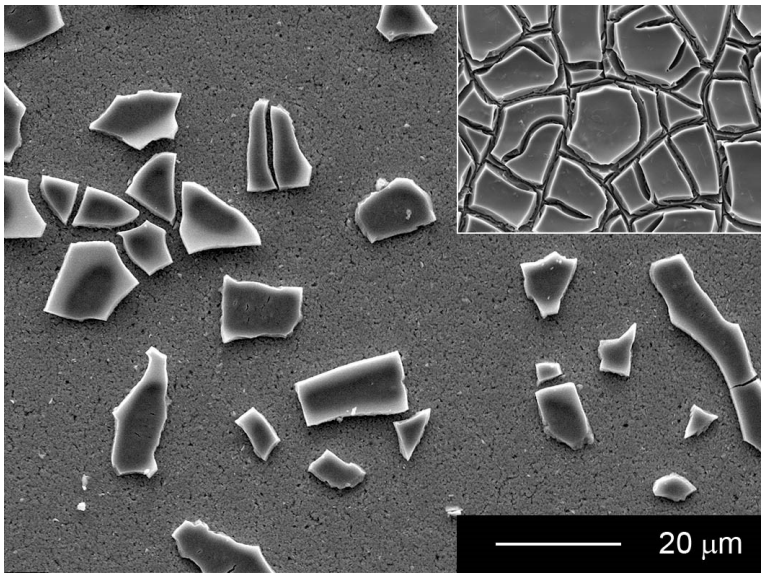

Fig. 5.13: SnS morphology after $SnCl_2$ treatment (inset) and after rinsing in water. Untreated SnS layer were deposited at a substrate temperature of 400 °C.

In order to improve the cleaning quality, some samples were also dipped in ammonia solution (30 %) and processed in ultrasonic bath for 5 minutes. The residues layer with large plate grains is further removed, and the morphology below it will be discussed. The EDX measurement performed on the residues shown in Fig. 5.13, detected mainly Sn and O, and only negligible signal from S and Cl. The oxidation of the layer due to the thermal treatment performed in air is a common result with the $CdCl_2$ treatment.

Samples exhibiting strong layer intermixing after the treatment application, like those deposited at low substrate temperature depicted in Fig. 5.15-b and Fig. 5.15-c, were instead non-sensitive to any cleaning procedure.

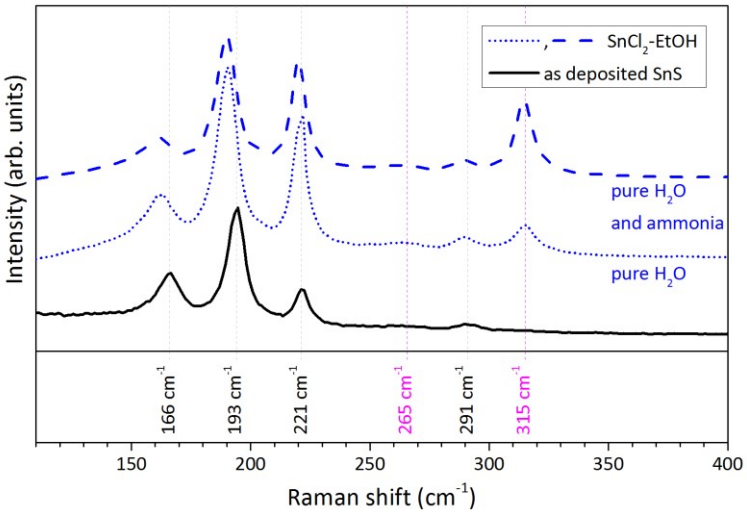

Fig. 5.14: Raman spectra of as deposited SnS films (black line), of $SnCl_2$ treated samples after the cleaning process in pure water (blue dotted line) and in pure water and in ammonia (blue dashed line).

The Raman spectra of the sample treated with $SnCl_2$ are reported in Fig. 5.14. The main SnS peaks are present after the treatment, even if the 166 and 193 cm^{-1} modes are shifted to lower energies. The shift of the 221 and 291 cm^{-1} modes is instead smaller. After the treatment, two new modes appear at 265 and 315 cm^{-1}, and it seems that the cleaning procedure further enhance their intensity. The peak at 315 cm^{-1} could be explained by the presence of SnS_2[18] on the sample surface shifted to higher energies due to the treatment. EDX measurements showed a slightly sulphur rich composition of the surface, in agreement with Raman spectroscopy results.

The PDTs were applied to two sets of samples, those deposited at T_{sub} = 270 °C – those which exhibited the best device performance – and those deposited at T_{sub} = 400 °C – the samples with the most appropriate morphology for thin film devices purpose – thus it is useful to briefly summarize the as-deposited morphology exhibited by the SnS thin films for the following comparisons.

In Fig. 5.15-a is depicted the morphology of the SnS thin film grown at T_{sub} = 270 °C, which is constituted by several clusters larger than 1 µm surrounded by flake-like grains of hundreds of nm. In Fig. 5.16-a is instead shown the case of the SnS film grown at T_{sub} = 400 °C, which exhibits a different morphology constituted by big rectangular grains (which size is about 1 µm or more).

5.2.2.2 PDTs effects on SnS morphology

The KI salts were dissolved in 0.95 M methanol (MeOH) and in 0.15 M ethanol (EtOH). The PDT has been performed under different experimental conditions: we deposited 100 µl or 300 µl of either KI-MeOH or KI-EtOH solutions.

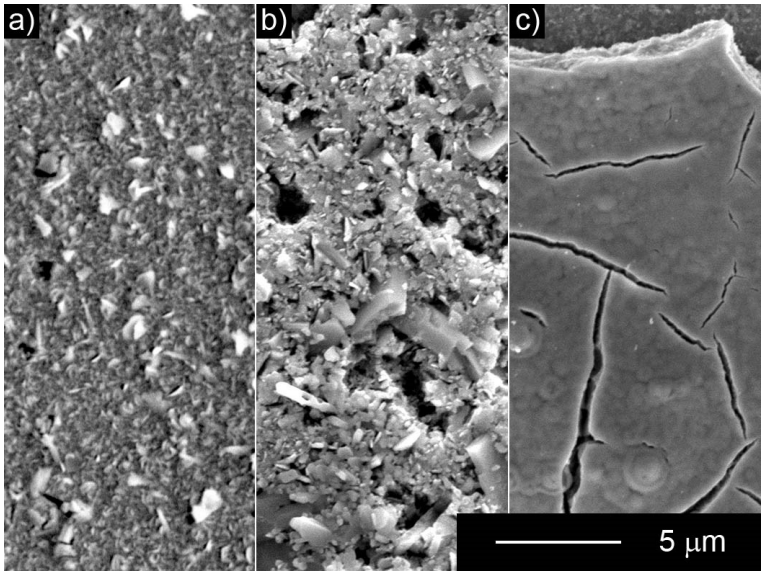

Fig. 5.15: SEM images of the a) as-deposited, b) KI treated, and c) $SnCl_2$ treated SnS films, grown at T_{sub} = 270 °C.

In Fig. 5.15-b is shown the effect of the KI PDT on the morphology of the SnS thin film deposited at T_{sub} = 270 °C. The sample has been treated at T_{tr} = 450 °C with 300 µl of KI-EtOH. After the thermal treatment, the morphology changed: the film resulted in a more porous and less compact structure. KI caused the dissolution of the SnS film, and most probably also of the underlying layers. After recrystallization, grains tend to concentrate into clusters with big boundaries. EDX measurements revealed the presence of some secondary phases with mixed composition, constituted of Sn, S, I, K, O, Zn inside these boundaries.

When the PDT is applied to a sample grown at the higher T_{sub} value, 400 °C, the morphology of the treated sample did not change significantly (see Fig. 5.16-b). In this case, EDX measurements indicated that the treated film has the correct stoichiometry of tin and sulphur, together with residues of K, but not of I.

The $SnCl_2$ salts were dissolved in 0.6 M isopropyl alcohol (IPrOH) and in 2.2 M ethanol. The $SnCl_2$ PDTs were applied with a fixed volume of $SnCl_2$ solution – 100 µl.

The first applications of the $SnCl_2$ PDT at T_{tr} = 450 °C resulted in very strong modification of the stacks, with a strong interdiffusion of the constituent layers occurred to the point that all the layers were mixed together. The sample colour turned from grey

to yellow. Moreover, the samples treated with $SnCl_2$ solutions at the higher concentration – the EtOH one – during EDX measurements showed an important (up to 15 %) signal from chlorine: this suggests the presence of an upper threshold, above which not all SnS reacts with chlorine. For this reason, we reduced the concentration of both solutions (EtOH and IPrOH) to less than 20 % of the initial values; at the same time, the treatment temperature has been reduced to 350 °C.

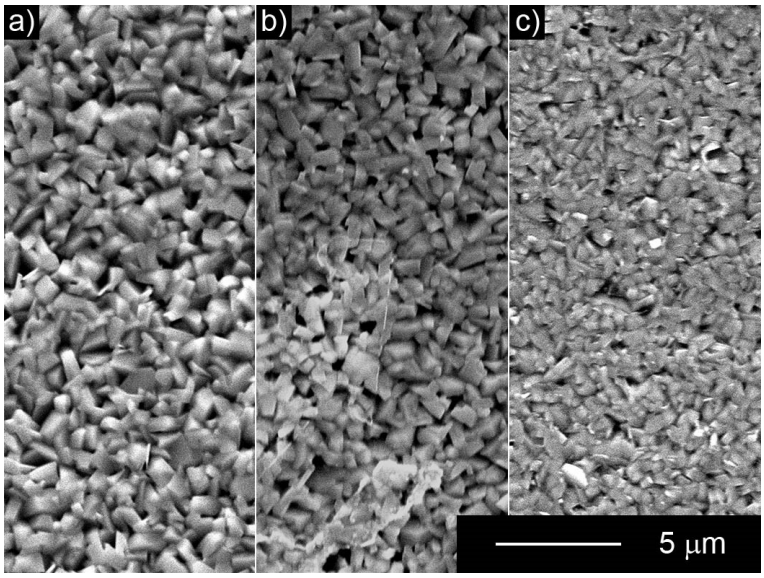

Fig. 5.16: SEM images of the a) as-deposited, b) KI treated, and c) $SnCl_2$ treated SnS films, grown at T_{sub} = 400 °C.

The morphologies of the SnS layers after the treatment with $SnCl_2$-EtOH (0.3 M) at 350 °C are shown in Fig. 5.15-c and Fig. 5.16-c.

The morphology of the sample deposited at 270 °C (Fig. 5.15-c) changed significantly after the $SnCl_2$ treatment: the layer is constituted by several domains, separated by deep fractures. Part of the film delaminated from the substrate. EDX analysis highlighted a consistent loss of sulphur, and the oxidation of the surface, most likely a SnO_2 layer formed.

The sample grown at a substrate temperature of 400 °C exhibits a modified morphology (Fig. 5.16-c). After the application of the PDT, the film seems more compact, but grain size is reduced and the grain shape changes to less regular structures. In this case, the elemental analysis showed a stoichiometric SnS film after the treatment. Only traces of Cl were found by EDX measurements on samples treated with $SnCl_2$, independently from the SnS layer preparation and from the PDT application parameters.

5.2.2.3 PDTs effects on SnS microcrystalline structure

Fig. 5.17 shows the XRD patterns of the as deposited, and of the Ki and $SnCl_2$ treated SnS samples which morphology has been discussed so far. Only the XRD spectra of the treated samples which were deposited at T_{sub} = 400 °C are reported. Those deposited at T_{sub} = 270 °C only confirm how much the treatments were strong and their detrimental effects affected to the whole sample stacks.

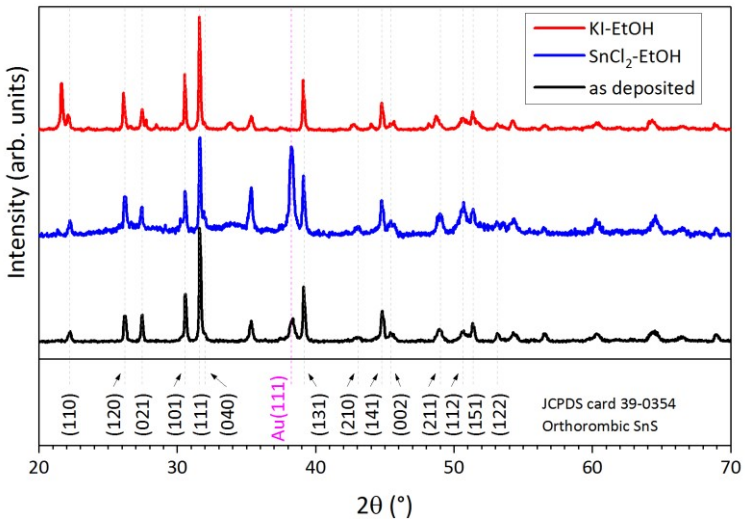

Fig. 5.17: XRD patterns of the as-deposited (black), $SnCl_2$ treated (blue) and KI treated (red) SnS samples, grown at T_{sub} = 400 °C.

The comparison of the KI treated XRD pattern with the as-deposited one highlights that the thermal treatment resulted in a mixture of different phases, SnS, Sn_2S_3 and SnO_2 among the other. It does not seem that a recrystallization process of the SnS occurred, but after the treatment the sample resulted heavily damaged, characterized by macroscopic holes, and the surface colour from grey turned to black in some region and orange in other (it is not homogeneously distributed). The presence of the diffraction peaks of Sn_2S_3 and other compounds of Zn, In, Sn, S, O suggests that a strong intermixing of the layers happened also to this sample.

In the case of the $SnCl_2$ treatments, the samples exhibit the main diffraction peaks of orthorhombic SnS. A slight modification of the relative intensities of XRD peaks is also visible, the preferential orientation is reduced, and this behaviour confirms the morphological analysis. This effect is similar to the re-orientation of the CdTe grains after applying $CdCl_2$ treatment.

5.2.2.4 PDTs effects on SnS solar device performance

All the samples treated with the KI “wet” treatment resulted damaged to the point that no device could be measured.

In Fig. 5.18, the J-V characteristic of the as-deposited sample best cell is compared to the sample best cell after the $SnCl_2$ PDT. The sample was deposited at T_{sub} = 400 °C, and the as-deposited performance is coherent with the sample deposited at high substrate temperature discussed in the Section 4.3. The slight decrease in this case is most probably due to the T_{sub} value, which is slightly different, and more important, this sample was deposited before the cleaning of the deposition apparatus discussed at the end of Section 3.2.

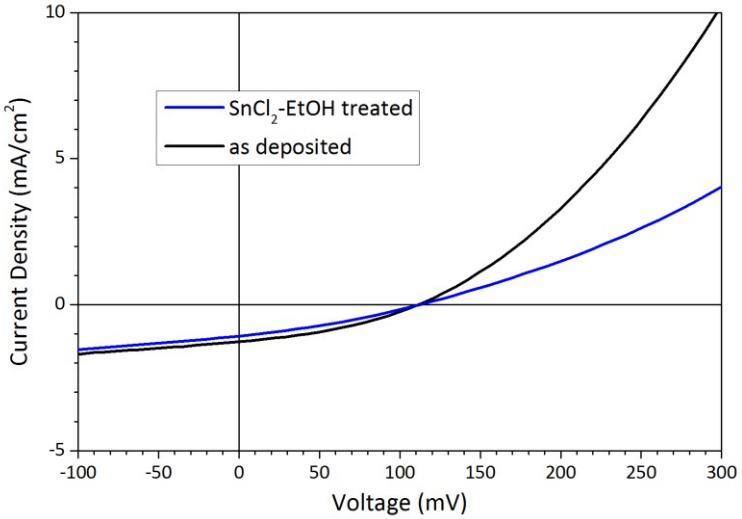

Fig. 5.18: J-V characteristic of the as deposited sample (black) compared with the treated one (blue).

The treated sample shows a slight degradation of the performance due to the PDT. The parameter (see Table 5.4) which mostly suffered from the treatment seems to be the F.F., indicating again a degradation of the junction rectifying ability after the thermal treatment.

Table 5.4: The working parameters of the as deposited solar cell compared with the one treated with .

	η [%]	F.F. [%]	V_{OC} [mV]	J_{SC} [mA/cm²]	R_P [Ω·cm²]	R_S [Ω·cm²]
$SnCl_2$ treated	0.04	29.8	107	-1.3	126	52
as deposited	0.06	35.3	114	-1.4	176	33

5.3 Conclusion

Several post-deposition treatments were applied to the SnS thin film solar cells and the results discussed.

It has been shown that the annealing of the CdS/SnS stack resulted in a reduction of the performance of the junction. To favour the SnS re-crystallization, we tested an annealing in inert atmosphere at a higher temperature, and the beginning of the re-crystallization process of the SnS has been achieved, but this PDT gave a result similar to the previous one for the device performance. Thus, we tried to reduce the annealing temperature and to aid the recrystallization process by adding a chlorine containing gas, Freon® R-22, which has been successfully applied to the CdTe case. Probably due to the low treating temperature, the PDT was non-effective. Also in this case, the cell performance resulted degraded due to the thermal annealing.

Then we looked to the well-known $CdCl_2$ treatment, widely applied to activate CdTe solar devices. Recrystallization of SnS thin films was achieved in the case with $CdCl_2$ "wet" treatment, but grain size resulted reduced. Furthermore, a strong layer intermixing affected the samples, indicating that the SnS hardly bears "violent" PDT.

To find an alternative to $CdCl_2$, the KI and $SnCl_2$ PDTs were developed. By applying the KI and $SnCl_2$ "wet" treatments we obtained for both worse results than the $CdCl_2$ case. We found that the treatment was too intense, and thus we moved to reduce its effects. Moreover, we found that the application of the same treatment over samples grown at different substrate temperatures gives different results. Samples deposited at T_{sub} = 400 °C can carry the PDTs, whereas those deposited at T_{sub} = 270 °C cannot, i.e. it seems that there is a correlation between treatments and the way in which samples are prepared. Samples grown at low substrate temperatures (270 °C) suffered a decrease of crystalline quality and phase purity until the formation of compounds where the underlying layers are mixed together with the SnS layer. Samples grown at high substrate temperature (400 °C) are instead more stable, and the treatments did not affect them in that detrimental way. Re-crystallization of samples happened with both KI and $SnCl_2$, but only in the latter PDT case samples were not irremediably damaged.

These results suggest that the re-crystallization and improvement of the grain quality with KI and $SnCl_2$ is achievable.

Finally, the degradation of the sample performance was a typical result of the treatment application. If the junction resulted damaged because of the thermal treatment, this could explain the phenomenon. It would be interesting to investigate the possibility to apply these PDTs on samples deposited in substrate configuration – i.e. before the buffer layer deposition – since it would lead to different results, not necessary the device performance degradation. In this way, one can treat SnS without the necessity to be conservative with respect the p-n junction, and thus it remains "only" to find the right PDT parameters and to ensure that the buffer layer will be deposited on the right layer, not on residues or oxidized layer. As seen, most of the works presenting the best performing SnS solar device adopt this configuration[16,32,33].

Chapter 6.

MODIFICATIONS TO THE SOLAR CELL STACK

In Chapter 4 the standard SnS based solar cell has been discussed. The absorber layer is deposited by thermal evaporation in vacuum on the following substrate stack: glass/ITO/ZnO/CdS. The CdS buffer layer is 50 nm-thick, and before the SnS deposition it undergoes an annealing treatment at 450 °C. Once the SnS deposition is completed, the device is completed by the deposition of a 50 nm-thick layer of Au, which is the back contact. In this chapter, few modifications to the stack will be discussed.

Our solar devices are deposited in superstrate configuration, and thus the front contact and the buffer layer play an important role. In fact, photons must travel inside the front contact and the buffer layer before their reach the absorber layer, where the absorption process can take place, and the photo-generated carriers could be separated before their recombination and supplying an external load. The absorption processes at the front contact and most of those at the buffer layer lead to photon losses, thus the transparency of these layers is an important parameter.

In our standard device, we use an ITO/ZnO bilayer as front contact, however indium is a rare element, and thus on industrial scale is too expensive. Thus, to reduce the solar module price ITO should be avoided as front contact despite its good properties, and

alternative transparent conductive oxides are now under development. We substituted the ITO/ZnO bilayer with a commercial FTO coated glass (NSG TEC™ C15).

We will discuss the optimization of the CdS buffer layer thickness for improving the CdS/SnS heterojunction. Moreover, it has been pointed out that since the CdS/SnS heterojunction forms a type II heterojunction, it is not ideal for SnS based solar device[17,58]. Thus, we investigated the substitution of the CdS buffer layer in favour of a ZnS layer – the ZnS/SnS heterojunction. Finally, we studied the n-type SnS/p-type SnS homojunction deposition on top of the CdS layer to improve the performance by reducing the defects concentration.

Finally, the standard back contact of the CdTe-based solar cells – the Cu/Au bilayer[73] – will be applied to our SnS solar devices, and the results will be compared to those of our standard back contact. Furthermore, the Cu diffusion inside CdTe is a well-known phenomenon, which can be promoted by annealing the back contact. The effects of this treatment to the Cu/Au back contact on SnS solar cells will be discussed.

In Section 4.2 a limited reproducibility of the SnS devices performance has been discussed, whereas in Section 4.3 a precise set of procedures has been applied to achieve comparability among the obtained results. These procedures were not applied in the experiments, which will be described in this chapter, in other words, this means that the sample performance cannot be compared with the results reported in Chapter 4. Thus, to guarantee the reliability of the comparisons between a sample and its reference, their SnS absorber layer has been deposited during the same deposition process, if not differently indicated.

6.1 Front contact layer

In this section, we will discuss the results of the substitution of the ITO/ZnO bilayer front contact with the commercial product NSG TEC™ C15 a FTO coated glass.

In Fig. 6.1 the transmittance of the standard glass/ITO/ZnO front contact is compared to the commercial NSG TEC™ C15 one (glass/FTO) is shown. The interference pattern of both spectra, is due to the presence of multiple interfaces in the two samples. The commercial product exhibits a higher transmittance in the 300÷370 nm range, whereas in the remaining part of the spectrum the results are comparable. The absorption in the 300÷370 nm region in the case of ITO/ZnO is mostly due to the absorption of the ZnO layer.

The average transmittance in the visible part of the spectrum (wavelengths in 400÷800 nm range) is 77 % for the glass/ITO/ZnO case and 80 % in the glass/FTO one.

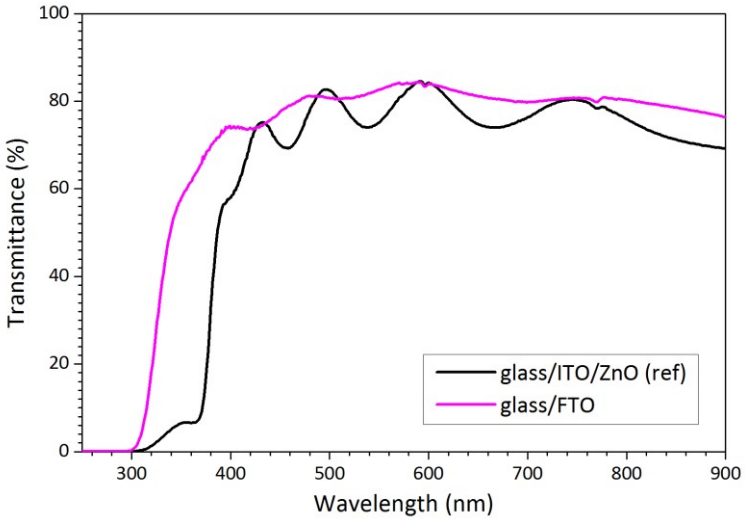

Fig. 6.1: The transmittance of the glass/ITO/ZnO substrate (black) compared to the glass/FTO one (magenta).

These two TCOs were used as substrates. The standard procedure discussed in Chapter 2 has been applied. The TCOs were annealed before the deposition of the 50 nm-thick CdS layer (deposited by thermal evaporation); after the deposition, the samples were annealed on their turn. Then, the deposition of the SnS layer and of the Au back contact layer completes the device. In this case, the 2 µm-thick SnS absorber layer has been deposited at T_{sub} = 270 °C, with a deposition rate of 0.5 nm/s.

In Fig. 6.2 the morphologies of the SnS thin films grown on the two substrates are shown.

Both samples exhibit the lamellar structure seen in Fig. 4.3 (but for lower T_{sub} = 250 °C), and the same inhomogeneous grain size distribution seen in Fig. 4.15 (at the same T_{sub} = 270 °C): there are small grain of hundreds of nm together with big grains of more than one µm.

Since Fig. 6.2-b seems to be affected by the double tip artefact, it is not possible to describe the morphology with no doubts. However, it seems that the main difference between Fig. 6.2-a and Fig. 6.2-b lies in a different microstructure complexity. The sample grown on the glass/FTO/CdS stack seems to be characterized by the presence of “small grains” smaller than those of the other case, and similarly for the big layered grains, where their constituent structures are smaller.

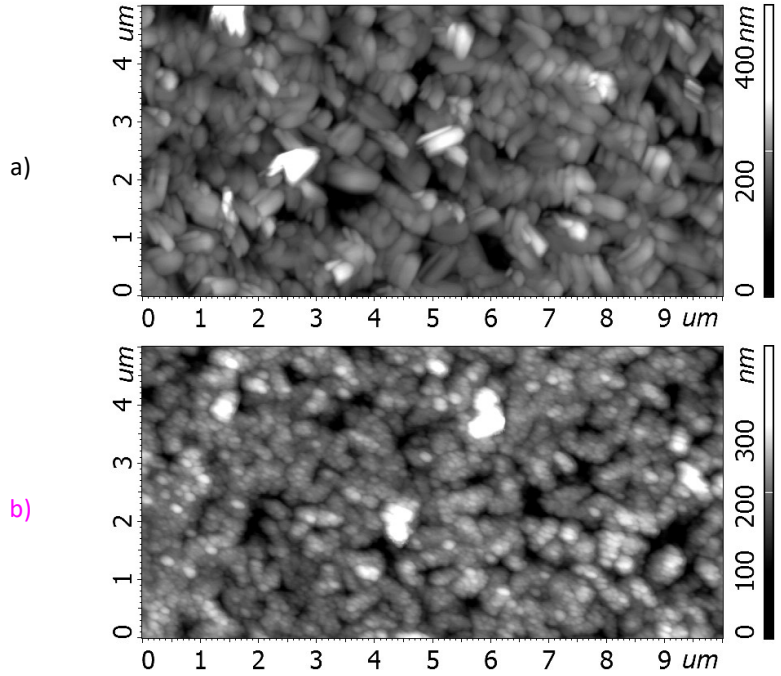

Fig. 6.2: The morphology of the SnS layer deposited on the a) standard glass/ITO/ZnO/CdS stack and on the b) glass/FTO/CdS one.

The x-ray diffraction patterns of these samples are shown in Fig. 6.3: they are very similar and both showed the main reflections of orthorhombic SnS, but some differences can be found.

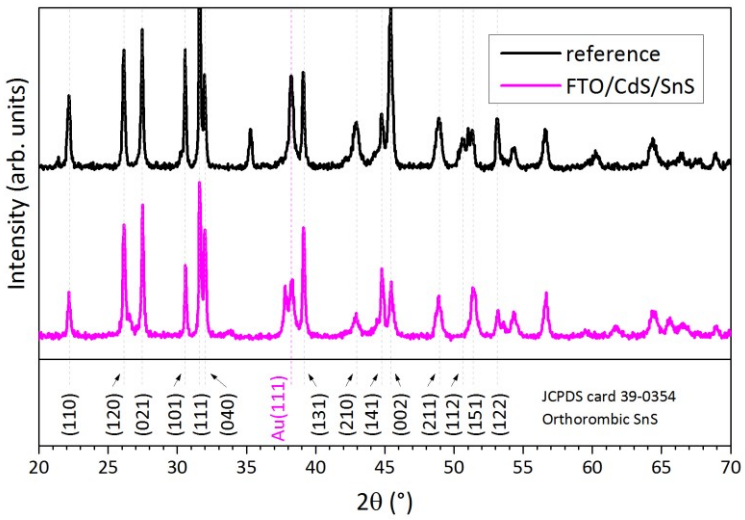

Fig. 6.3: The XRD patterns of the sample with the ITO/ZnO (black), and the FTO (magenta) front contact.

The first difference is the peak at $2\theta \approx 35.5$ °, which, as seen in Section 4.2 can be attributed to the ITO layer. In the FTO case this reflection disappears. The second difference is a slight change in the peaks relative intensity: since the two samples were prepared during the same deposition, the difference may be imputed to the different

substrate. The last difference is the presence of two peaks at $2\theta \approx 26.5$ ° and $2\theta \approx 37.8$ ° in the sample with FTO, which indicate the presence of the Sn_2S_3 impurity phase in the sample with FTO.

Despite these differences, the sample XRD patterns are in good agreement with those of Fig. 4.16 for samples grown at the same substrate temperature.

These samples were also measured by Raman spectroscopy. A representative of the Raman measurements performed on several regions of the samples are shown in Fig. 6.4.

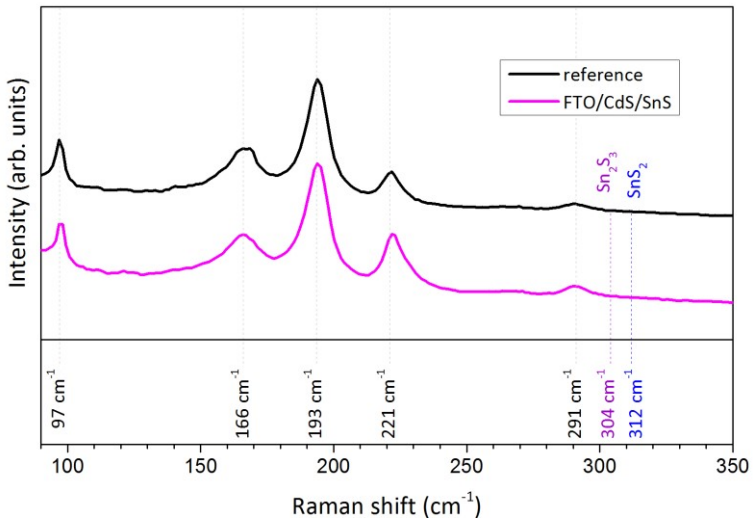

Fig. 6.4: Raman spectra of the samples with the ITO/ZnO (black), and the FTO (magenta) front contact.

The Raman spectra of the two samples are very similar, and in good agreement with those of Section 4.3. The main SnS vibration modes are present, and the relative intensities are very similar to those depicted in Fig. 4.17 for the same T_{sub} value.

Despite the XRD pattern of the FTO sample demonstrated the presence of Sn_2S_3, none of the Raman measurements on this sample confirms this result. We could find two possible explanations for this phenomenon. One case could be that the inhomogeneity of the sample would give unreliable measurements if a not sufficiently high number of Raman measurements are made. Another case might be that the Sn_2S_3 impurity phases would lie in the SnS bulk and Raman spectroscopy could not detect them. We cannot exclude any of these two possibilities.

In Fig. 6.5 are shown the J-V characteristic of the best device with the ITO/ZnO front contact and of the best device with the FTO front contact; the cell parameters are listed in Table 6.1.

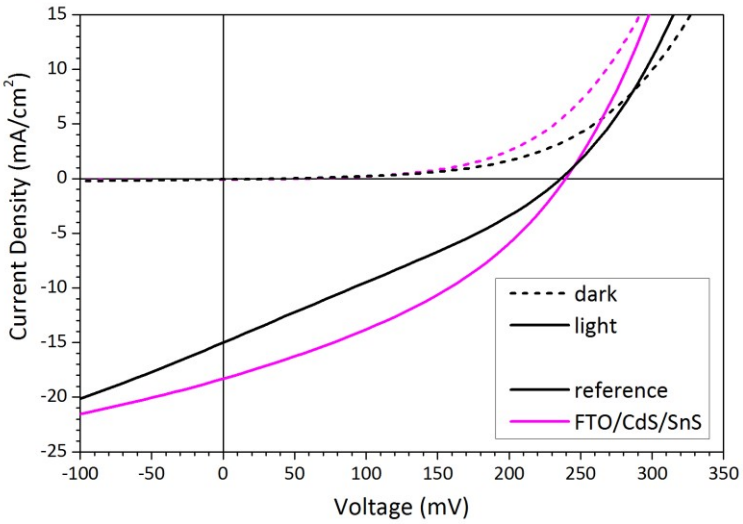

Fig. 6.5: J-V characteristic of the best device under dark (dashed line), and under light (black line).

The sample grown on the standard ITO/ZnO front contact – the reference – exhibits a best power conversion efficiency η = 1.03 %, while the one grown on the FTO front contact shows an improved performance with a best power conversion efficiency of η = 1.59 %.

From Table 6.1, we can observe that the performance difference is not due to the V_{OC}, which is similar for the two samples. The parameters exhibiting the main difference are J_{SC} and the parallel and series resistances. The short circuit current density results improved of about 20 % in the FTO case, and both the resistances values improve (R_P increases, R_S decreases). This difference is even more evident by looking to the shape of J-V characteristic of the ITO/ZnO case.

Table 6.1: The working parameters of the solar cell using the ITO/ZnO and the FTO front contact.

	η [%]	F.F. [%]	V_{OC} [mV]	J_{SC} [mA/cm²]	R_P [Ω·cm²]	R_S [Ω·cm²]
reference	0.98 ± 0.04	28.6 ± 0.4	240 ± 1	-14.3 ± 0.5	19 ± 1	9 ± 1
FTO/CdS/SnS/Au	1.39 ± 0.15	33.8 ± 1.8	233 ± 9	-17.7 ± 0.9	24 ± 3	6 ± 1

Despite the XRD pattern pointed out the presence of the Sn_2S_3 impurity phase in the FTO sample, this device exhibited the best performance ever achieved in our laboratory for SnS based solar devices. From the comparison of the FTO sample with the one discussed in Section 4.1 – the best SnS based device produced with the glass/ITO/ZnO/CdS/SnS/Au stack – we found that these samples have a very similar performance (see Table 6.2). However, we are aware that the sample of Section 4.1 has

been grown at a different T_{sub} value (T_{sub} = 250 °C), and the comparison is possible since all these samples were deposited during the "2nd deposition process" of the SnS raw material.

Table 6.2: The working parameters of the best solar cell using the ITO/ZnO and the FTO front contacts compared with the best device discussed in Section 4.1 (Sec. 4.1 ref.).

	T_{sub} [°C]	η [%]	F.F. [%]	V_{OC} [mV]	J_{SC} [mA/cm²]	R_P [Ω·cm²]	R_S [Ω·cm²]
reference	270	1.03	29.3	240	-14.6	19	8
FTO/CdS/SnS/Au	270	1.59	36.3	240	-18.3	26	5
Sec. 4.1 ref.	250	1.51	34.0	226	-19.6	21	5

6.2 Buffer layer

6.2.1 CdS buffer layer optimization

In this section, we will present the results of the study on the CdS buffer layer optimization. Several CdS layers with different thickness (0, 30, 50, 100, 150 nm) were deposited on glass/ITO/ZnO substrates after their annealing in vacuum (30 minutes at 450 °C). After the deposition of the CdS layer and the consequent annealing of the stack (30 minutes at 450 °C), the transmittance of the CdS thin films was measured. The SnS layer is deposited with the same parameters for all the samples: 2 µm-thick layers were deposited at a substrate temperature T_{sub} = 250 °C and a deposition rate of about 0.5 nm/s. Samples were deposited during the 2nd deposition process of as-bought raw material – i.e. the raw material underwent one sublimation/condensation cycle before the deposition of the sample – of different crucible refills.

The sample grown on the 50 nm-thick CdS layer is the same sample discussed in Section 4.1.

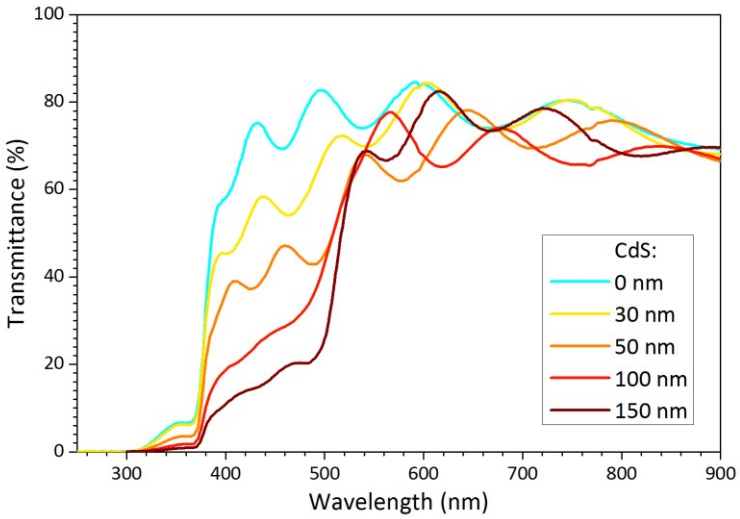

Fig. 6.6: The transmittance of the glass/ITO/ZnO/CdS stacks where the CdS layer is deposited with different thicknesses.

Fig. 6.6 shows the transmittance of the different thick CdS layers. Increasing CdS thickness, its absorption in the 300÷500 nm wavelength range increases strongly, whereas at higher wavelengths it remains almost transparent, and absorption is caused by the underlying layers. Also in this case the interference pattern is caused by the presence of multiple interfaces between the layers constituting the stack.

The morphologies of the SnS layers deposited over these substrates is shown in Fig. 6.7. Also in this case, the SnS morphologies exhibit both the lamellar structure and the grain size distribution inhomogeneity seen for films deposited at similar substrate temperature value (in this case T_{sub} = 250 °C). In fact, it is possible to find big grains which size exceed one µm, and it is clearly possible to see their own morphology – these grains are constituted by many superimposed layers – and, at the same time, in other regions there are small grains of hundreds of nm.

It seems that no significant variation of the morphology occurs in the case of different CdS layer thicknesses.

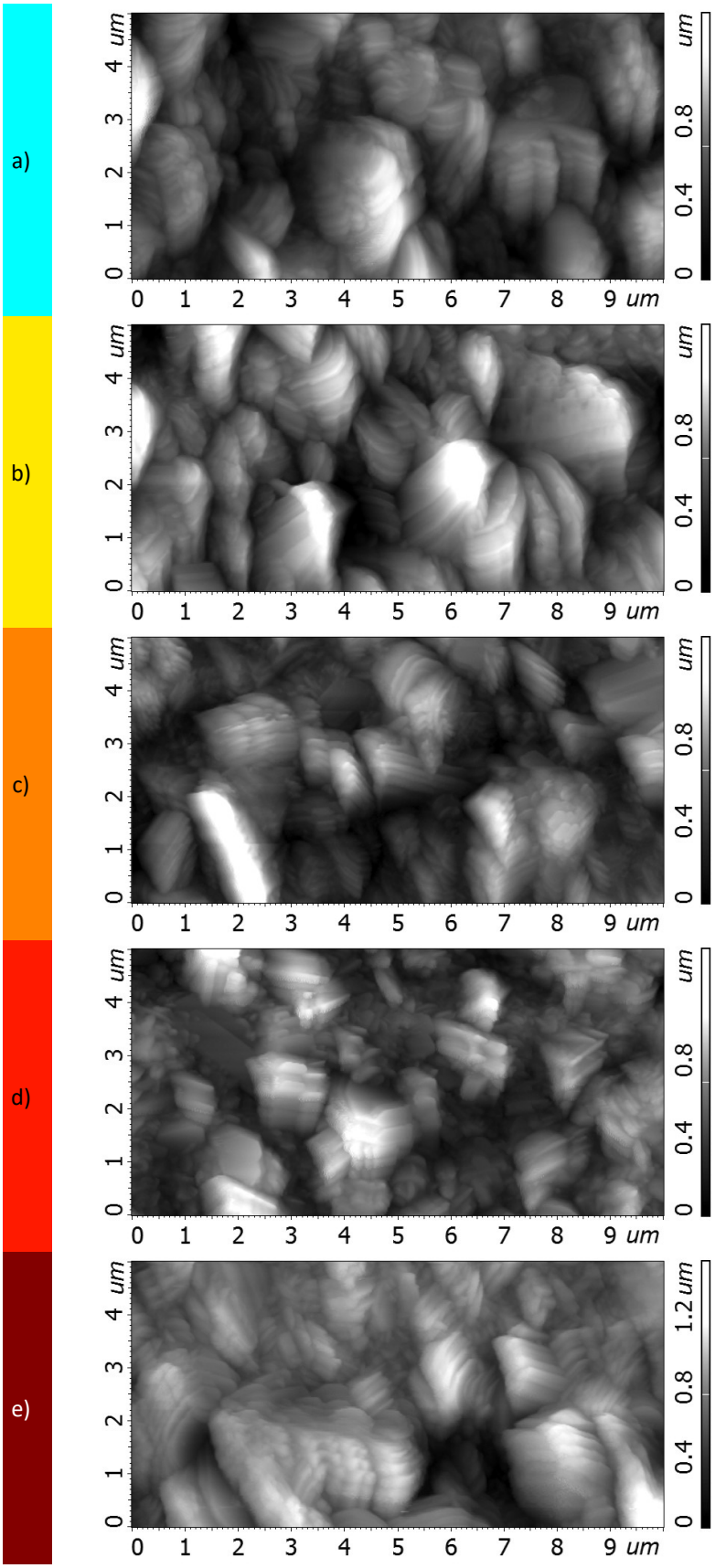

Fig. 6.7: The morphology of the 2 µm-thick SnS layer deposited on CdS buffer layer of different thickness: a) 0 nm, b) 30 nm, c) 50 nm, d) 100 nm and e) 150 nm.

The XRD spectra of these samples are shown in Fig. 6.8. Increasing the CdS layer thickness, the SnS exhibits a microcrystalline structure, which is more and more preferentially oriented. In the case where no CdS was deposited, there are many intense diffraction peaks, whereas, on the opposite, in the case with the thickest CdS layer, only three diffraction peaks dominate the spectrum. The peaks due to (101), (111) and (040) reflections become more and more intense increasing the CdS layer thickness. This indicates that the SnS growth is more and more influenced by the CdS layer presence. We can conclude that the SnS layer microstructure adapts to the substrate one.

Only in the case of the 150 nm-thick CdS an intense peak due to the Sn_2S_3 impurity phases ($2\theta \approx 26.2$ °) was observed. In the other cases, there are not so evident signs of its presence.

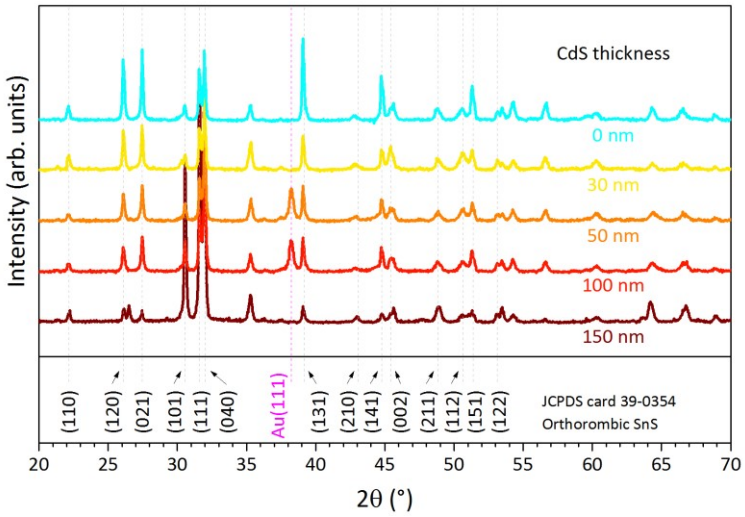

Fig. 6.8: XRD patterns of the SnS solar cell sample grown on CdS buffer layer with different thicknesses.

Finally, the solar device performances were measured, and in Fig. 6.9 the J-V characteristics of the best device for every sample are shown. The sample average performance parameters are listed in Table 6.3.

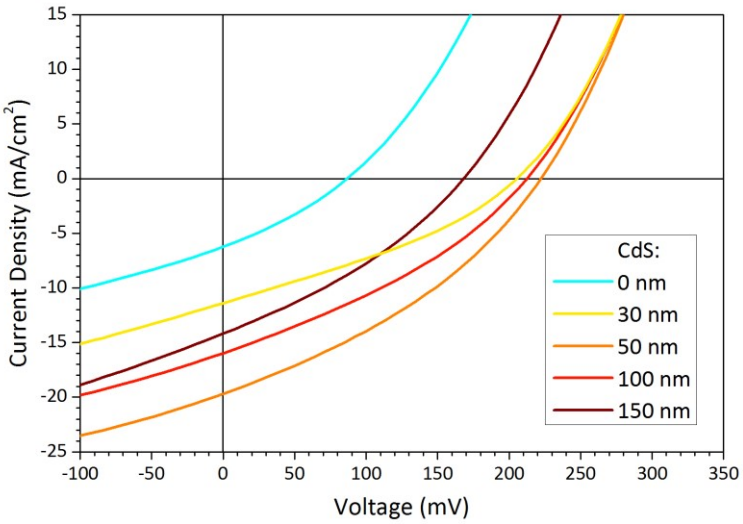

Fig. 6.9: J-V characteristic of the best device under dark (dashed line), and under light (black line).

In the case where no CdS were deposited, a ZnO/SnS heterojunction was formed. In this case, both V_{OC} and J_{SC} show poor performance. By adding a 30 nm-thick CdS layer both V_{OC} and J_{SC} were doubled. These results are in good agreement with those of Schneikart *et al.*[31].

A further increment of the CdS layer thickness to 50 nm resulted in the best performance (Section 4.1). Any further increase of the CdS thickness reduced the power conversion efficiency η. For the 100 nm-thick CdS case, we found a slight reduction of V_{OC} and J_{SC}, but the performance is higher than the one of the case of 30 nm-thick CdS layer. Finally, for the 150 nm-thick CdS, the performance is comparable with the 30 nm-thick case: the strong reduction of V_{OC} is compensated by an increase of J_{SC}. In all cases F.F. is about 30 %.

Table 6.3: The working parameters of the solar cells deposited on CdS layers of different thickness.

CdS thickness [nm]	η [%]	F.F. [%]	V_{OC} [mV]	J_{SC} [mA/cm²]	R_P [Ω·cm²]	R_S [Ω·cm²]
0	0.14 ± 0.02	28.6 ± 0.8	85 ± 5	-5.6 ± 0.5	20 ± 2	9 ± 1
30	0.67 ± 0.07	32.2 ± 0.4	209 ± 7	-9.9 ± 1.3	30 ± 5	9 ± 1
50	1.23 ± 0.22	32.8 ± 1.2	227 ± 2	-16.4 ± 2.6	24 ± 2	7 ± 2
100	0.99 ± 0.10	32.4 ± 0.5	213 ± 3	-14.4 ± 1.3	23 ± 1	7 ± 1
150	0.62 ± 0.09	30.7 ± 1.4	159 ± 10	-12.6 ± 1.1	19 ± 3	7 ± 1

Since the best performance has been achieved with the 50 nm-thick CdS, we chose this value as our standard CdS buffer layer thickness.

6.2.2 ZnS buffer layer

The CdS/SnS heterojunction is a type II heterojunction, with a conduction band discontinuity of 0.4 eV[17] which is not ideal for solar devices since it increases the current losses due to charge carriers recombination. In Section 6.2 we already studied the properties of the ZnO/SnS heterojunction. Its performance was poor compared with the optimized 50 nm-thick CdS layer. The presence of the CdS layer increased both V_{OC} and J_{SC} allowing to reach a power conversion efficiency about ten times greater than the ZnO case. In this section, we will investigate an alternative buffer layer, ZnS, which has been successfully used with other absorbers[74].

We deposited the standard SnS thin film (2 µm-thick, T_{sub} = 270 °C, 0.5 nm/s) on two different substrates. One is our reference sample – the substrate was a glass/ITO/ZnO/CdS stack – and in the other one, the CdS layer has been replaced with the ZnS one. The ZnS has been deposited on a commercial NSG TEC™ C15 substrate by sputter deposition at the university of Milano-Bicocca and stored in vacuum until its usage. The ZnS layer deposition parameters are unknown.

In Fig. 6.10, the transmittance of our reference sample (the glass/FTO/CdS stack with a 50 nm-thick CdS layer) is compared to the ZnS one. In the visible part of the light spectrum (we considered the wavelength range 400÷800 nm) the transmittance of our reference is T ≈ 60 %, whereas the ZnS coated sample exhibited a higher value T = 75 %. This difference can be ascribed to the different buffer layer, since the CdS has a bandgap of E_g = 2.4 eV while ZnS has an energy bandgap of E_g = 3.5 eV – in other words, CdS absorbs light of all wavelengths below ≈ 520 nm, whereas ZnS of all the wavelengths below ≈ 350 nm: ZnS is transparent in the visible region of the spectrum. The different transmittance above 520 nm could be due to the different refractive index of the two materials, which in the case of CdS seems to increase the losses due to the reflection at the FTO/CdS and CdS/air interfaces.

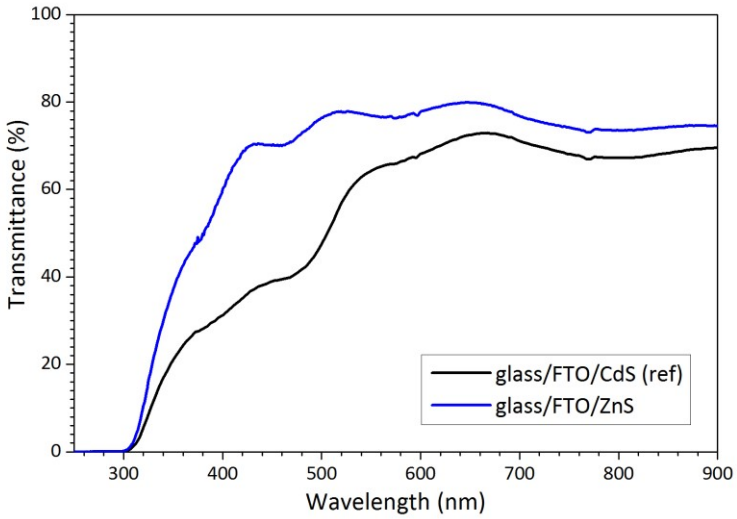

Fig. 6.10: The transmittance of the glass/FTO/CdS stacks compared with the glass/FTO/ZnS one.

Standard SnS thin films were deposited on the two substrates during the same deposition process. In Fig. 6.11 the AFM images describing the sample surface morphologies are shown.

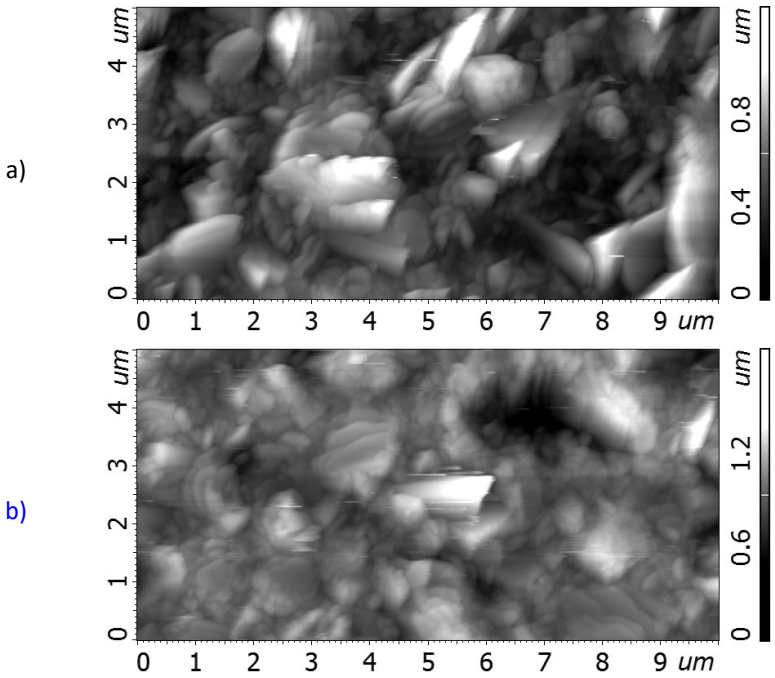

Fig. 6.11: The morphology of the SnS layer deposited on the a) glass/FTO/CdS stack and on the b) glass/FTO/ZnS one.

Also in this case the samples exhibit both the layered nature of SnS and the grain size distribution inhomogeneity, where small grains stand together with big grains. In the reference case, we can see that the small grain size is about 500 nm whereas the big grain size exceeds one µm. In the case of the sample grown on the ZnS layer, it seems that the

small grain size is reduced to about 200 nm while the big agglomerate of grains has a reduced size which hardly exceeds the µm. The ZnS sample seems thus to have a more complex morphology.

In Fig. 6.12 the XRD spectra of the two samples are shown. Both exhibit the main diffraction peak of orthorhombic SnS, and both exhibit also the peaks at $2\theta \approx 26.5$ and $2\theta \approx 37.8$: the impurity phase Sn_2S_3 is present in both the samples. From the comparison of the two XRD patterns, only a slight variation of the peak relative intensities can be found.

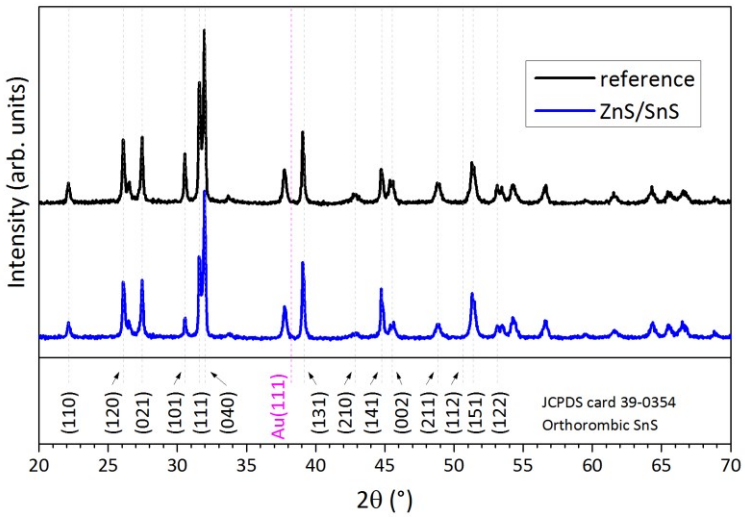

Fig. 6.12: XRD patterns of the SnS solar cell sample grown on CdS buffer layer with different thicknesses.

The J-V characteristics of the best solar cell of the two samples are shown in Fig. 6.13, and the working parameters of the device are summarized in Table 6.4. Since the ZnS/SnS solar cell showed a very poor performance, to demonstrate its non-ohmic behaviour, its J-V characteristic is shown in the inset of Fig. 6.13 in a more suitable current density range.

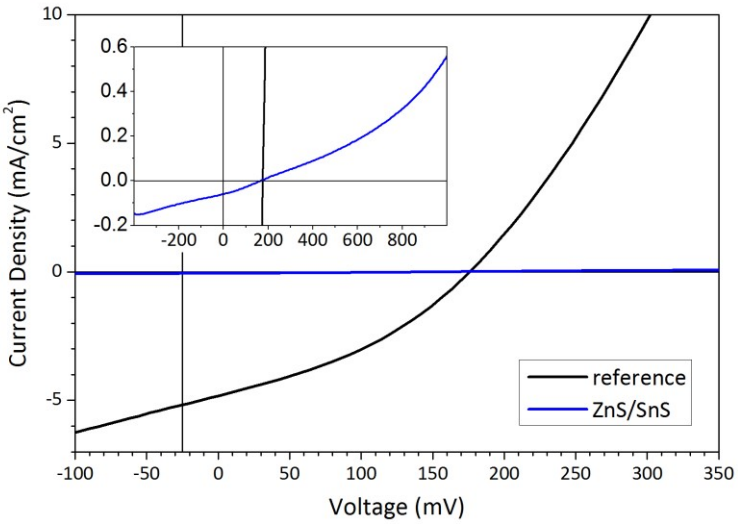

Fig. 6.13: J-V characteristic of the (black) CdS/SnS heterojunction reference sample compared to the (blue) ZnS/SnS one. The inset shows the same J-V curves on a more suitable current density scale.

It is interesting to observe that the reason for the very poor performance for the sample with the ZnS buffer layer is the absence of J_{SC}, whereas V_{OC} shows a good value although it is not ideal.

Also the reference cell shows a poor performance compared to others showed in this thesis, but this behaviour could be explained with the argumentations discussed in Section 4.2 relatively the performance irreproducibility.

Table 6.4: The working parameters of the CdS/SnS reference sample compared to the ZnS/SnS one.

	η [%]	F.F. [%]	V_{OC} [mV]	J_{SC} [mA/cm²]	R_P [Ω·cm²]	R_S [Ω·cm²]
reference	0.25 ± 0.03	33.6 ± 1.0	169 ± 8	-4.4 ± 0.3	69 ± 8	20 ± 1
FTO/ZnS/SnS/Au	0.00 ± 0.01	28.0 ± 0.4	125 ± 32	-0.1 ± 0.1	>1000	>1000

All the sample fabricated on the ZnS layer deposited at Milano-Bicocca university showed the same result.

6.2.3 CdS/n-SnS buffer layer

Compared to a homojunction, a heterojunction generally introduces additional defect states. An example of this are the defect states introduced by simply growing the SnS layer on the CdS layer because of the CdS/SnS lattice mismatch.

Thus, to reduce this contribution, which limits the CdS/SnS solar cell performance, we tried to add a thin layer of n-type SnS between the n-type CdS and the p-type SnS

layers. In this way we wanted to create a more efficient SnS homojunction similarly to what happens in the CIGS case[75].

SnS generally shows p-type conductivity due to the acceptor behaviour of tin vacancies[46]. Ristov *et al.*[51] demonstrated the feasibility of turning its intrinsic p-type conduction into n-type conduction by simply annealing the SnS film in air at the proper treatment temperature.

We deposited SnS layers on glass substrates to investigate the annealing effects on SnS conductivity. The conductivity of samples has been verified by Seebeck effect measurements of annealed samples at different temperature. We found that a single annealing of 60 minutes at 450 °C was the proper combination to obtain n-type conductivity.

Thereafter, we deposited over two glass/FTO/CdS stack substrates a thin layer of SnS. The CdS layer thickness was 50 nm, and has been annealed in vacuum after its deposition. The 400 nm-thick SnS layers have been deposited at a substrate temperature T_{sub} = 270 °C and at a deposition rate of 0.5 nm/s during the same deposition process. One of the samples was then annealed in air for turning its conductivity to the n-type one, while the other one was conserved in vacuum during this process. The following step was the deposition of the 2 µm-thick SnS absorber layer on top of these two sample, and on a third one – the third sample was deposited on the same substrate of the other two (glass/FTO/CdS) but without the thin SnS layer: this sample will be our reference. Also this SnS layer has been deposited at T_{sub} = 270 °C, and a deposition rate of 0.5 nm/s. The samples were than completed with the deposition of the Au back contact.

Their J-V characteristic was then measured, and the results are shown in Fig. 6.14; the working parameters are listed in Table 6.5.

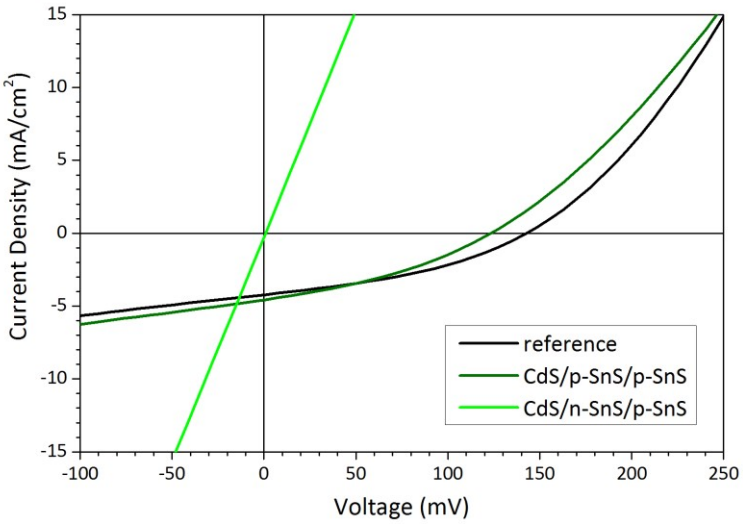

Fig. 6.14: J-V characteristics of the reference device (black), the CdS/p-type SnS double layer (dark green), and the CdS/n-type SnS/p-type SnS layer (green).

The J-V characteristics of all the devices with the SnS p-n homojunction show only ohmic behaviour. The reference sample and the one with the double p-type SnS layer exhibit a similar performance, i.e. a power conversion efficiency of about $\eta \approx 0.2$ %. The reference sample shows a slightly better performance: a better F.F. and V_{OC}, but a poor J_{SC} compared to the other sample. On the other side, the sample with the double SnS layer shows a slight improved J_{SC} despite its series resistance increased.

Likewise the previous section, the reference cell shows a poor performance compared to others cases, and this behaviour could be explained with the same arguments about performance irreproducibility discussed in Section 4.2.

Table 6.5: The working parameters of the reference device, of the CdS/p-type SnS double layer, and of the CdS/n-type SnS/p-type SnS layer.

	η [%]	F.F. [%]	V_{OC} [mV]	J_{SC} [mA/cm²]	R_P [Ω·cm²]	R_S [Ω·cm²]
reference	0.21 ± 0.01	37.1 ± 0.8	147 ± 3	-3.8 ± 0.2	81 ± 6	14 ± 1
CdS/p-SnS/p-SnS	0.18 ± 0.01	33.3 ± 0.9	123 ± 3	-4.4 ± 0.2	51 ± 4	14 ± 1
CdS/n-SnS/p-SnS	*all samples exhibit ohmic behaviour*					

The experiment has been repeated, but a thinner n-type SnS layer (100 nm) has been used. Also in this case the same results were obtained.

Most probably, the ohmic behaviour of the SnS p-n homojunction sample, is caused by the thermal annealing which turn the SnS conductivity. As seen in Chapter 5, any thermal annealing applied to SnS samples have had detrimental effects on the CdS/SnS junction. It would be very interesting to explore this approach for SnS based solar cells

deposited in substrate configuration, i.e. without the limitations of applying thermal treating on samples with an already formed instable junction.

6.3 Back contact layer

The variation of the performance of SnS solar cells due to a different back contact (BC) was then investigated. In the CdTe case, due to its high work function, it is difficult to create a good ohmic contact. Typically, after the $CdCl_2$ activation treatment and the consequent etching, a Te rich layer results on the surface of the CdTe layer. The deposition of the standard Cu/Au layer complete the device. Cu is known to act as a dopant for CdTe and to improve its performance[76]. Moreover, Cu easily diffuses inside CdTe and the stack annealing – the back contact annealing – promotes this diffusion process.

In our case, the standard back contact for SnS solar devices is the 50 nm-thick Au layer. Schneikart *et al.*[31] demonstrated that Au forms an ohmic contact on SnS, and thus that is a good back contact for this technology. However, we decided to compare the standard Au back contact with the Cu/Au back contact.

The samples were deposited over the glass/FTO/CdS stacks. A 2 µm-thick SnS layer has been deposited by thermal evaporation at T_{sub} = 270 °C, and at a rate of 0.5 nm/s. The reference sample was completed with the standard 50 nm-thick Au layer, whereas the other one with a 2 nm-thick Cu layer on top of which another Au layer (50 nm-thick) has been deposited.

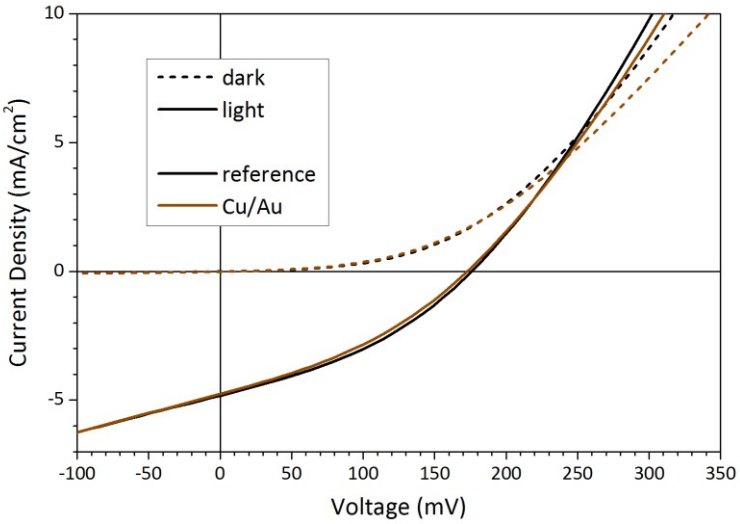

Fig. 6.15: J-V characteristic of the sample with the standard Au back contact (black) compared to the sample with the Cu/Au one (brown).

In Fig. 6.15 the J-V characteristics of the sample with the Au back contact (black) and with the Cu/Au back contact (brown) are shown. From the analysis of the working parameters of the two devices (Table 6.6), we can conclude that their performances are equivalent. The one with the Cu/Au back contact exhibits a slight worsened F.F. and parallel and series resistances.

Table 6.6: The working parameters of the solar cell using the ITO/ZnO and the FTO front contact.

	η [%]	F.F. [%]	V_{OC} [mV]	J_{SC} [mA/cm²]	R_P [Ω·cm²]	R_S [Ω·cm²]
reference	0.25 ± 0.03	33.6 ± 1.0	169 ± 8	-4.4 ± 0.3	69 ± 8	20 ± 1
Cu/Au BC	0.24 ± 0.02	32.5 ± 0.9	171 ± 3	-4.4 ± 0.2	65 ± 3	22 ± 2

As in the previous cases, the reference itself showed a poor performance; also in this case this is due to the performance irreproducibility discussed in Section 4.2. Thus, only the comparison between the sample deposited during the same SnS deposition is meaningful, and so these results could be considered only qualitative when compared with the performance of other samples.

Finally, the samples with the Cu/Au back contact were submitted to a series of thermal annealing in air, with the treatment temperatures increasing at every step. The thermal treatment has the purpose of promoting Cu diffusion inside SnS, and thus we want to correlate the SnS solar cell performance to this parameter.

The thermal treatments lasted for 30 minutes with a temperature ramp time of 15 minutes. The first annealing was carried out at T_{tr} = 80 °C, and the following to a treatment temperature T_{tr} increased step by step of 20 °C.

The J-V characteristics modification due to the consequent annealing treatments are depicted in Fig. 6.16, while the solar cell parameters are listed in Table 6.7.

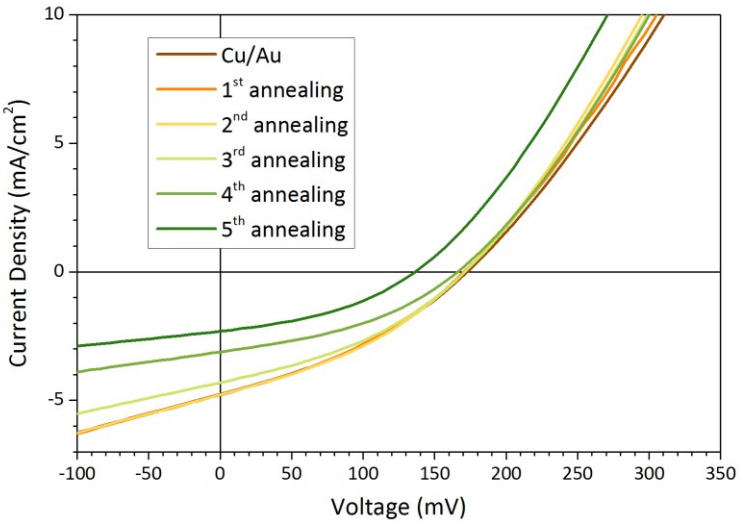

Fig. 6.16: Modifications to the J-V characteristic of the sample with the Cu/Au back contact due to the thermal treatments.

The first two annealing procedures resulted in a slight improvement of the sample performance. The improved parameters are mainly V_{OC} and F.F. (as well as R_P and R_S). The 3rd annealing treatment worsened the performance to the initial value; the following treatments worsened it to less than the half of the starting power conversion efficiency. The F.F. increased almost linearly by increasing the thermal treatment temperature, and similarly the parallel resistance R_P. Moreover, after the third annealing, the J_{SC} and V_{OC} values showed a significant drop.

Table 6.7: The working parameters of the sample with the Cu/Au back contact measured after the thermal annealing (ann.) at the T_{tr} temperature.

	T_{tr} [°C]	η [%]	F.F. [%]	V_{OC} [mV]	J_{SC} [mA/cm²]	R_P [Ω·cm²]	R_S [Ω·cm²]
Cu/Au BC	-	0.24 ± 0.02	32.5 ± 0.9	171 ± 3	-4.4 ± 0.2	65 ± 3	22 ± 2
1st ann.	80	0.25 ± 0.02	32.8 ± 0.6	171 ± 3	-4.5 ± 0.2	66 ± 2	21 ± 2
2nd ann.	100	0.26 ± 0.02	33.6 ± 0.4	173 ± 3	-4.5 ± 0.2	69 ± 3	20 ± 2
3rd ann.	120	0.23 ± 0.01	34.3 ± 0.9	171 ± 3	-3.9 ± 0.2	83 ± 6	22 ± 2
4th ann.	140	0.18 ± 0.01	36.9 ± 0.8	166 ± 3	-2.9 ± 0.1	126 ± 9	25 ± 2
5th ann.	160	0.11 ± 0.01	36.1 ± 0.7	136 ± 5	-2.2 ± 0.1	143 ± 15	28 ± 3

We can conclude that the Cu/Au and the simple Au back contact are equivalent in our case. The Cu diffusion inside SnS implicates only a slight improvement of the device performance. There is a threshold value over which Cu concentration inside SnS became detrimental.

6.4 Conclusion

In this chapter, we proposed, investigated and discussed some modifications to the standard SnS based solar cell as possible strategies to improve the device performance.

The standard SnS based solar cell is constituted by a ITO/ZnO bilayer as front contact, a CdS layer as buffer layer, the SnS absorber layer and the Au back contact layer. While in Chapter 4 and 5 we focused on the SnS absorber layer, in the present chapter we focused our attention to the other constituents one by one.

We have seen how the substitution of the ITO/ZnO front contact layer with the commercial FTO coated glass from NSG resulted in an increment of the cell performance, and in the best SnS based solar cell ever produced in our laboratory.

In Section 6.2 we showed the results about our study on the optimization of the CdS layer thickness. We demonstrated that the most suitable CdS thickness for improving the SnS solar cell performance is the 50 nm one. We also studied the possible CdS substitution with other semiconductor materials, since it is known that the CdS/SnS heterojunction suffers from a non-optimal band alignment. We investigated the ZnS/SnS heterojunction, but despite the samples showed a certain rectifying ability – thus a p-n junction was formed – its quality was very unsatisfactory: it was not possible to extract any current from the samples. Another investigated strategy consisted in adding a thin SnS layer with n-type conductivity between the n-CdS and the p-SnS absorber layer, to create an SnS homojunction in the SnS material; also in this case, we obtained unsatisfactory results: no junction was formed.

Finally, in the last section of the chapter, we applied to the SnS solar devices the Cu/Au back contact layer instead of the standard Au back contact. The Cu/Au back contact does not offer a real advantage than the standard Au back contact. We investigated also the Cu diffusion inside the SnS layer, by annealing the back contact to promote diffusion: we found that the performance resulted very slightly improved during the first thermal treatments, demonstrating a sort of stability, but once Cu diffuses inside SnS the performance suddenly drops.

CONCLUSION

In this work, tin sulphide (SnS) has been investigated as absorber layer material for thin film photovoltaic devices.

Tin sulphide has been chosen because of its abundance in nature, low cost, and absence of toxicity, whereas other absorber materials in the thin film photovoltaic field exhibited high performance, like CdTe and CIGS, but contain tellurium, indium, gallium, selenium which are rare materials and toxic elements such as cadmium and selenium. Moreover, SnS is characterized by properties suitable for light conversion applications, an energy bandgap close to the maximum efficiency of the Shockley-Queisser limit, a very high absorption coefficient, and an intrinsic p-type conductivity.

The experimental apparatus used in this work for depositing the SnS absorber layer by thermal evaporation, once its construction was completed, exhibited several limitations which have been overcome. Therefore, the main apparatus subsystems have been completely re-designed and re-built for the purpose of the present research activity.

We achieved a maximum power-conversion efficiency comparable to the best performing device based on the same p-n junction, the same configuration, and the same deposition method, published by Schneikart *et al.* – i.e. a CdS/SnS heterojunction deposited in superstrate configuration by thermal evaporation.

Since samples demonstrated poor reproducibility, we investigated the possible origin of this phenomenon. We found a correlation between the device performance and the raw material thermal history, and for this reason we studied the performance of SnS

devices deposited in two consecutive processes of the same raw material. Moreover, the investigation has been carried out at several substrate temperatures to study also the influence of this parameter on the SnS solar devices. As expected, the substrate temperature parameter strongly affected the SnS thin film morphology, crystalline structure and vibrational dynamic as well as the device performance, in agreement with several other works. Although the thermal history of the SnS raw material seems to have no influence on morphology, crystalline structure and vibrational dynamic, the device performance exhibited a dramatic change between the two sets of samples. We hypothesize that a main difference has thus to be enclosed near the junction region.

With the aim of improving the device performance, similarly to what happen with other technologies, several post-deposition treatments were applied to the SnS thin film solar cells.

Thermal annealing in vacuum were applied on our samples, but these treatments resulted only in damaging the device junction. To reach higher treating temperatures, and thus to favour SnS re-crystallization, thermal annealing in inert atmosphere were applied to our samples. We found the evidence of the beginning of the re-crystallization process of the SnS layer, while the device performance gave a result similar to the previous case. Finally, to reduce the annealing temperature and to help the recrystallization process, a chlorine containing gas, Freon® R-22, has been added to obtain a reactive atmosphere in the treating chamber. Probably the low treating temperatures did not allow reaching effective results.

We decided to apply the well-known $CdCl_2$ treatment (the CdTe "activation" treatment) to our samples. A certain re-organization of SnS crystals was achieved, but grain size resulted reduced. Furthermore, a strong intermixing between the buffer and the absorber layers affected the samples, indicating that the SnS hardly bears "violent" post-deposition treatments. The effects of the KI and $SnCl_2$ post deposition treatments on SnS were also investigated. First, we found that the application of the same treatment on samples grown at different substrate temperatures gives different results. Samples deposited at low substrate temperature cannot tolerate the treatments resulting in the strong intermixing of all the sample layers. Samples deposited at high substrate temperature are instead more stable. Re-crystallization of the samples took place with both KI and $SnCl_2$, but only in the latter case samples were not irremediably damaged.

These results suggest that the re-crystallization and improvement of the grain quality with KI and $SnCl_2$ is achievable. Future investigations can be carried on in this direction.

As a consequence of thermal treatments, sample performance resulted degraded. It would be interesting to investigate the application of these post-deposition treatments on samples deposited in substrate configuration. In this manner, the p-n junction will be formed after the treatment application. Thus, it would be possible to exclude the eventuality of damaging the CdS/SnS heterojunction during PDTs application of superstrate samples.

Finally, some modifications to our standard SnS-based solar cell were investigated as possible strategies to improve the device performance.

We showed that the substitution of the ITO/ZnO front contact layer with the commercial FTO coated glass from NSG resulted in the best SnS based solar cell ever produced in our laboratory. Moreover, the CdS layer thickness is an important parameter for the device performance, we showed that in our case the most suitable CdS thickness for improving the SnS solar cell performance is equal to 50 nm.

Since it is known that the CdS/SnS heterojunction suffers from a non-optimal band alignment, we studied the CdS substitution with other semiconductor materials. The ZnS as buffer layer was applied. In our case, despite the samples showed a certain rectifying ability, the ZnS/SnS heterojunction showed low efficiencies. The application of ZnS to our absorbers needs further investigation. Again, for improving the junction formation, a thin SnS layer with n-type conductivity was inserted between the n-CdS and the p-SnS absorber layer, to create a SnS homojunction in the SnS material. Although we were able to obtain SnS layers exhibiting n-type conductivity, no junctions were formed: probably the thermal annealing necessary to turn the SnS conductivity from p-type to n-type damaged the CdS/SnS junction.

A Cu/Au back contact layer instead of the standard Au back contact to the SnS solar devices was also applied. However, this back contact does not offer a real advantage with respect to the standard Au back contact. We investigated the effects of Cu diffusion (by thermal annealing) inside the SnS layer, and we found that the performance resulted very slightly improved during the first treatments, but once a threshold Cu concentration was reached inside SnS, the performance suddenly drops.

REFERENCES

1. International Energy Agency. *Key World Energy Statistics 2016*. (IEA, 2016). doi:10.1787/key_energ_stat-2016-en
2. Kaneka Corporation. World's Highest Conversion Efficiency of 26.33% Achieved in a Crystalline Silicon Solar Cell — A World First in a Practical Cell Size. (2016). Available at: http://www.kaneka.co.jp/kaneka-e/images/topics/1473811995/1473811995_101.pdf. (Accessed: 9th January 2017)
3. First Solar Incorporation. First Solar Achieves Yet Another Cell Conversion Efficiency World Record. (2016). Available at: http://investor.firstsolar.com/releasedetail.cfm?ReleaseID=956479. (Accessed: 9th January 2017)
4. Zentrum für Sonnenenergie- und Wasserstoff-Forschung Baden-Württemberg (ZSW). ZSW Sets New World Record for Thin-film Solar Cells. (2016). Available at: https://www.zsw-bw.de/en/newsroom/news/news-detail/news/detail/News/zsw-sets-new-world-record-for-thin-film-solar-cells.html. (Accessed: 9th January 2017)
5. H. Sai *et al.* Stabilized 14.0%-efficient triple-junction thin-film silicon solar cell. *Applied Physics Letters* **109,** 183506 (2016). doi:10.1063/1.4966996
6. M. A. Green. *Third Generation Photovoltaics*. **12,** (Springer Berlin Heidelberg, 2006). doi:10.1007/b137807
7. Sharp Corporation. Sharp Develops Concentrator Solar Cell with World's Highest Conversion Efficiency of 44.4%. (2013). Available at: http://www.sharp-world.com/corporate/news/130614.html. (Accessed: 9th January 2017)
8. Fraunhofer-Institut für Solare Energiesysteme ISE. New World Record For Solar Cell Efficiency At 46%. (2014). Available at: https://www.ise.fraunhofer.de/en/press-and-media/press-releases/press-releases-2014/new-world-record-for-solar-cell-efficiency-at-46-percent.
9. W. S. Yang *et al.* High-performance photovoltaic perovskite layers fabricated through intramolecular exchange. *Science* **348,** 1234–1237 (2015). doi:10.1126/science.aaa9272
10. R. Komiya *et al.* Improvement of the conversion efficiency of a monolithic type dye-sensitized solar cell module. in *Technical Digest, 21st International Photovoltaic Science and Engineering Conference* 2C–5O–08 (2011).
11. S. Mori *et al.* Organic photovoltaic module development with inverted device structure. *MRS Proceedings* **1737,** mrsf14-1737-u17-02 (2015). doi:10.1557/opl.2015.540
12. J. Du *et al.* Zn–Cu–In–Se Quantum Dot Solar Cells with a Certified Power Conversion Efficiency of 11.6%. *Journal of the American Chemical Society* **138,** 4201–4209 (2016). doi:10.1021/jacs.6b00615
13. W. Wang *et al.* Device characteristics of CZTSSe thin-film solar cells with 12.6% efficiency. *Advanced Energy Materials* **4,** 1–5 (2014). doi:10.1002/aenm.201301465
14. T. Minami *et al.* High-Efficiency Cu_2O-Based Heterojunction Solar Cells Fabricated Using a Ga_2O_3 Thin Film as n-Type Layer. *Applied Physics Express* **6,** 44101 (2013). doi:10.7567/APEX.6.044101
15. Y. Zhou *et al.* Thin-film Sb_2Se_3 photovoltaics with oriented one-dimensional ribbons

and benign grain boundaries. *Nature Photonics* **9,** 409–415 (2015). doi:10.1038/nphoton.2015.78
16. P. Sinsermsuksakul *et al.* Overcoming efficiency limitations of SnS-based solar cells. *Advanced Energy Materials* **4,** 1400496–2 (2014). doi:10.1002/aenm.201400496
17. M. Sugiyama *et al.* Band offset of SnS solar cell structure measured by X-ray photoelectron spectroscopy. *Thin Solid Films* **519,** 7429–7431 (2011). doi:10.1016/j.tsf.2010.12.133
18. P. Sinsermsuksakul *et al.* Atomic Layer Deposition of Tin Monosulfide Thin Films. *Advanced Energy Materials* **1,** 1116–1125 (2011). doi:10.1002/aenm.201100330
19. H. Noguchi *et al.* Characterization of vacuum-evaporated tin sulfide film for solar cell materials. *Solar Energy Materials and Solar Cells* **35,** 325–331 (1994). doi:10.1016/0927-0248(94)90158-9
20. V. Steinmann *et al.* Photovoltaics: Non-cubic solar cell materials. *Nature Photonics* **9,** 355–357 (2015). doi:10.1038/nphoton.2015.85
21. R. D. Engelken. Low Temperature Chemical Precipitation and Vapor Deposition of Sn_xS Thin Films. *Journal of The Electrochemical Society* **134,** 2696 (1987). doi:10.1149/1.2100274
22. R. E. Banai *et al.* A review of tin (II) monosulfide and its potential as a photovoltaic absorber. *Solar Energy Materials and Solar Cells* **150,** 112–129 (2016). doi:10.1016/j.solmat.2015.12.001
23. D. Avellaneda *et al.* Structural and chemical transformations in SnS thin films used in chemically deposited photovoltaic cells. *Thin Solid Films* **515,** 5771–5776 (2007). doi:10.1016/j.tsf.2006.12.078
24. M. Ichimura *et al.* Electrochemical deposition of SnS thin films. *Thin Solid Films* **361–362,** 98–101 (2000). doi:10.1016/S0040-6090(99)00798-1
25. M. Gunasekaran and M. Ichimura. Photovoltaic cells based on pulsed electrochemically deposited SnS and photochemically deposited CdS and $Cd_{1-x}Zn_xS$. *Solar Energy Materials and Solar Cells* **91,** 774–778 (2007). doi:10.1016/j.solmat.2006.10.026
26. A. Ortiz *et al.* Tin sulphide films deposited by plasma-enhanced chemical vapour deposition. *Semiconductor Science and Technology* **11,** 243–247 (1996). doi:10.1088/0268-1242/11/2/017
27. L. S. Price *et al.* Atmospheric Pressure Chemical Vapor Deposition of Tin Sulfides (SnS, Sn_2S_3, and SnS_2) on Glass. *Chemistry of Materials* **11,** 1792–1799 (1999). doi:10.1021/cm990005z
28. P. Sinsermsuksakul *et al.* Enhancing the efficiency of SnS solar cells via band-offset engineering with a zinc oxysulfide buffer layer. *Applied Physics Letters* **102,** 53901 (2013). doi:10.1063/1.4789855
29. K. T. R. Reddy *et al.* Photovoltaic properties of SnS based solar cells. *Solar Energy Materials and Solar Cells* **90,** 3041–3046 (2006). doi:10.1016/j.solmat.2006.06.012
30. M. Calixto-Rodriguez *et al.* Structural, optical, and electrical properties of tin sulfide thin films grown by spray pyrolysis. *Thin Solid Films* **517,** 2497–2499 (2009). doi:10.1016/j.tsf.2008.11.026
31. A. Schneikart *et al.* Efficiency limitations of thermally evaporated thin-film SnS solar cells. *Journal of Physics D: Applied Physics* **46,** 305109 (2013). doi:10.1088/0022-3727/46/30/305109
32. V. Steinmann *et al.* 3.88% Efficient tin sulfide solar cells using congruent thermal evaporation. *Advanced Materials* **26,** 7488–92 (2014). doi:10.1002/adma.201402219
33. Y. Kawano *et al.* Impact of growth temperature on the properties of SnS film

prepared by thermal evaporation and its photovoltaic performance. *Current Applied Physics* **15,** 897–901 (2015). doi:10.1016/j.cap.2015.03.026
34. L. Zhao *et al.* In situ growth of SnS absorbing layer by reactive sputtering for thin film solar cells. *RSC Adv.* **6,** 4108–4115 (2016). doi:10.1039/C5RA24144H
35. T. Ikuno *et al.* SnS thin film solar cells with $Zn_{1-x}Mg_xO$ buffer layers. *Applied Physics Letters* **102,** 193901 (2013). doi:10.1063/1.4804603
36. R. E. Banai *et al.* Optical Properties of Sputtered SnS Thin Films for Photovoltaic Absorbers. *IEEE Journal of Photovoltaics* **3,** 1084–1089 (2013). doi:10.1109/JPHOTOV.2013.2251758
37. V. R. Minnam Reddy *et al.* Development of sulphurized SnS thin film solar cells. *Current Applied Physics* **15,** 588–598 (2015). doi:10.1016/j.cap.2015.01.022
38. Y. Kawano *et al.* Effects of Na and secondary phases on physical properties of SnS thin film after sulfurization process. *Japanese Journal of Applied Physics* **55,** 92301 (2016). doi:10.7567/JJAP.55.092301
39. W. Guo *et al.* Highly efficient inorganic–organic heterojunction solar cells based on SnS-sensitized spherical TiO_2 electrodes. *Chemical Communications* **48,** 6133 (2012). doi:10.1039/c2cc31903a
40. G. Yue *et al.* SnS homojunction nanowire-based solar cells. *Journal of Materials Chemistry* **22,** 16437 (2012). doi:10.1039/c2jm32116e
41. B. Show *et al.* Electrochemically synthesized microcrystalline tin sulphide thin films: high dielectric stability with lower relaxation time and efficient photochemical and photoelectrochemical properties. *RSC Adv.* **4,** 58740–58751 (2014). doi:10.1039/C4RA11140K
42. H. Wiedemeier and F. J. Csillag. Equilibrium sublimation and thermodynamic properties of SnS. *Thermochimica Acta* **34,** 257–265 (1979). doi:10.1016/0040-6031(79)87115-4
43. V. Piacente *et al.* Sublimation study of the tin sulphides SnS_2, Sn_2S_3 and SnS. *Journal of Alloys and Compounds* **177,** 17–30 (1991). doi:10.1016/0925-8388(91)90053-X
44. L. A. Burton and A. Walsh. Phase Stability of the Earth-Abundant Tin Sulfides SnS, SnS_2, and Sn_2S_3. *The Journal of Physical Chemistry C* **116,** 24262–24267 (2012). doi:10.1021/jp309154s
45. L. A. Burton *et al.* Synthesis, Characterization, and Electronic Structure of Single-Crystal SnS, Sn_2S_3, and SnS_2. *Chemistry of Materials* **25,** 4908–4916 (2013). doi:10.1021/cm403046m
46. J. Vidal *et al.* Band-structure, optical properties, and defect physics of the photovoltaic semiconductor SnS. *Applied Physics Letters* **100,** 32104 (2012). doi:10.1063/1.3675880
47. M. G. Sousa *et al.* Annealing of RF-magnetron sputtered SnS_2 precursors as a new route for single phase SnS thin films. *Journal of Alloys and Compounds* **592,** 80–85 (2014). doi:10.1016/j.jallcom.2013.12.200
48. R. E. Banai *et al.* Control of Phase in Tin Sulfide Thin Films Produced via RF-Sputtering of SnS_2 Target with Post-deposition Annealing. *Journal of Electronic Materials* **45,** 499–508 (2016). doi:10.1007/s11664-015-4137-2
49. M. Devika *et al.* Influence of annealing on physical properties of evaporated SnS films. *Semiconductor Science and Technology* **21,** 1125–1131 (2006). doi:10.1088/0268-1242/21/8/025
50. O. E. Ogah *et al.* Annealing studies and electrical properties of SnS-based solar cells. *Thin Solid Films* **519,** 7425–7428 (2011). doi:10.1016/j.tsf.2010.12.235
51. M. Ristov *et al.* Chemical deposition of tin(II) sulphide thin films. *Thin Solid Films* **173,** 53–58 (1989). doi:10.1016/0040-6090(89)90536-1

52. B. Ghosh *et al.* Structural and optoelectronic properties of vacuum evaporated SnS thin films annealed in argon ambient. *Applied Surface Science* **257,** 3670–3676 (2011). doi:10.1016/j.apsusc.2010.11.103
53. H. H. Park *et al.* Co-optimization of SnS absorber and Zn(O,S) buffer materials for improved solar cells. *Progress in Photovoltaics: Research and Applications* **23,** 901–908 (2015). doi:10.1002/pip.2504
54. K. Hartman *et al.* Impact of H_2S annealing on SnS device performance. in *2014 IEEE 40th Photovoltaic Specialist Conference (PVSC)* 0362–0364 (IEEE, 2014). doi:10.1109/PVSC.2014.6924932
55. P. Sinsermsuksakul *et al.* Supporting Information for 'Overcoming efficiency limitations of SnS-based solar cells'. *Advanced Energy Materials* (2014). doi:10.1002/aenm.201400496
56. A. M. Abdel Haleem and M. Ichimura. Experimental determination of band offsets at the SnS/CdS and SnS/InS_xO_y heterojunctions. *Journal of Applied Physics* **107,** 34507 (2010). doi:10.1063/1.3294619
57. A. Niemegeers *et al.* On the CdS/$CuInSe_2$ conduction band discontinuity. *Applied Physics Letters* **67,** 843–845 (1995). doi:10.1063/1.115523
58. M. Sugiyama *et al.* Experimental determination of vacuum-level band alignments of SnS-based solar cells by photoelectron yield spectroscopy. *Journal of Applied Physics* **115,** 83508 (2014). doi:10.1063/1.4866992
59. S. Di Mare *et al.* Analysis of SnS Growth and Post Deposition Treatment by Congruent Physical Vapor Deposition. in *31st European Photovoltaic Solar Energy Conference and Exhibition* (2015). doi:10.4229/EUPVSEC20152015-3DV.3.22
60. R. A. Sasala and J. R. Sites. Time dependent voltage in $CuInSe_2$ and CdTe solar cells. in *Conference Record of the Twenty Third IEEE Photovoltaic Specialists Conference - 1993 (Cat. No.93CH3283-9)* 543–548 (IEEE, 1993). doi:10.1109/PVSC.1993.347036
61. S. Demtsu *et al.* Intrinsic stability of thin-film CdS/CdTe modules. in *2010 35th IEEE Photovoltaic Specialists Conference* 001161–001165 (IEEE, 2010). doi:10.1109/PVSC.2010.5614753
62. A. Schneikart. Herstellung und Charakterisierung von SnS-Dünnschichtsolarzellen. (Technische Universitat Darmstadt, 2014).
63. H. R. Chandrasekhar *et al.* Infrared and Raman spectra of the IV-VI compounds SnS and SnSe. *Physical Review B* **15,** 2177–2183 (1977). doi:10.1103/PhysRevB.15.2177
64. B. L. Xu *et al.* $CdCl_2$ activation treatment: A comprehensive study by monitoring the annealing temperature. *Thin Solid Films* **582,** 110–114 (2015). doi:10.1016/j.tsf.2014.10.006
65. D. Menossi *et al.* Study of $MgCl_2$ activation treatment on the defects of CdTe solar cells by capacitance-voltage, drive level capacitance profiling and admittance spectroscopy techniques. *Thin Solid Films* (2016). doi:10.1016/j.tsf.2016.10.008
66. A. Salavei *et al.* Study of difluorochloromethane activation treatment on low substrate temperature deposited CdTe solar cells. *Solar Energy Materials and Solar Cells* **112,** 190–195 (2013). doi:10.1016/j.solmat.2013.01.019
67. S. Di Mare *et al.* A study of SnS recrystallization by post deposition treatment. in *2016 IEEE 43rd Photovoltaic Specialists Conference (PVSC)* 0431–0434 (IEEE, 2016). doi:10.1109/PVSC.2016.7749627
68. H. R. Moutinho *et al.* Studies of recrystallization of CdTe thin films after $CdCl_2$ treatment. in *Conference Record of the Twenty Sixth IEEE Photovoltaic Specialists Conference - 1997* 431–434 (IEEE, 1997). doi:10.1109/PVSC.1997.654120
69. The European Parliament and the Council of the European Union. REGULATION (EC) No. 1005/2009. *Official Journal of the European Union* **L 286, 52,** (2009).

70. N. Romeo *et al.* High Efficiency CdTe/CdS Thin Film Solar Cells Prepared by Treating CdTe Films with a Freon Gas in Substitution of $CdCl_2$. in *Proceedings of the 21st European Photovoltaic Solar Energy Conference and Exhibition* 1857–1860 (2006).
71. K. Timmo *et al.* Comparative study of SnS recrystallization in molten CdI_2, $SnCl_2$ and KI. *physica status solidi (c)* **13,** 8–12 (2016). doi:10.1002/pssc.201510082
72. I. Rimmaudo *et al.* Etching effect of CdTe absorber on the stability of thin film solar cell devices. in *2013 IEEE 39th Photovoltaic Specialists Conference (PVSC)* 2029–2033 (IEEE, 2013). doi:10.1109/PVSC.2013.6744871
73. D. L. Bätzner *et al.* Development of efficient and stable back contacts on CdTe/CdS solar cells. *Thin Solid Films* **387,** 151–154 (2001). doi:10.1016/S0040-6090(01)00792-1
74. M. Nguyen *et al.* ZnS buffer layer for $Cu_2ZnSn(SSe)_4$ monograin layer solar cell. *Solar Energy* **111,** 344–349 (2015). doi:10.1016/j.solener.2014.11.006
75. K. Ramanathan *et al.* High-Efficiency Cu(In,Ga)Se_2 Thin Film Solar Cells Without Intermediate Buffer Layers. in *2nd World Conference and Exhibition on Photovoltaic Solar Energy Conversion* (1998).
76. L. Kranz *et al.* Doping of polycrystalline CdTe for high-efficiency solar cells on flexible metal foil. *Nature Communications* **4,** (2013). doi:10.1038/ncomms3306
77. A. Polman *et al.* Photovoltaic materials: Present efficiencies and future challenges. *Science* **352,** aad4424-aad4424 (2016). doi:10.1126/science.aad4424
78. S. M. Sze and M.-K. Lee. *Semiconductor Devices: Physics and Technology*. (Wiley, 2013).
79. O. Dupré *et al.* Physics of the temperature coefficients of solar cells. *Solar Energy Materials and Solar Cells* **140,** 92–100 (2015). doi:10.1016/j.solmat.2015.03.025
80. 'Electron Interaction with Matter', Claudionico~commonswiki (Own work) [CC BY-SA 4.0]. Available at: https://commons.wikimedia.org/wiki/File%3AElectron_Interaction_with_Matter.svg. (Accessed: 23rd January 2017)
81. Applied Physics 298r: Interdisciplinary Chemistry, Engineering, and Physics. Dr. Chen E. presentation 'Fabrication Techniques II: Deposition'. Available at: http://www.mrsec.harvard.edu/education/ap298r.php. (Accessed: 21st January 2017)
82. D. L. Smith. *Thin-Film Deposition: Principles and Practice*. (McGraw-Hill, 1995).
83. Nanotechnology Engineering 343: Microfabrication and thin film technology. Dr. Cui B. presentation 'Chapter 9 Thin film deposition III'. Available at: https://ece.uwaterloo.ca/~bcui/?page_id=20. (Accessed: 21st January 2017)